5-2004

Hydraulic Testing of the Big Hole Fault, Northern San Rafael Swell, Utah

William M. Schieb
Utah State University

HYDRAULIC TESTING OF THE BIG HOLE FAULT, NORTHERN SAN RAFAEL SWELL, UTAH

by

William M. Schieb

A thesis submitted in partial fulfillment
of the requirements for the degree

of

MASTER OF SCIENCE

in

Geology

UTAH STATE UNIVERSITY
Logan, Utah

2004

ABSTRACT

Hydraulic Testing of the Big Hole Fault, Northern San Rafael Swell, Utah

by

William M. Schieb, Master of Science

Utah State University, 2004

Major Professor: Thomas E. Lachmar
Department: Geology

Six cross-hole packer tests were conducted at the Big Hole fault, a dip-slip normal fault in the northern San Rafael Swell of east-central Utah. Three tests were conducted at each of two locations along the fault, each location having a different total displacement. Water was injected in the footwall, hanging wall, and fault core and pressure changes were monitored in isolated intervals in the adjoining wells. Response curves were analyzed using the type curves developed by Hsieh and Neuman, and Theis, in order to evaluate the hydraulic properties of the fault and its associated damage zone.

The tests were not quantitatively interpretable. Response curves were a poor match for Hsieh type curves and failed to give a positive definite hydraulic conductivity tensor. Theis analysis showed transmissivity varied over four orders of magnitude. The fault was both a barrier to and a conduit for fluid flow, indicating it was both heterogeneous and anisotropic with regard to flow. No correlation was seen between the fault displacement and the hydraulic properties of the fault.

The lack of consistent results indicates a high variability in the hydraulic

properties of the fault, possibility resulting from changes in fault core thickness and slip surface density over small distances. Injection testing at this intermediate scale is not an effective method in determining hydraulic properties of faults in sandstone reservoirs with deformation band style faulting.

(135 pages)

ACKNOWLEDGMENTS

I would like to thank my advisor, Dr. Thomas Lachmar, for his work in designing the tests and guiding me through their implementation. I would also like to thank Dr. James Evans for giving me the opportunity to work on this project, and Dr. W. David Liddell for serving on my committee and keeping me calm in stressful times.

Funding for this work was provided by the OBES-Department of Energy grants DE-FG03-00ER15042 and DE-FG03-95ER14526.

William M. Schieb

CONTENTS

Page

LIST OF TABLES

LIST OF FIGURES

INTRODUCTION

Statement of Problem

There is an increasing need to be able to characterize and predict fault zone hydraulic conductivity in fractured- and faulted-rock reservoirs. In the hydrocarbon industry, a predictive knowledge of fault zone structure and permeability can have a large influence on the economic viability of exploration targets and currently producing oil fields. Migration of hydrocarbons may be through fractured and faulted rock (Parnell, 1997; Magnavita, 2000) or the trap itself may be a by-product of faulting (Moretti et al., 2000). Impermeable cap rock may be juxtaposed over the reservoir rock by a fault and/or the fault itself may be a barrier to flow within a reservoir.

Large reservoirs may contain numerous faults within the rock unit comprising the reservoir. Economic production of such a reservoir requires knowing if the faults compartmentalize the reservoir (Riley et al., 1993; Moretti et al., 2000). Calculated well placement and spacing is based on the producible mass of rock delineated by faulting, rather than the boundaries of the reservoir as a whole.

Current knowledge of reservoirs is normally limited to seismic studies, giving large-scale views of the reservoirs, and drill cores, giving a very small view. A predictive knowledge of what happens at the intermediate scale is necessary to bridge the gap in our view of the reservoir. Large-scale faulting detected by seismic imaging may be, in fact, a series of faults, and the nature of their connections can have a large impact on flow across the fault plane.

Rather than treating the fault as a planar feature, it is necessary to treat it as a

volume comprised of different components, each with its own distinct hydraulic properties. Fault zone components are: a fault core, where most of the displacement is accommodated, and a damaged zone that is a result of the mechanical growth of the fault (Sibson, 1977; Chester and Logan, 1986; Davison and Wang, 1988; Forster and Evans, 1991; Byerlee, 1993; Scholz and Anders, 1994; Caine et al., 1996). Knowing the hydraulic properties of each component and the spatial relationships of the components is necessary for predicting the hydraulic behavior of the fault zone as a whole.

The effects on flow properties by fractures and faults are a concern in municipal water production for similar reasons. With increasing populations and limited financial means, many more water districts must use fractured rocks in low permeability units as a water source. Often limited subsurface data are available due to development over the reservoir, and the resources controlled by the development district rather than the location of the best reservoir dictate the positioning and number of wells. With this limited ability to directly measure the reservoir properties, it is important to have models that can properly predict the flow patterns within the reservoir from limited subsurface data.

Problems associated with contamination of groundwater are also influenced by fracture and fault flow (Willhite et al., 1986; Jakobsen and Klint, 1999; David et al., 1999). Models treating fractured reservoirs as an equivalent continuum have failed to predict contamination of wells far from the site of contamination, sometimes bypassing closer wells in the process. Similar problems arise dealing with cleanup and interception strategies.

In many cases, an understanding of the subsurface flow system is essential to the success of the project. Questions that need to be addressed are:

- What controls the permeability distribution within a particular fault? Is it a function of the fault core, the damage zone, or a combination of the two?
- Can correlations be made between lithology, structure and hydraulic zones within the fault?
- Do fault networks form linked systems to produce conduits or barriers to flow on a large scale?

Further study of sub-seismic faulting is needed, at a scale similar to actual well placement in the field, to successfully deal with these problems. This study addresses these problems by investigating the hydraulic properties of a high-angle, dip-slip, normal fault in the Navajo Sandstone. Injection tests have been used to measure the hydraulic conductivity within and between the fault core and the damaged zone (Caine et al., 1996) to gain an improved understanding of the fault zone hydraulic properties. The tests were preformed using a multi-hole technique to provide a large (3-7 m) representative volume.

Objectives

The objectives of the injection tests were:

- Determine if the fault acts as a barrier to flow perpendicular to the fault plane and/or enhances flow parallel to the fault plane. The barrier could be absolute (no flow) or relative (low flow compared to host rock). This would be the first step in creating a future conceptual model of the fault permeability structure.
- If possible, establish numerical hydraulic conductivity values for the different permeability components observed in the fault using the cross-hole testing method (Hsieh and Neuman, 1985; Hsieh et al., 1985). This could then be used to calibrate model parameters in any subsequent work.

- Determine if a fault-fracture system can be treated as an equivalent continuum on the scale of the tests. Two criteria need to be met to treat the rock mass as a three-dimensionally uniform, anisotropic medium: the head data must fit the Hsieh type curve and the square roots of the directional diffusivity must delineate an ellipsoid in three dimensions. This would be part of a conceptual model used in future work.
- Determine if the hydraulic conductivity values were a function of the fault displacement. This could be a result of changes in the fault composition from cataclasis, fracture infilling associated with fluid flow, changes in fracture apertures and geometries, or some combination of these. This would be accomplished by running tests at two locations on the fault known to have different offsets.

Study Location

The study location had to meet a number of criteria.

- The fault should contain both fault elements; fault core and damage zone.
- The scale of faulting in the area should be a good analog for aquifer or oil-field scale compartmentalization.
- It had to be accessible primarily by existing roads to keep drilling costs within budget constraints.
- There had to be an easily accessible supply of water for the injection tests.
- The fault had to be previously studied so the fault structural properties were already known.
- The water table had to be shallow enough to allow it to intersect the fault far

enough below the water table so that the fault could be tested with multiple boreholes within the budget constraints.

- Permission to drill had to be obtained.

The Big Hole fault located in the Chimney Rock fault array of the northern San Rafael Swell of east-central Utah was chosen for this study (Figure 1). The fault lies in Emery County, Utah, T19S, R13E, and has been previously studied by Shipton and Cowie (Shipton, 1999; Shipton and Cowie, 2001; Shipton et al., 2002); thus, the fault trace location and slip magnitudes along the fault are known. The Chimney Rock fault array is an excellent analog for similar faults in sandstone reservoirs (Shipton et al., 2002), as described by Gibson (1994), Antonellini et al. (1999), and Fossen and Hesthammer (2000). Faulting in the Navajo Sandstone host rock creates oil-field scale compartments.

In 1980, a United States Geological Survey (USGS) test hole was drilled ~ 400 m from the Big Hole fault test site, and is currently maintained as a well for supplying drinking water for cattle. The USGS test well was drilled to a depth of 93 m, through the Carmel Formation and completed in the Navajo Sandstone. Perched water was encountered in the Carmel Formation at 17.7 m. The depth to the water table in the well was 29 m, and the contact between the Navajo and Carmel Formations was 36.6 m below the land surface (1583 m altitude). The discharge rate for the aquifer at this well was estimated as 1.9×10^{-3} m^3/s while cleaning the hole with air. It was also used as a water source for the testing.

The land is owned by the Bureau of Land Management (BLM), which gave permission for drilling. The test sites can be reached by taking the east-west improved dirt road that

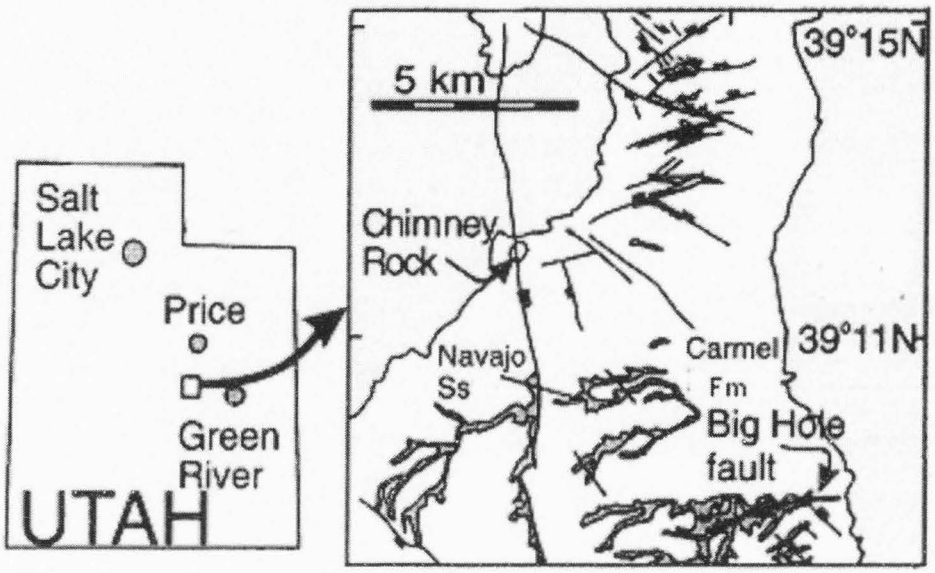

Figure 1 Location of the Big Hole fault, San Rafael Swell, east-central Utah (modified from Shipton and Cowie, 2001).

transverses the northern San Rafael Swell just south of Woodside, Utah, on U.S. Highway 6 and proceeding west to a rough dirt road that runs south, approximately paralleling the abandoned Rio Grande Western Railroad grade.

BACKGROUND

Northern San Rafael Swell

Structure

The San Rafael Swell is a broad, east-vergent, monoclinal flexure (Gilluly, 1929), resulting from the arching of Precambrian through early Tertiary rocks. Formation of the Swell began at 75 Ma and deformation ceased approximately at 58 Ma (Fouch et al., 1983; Lawton, 1986). The west flank has a gentle dip, commonly 2° to 6° westward. The east flank at the latitude of the Big Hole fault commonly dips 10° to 20° eastward, forming an easily discerned monocline.

There are three distinctive fault sets in the San Rafael Swell; 1) a north-striking set, 2) a west-striking set, and 3) a north- and northeast-striking set (Witkind, 1991). All are normal, steeply dipping, linear to slightly sinuous, dip-slip faults ranging in length from several hundred meters to 15 km. They are often paired locally to form grabens ranging from 300 to 1200 m wide. In the northern part of the San Rafael Swell, the oldest offset rocks are Permian in age and the youngest are Late Cretaceous. The faults extend beyond the Swell into rocks of Eocene age. Witkind (1991) speculates that the faults formed due to dissolution of underlying salt, with the northwest- and west-striking faults deriving from solution of the middle Pennsylvanian Paradox Salt Formation and the north-striking faults from dissolution of salt in the middle Jurassic Carmel Formation, or its correlative, the Arapien Shale. The inferred position of the zero isolith of the Paradox Salt Formation runs west between the west- and northwest-striking fault sets and curves south along the western side of the northwest-striking fault set (Baars and

Stevinson, 1981).

Evidence of the age of the faulting is not firmly established. The fact that they strike across the San Rafael Swell, independent of the northeast trend, indicate they are younger than the San Rafael Swell. The northwest-trending faults cut beds as young as the Colton Formation, which is Eocene in age, and are overlain by surficial deposits of Quaternary and Pliocene age. This suggests an age range of Eocene up to the Pleistocene (Witkind, 1991).

The Chimney Rock fault array is a set of mutually crosscutting, northwest- and northeast-striking dip-slip normal faults. Krantz (1988) suggests the faults accommodate north-south extension of the San Rafael Swell. Extension parallel to the fold axis in the region of maximum plunge may be the cause of the faulting (Shipton, 1999), which would date the faults as late Cretaceous – early Tertiary. The Big Hole fault is the southernmost fault in the Chimney Rock fault array.

The Big Hole Fault is a pure dip-slip, high angle normal fault in the Jurassic Navajo Sandstone. The fault strikes N70°E and dips 64°N. Throw along the fault has been determined by Shipton (1999) by detailed surveys of the base of the Carmel Sandstone, which is a regional unconformity marking the marine transgression over the Navajo Sandstone (Figure 2). The data show a maximum slip of 24 m, with slip decreasing towards the ends. The easternmost measurable slip of 8 m is in the Big Hole Wash, but the fault can be traced on the surface to the east, as a north-facing monocline in the Carmel Formation. The monocline extends at least 500 m east of the wash. Linear extrapolation of the fault (Cowie and Shipton, 1998) from the final easternmost exposure in the wash put the fault tip at 800-1000 m further east.

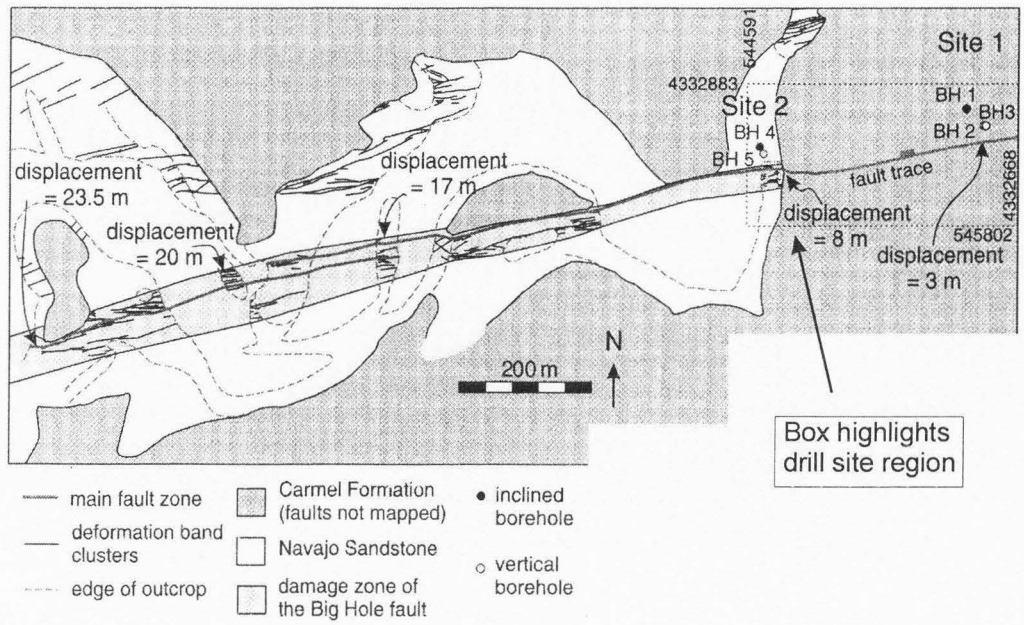

Figure 2 Fault displacements at eastern end of Big Hole fault (modified from Shipton et al., 2002).

The fault core in the Big Hole fault is a zone of fine-grained, cataclastically deformed rock up to 30 cm thick (Shipton, 1999). The core is bounded by narrow, typically polished or mineralized slip surfaces that are interpreted as accommodating the majority of the slip on the fault. The internal structure of the core consists of oppositely dipping deformation bands and slip surfaces that appear sub-parallel and anastomosing in plan view. The fault core is composed of very fine grained fault gouge and pods of relatively undeformed host rock. Porosity in the gouge may be less than 1% (Shipton and Cowie, 2001), and the permeability may be seven orders of magnitude less than the host rock (Antonellini and Aydin, 1994).

The damage zone contains anastomosing clusters of deformation bands dipping steeply to the north and south (Shipton et al., 2002). Individual deformation bands were formed by cataclastic grain crushing (Aydin, 1978), causing a reduction in permeability

and porosity. No chemical change is apparent between the deformation bands and the host rock. Individual slip surfaces are narrow, opaque planar structures surrounded by fault gouge.

Stratigraphy

Sedimentary rock units known to underlie the northern San Rafael Swell west of U.S. 6 range in age from the Pennsylvanian Hermosa Formation to the Cretaceous Mancos Shale. The Big Hole fault is in the Navajo Sandstone, a very fine to fine-grained eolian quartz arenite, which outcrops over large areas of the northern San Rafael Swell (Figure 3). At the Big Hole fault, it is 137-151 m thick (Shipton et al., 2002), and can be informally divided into three members (Thomas et al., 2000): an upper poorly sorted, cross-bedded, dune sequence, a middle massive sequence of well-sorted, fine sands, and a lower dune cross-stratified sequence. The Carmel Formation, a well-bedded, fine-grained limestone, overlies the Navajo.

Hydrology

The Green River and its two tributaries, the Price River and the San Rafael River, drain the northern San Rafael Swell. The Green River is east of the study area, and is not significantly affected by the Swell. The Price and San Rafael Rivers derive their flow from the mountains to the northwest of the Swell, but much of their flow is diverted for agriculture (Hood and Patterson, 1984). Despite the dry nature of the climate in the San Rafael Swell, the majority of recharge to the hydrologic system is by precipitation (Table 1). A small amount of groundwater, <1% of total flow, enters the rivers from the Navajo Sandstone (Hood and Patterson, 1984).

Five geologic units are considered major aquifers in the San Rafael Swell, either because

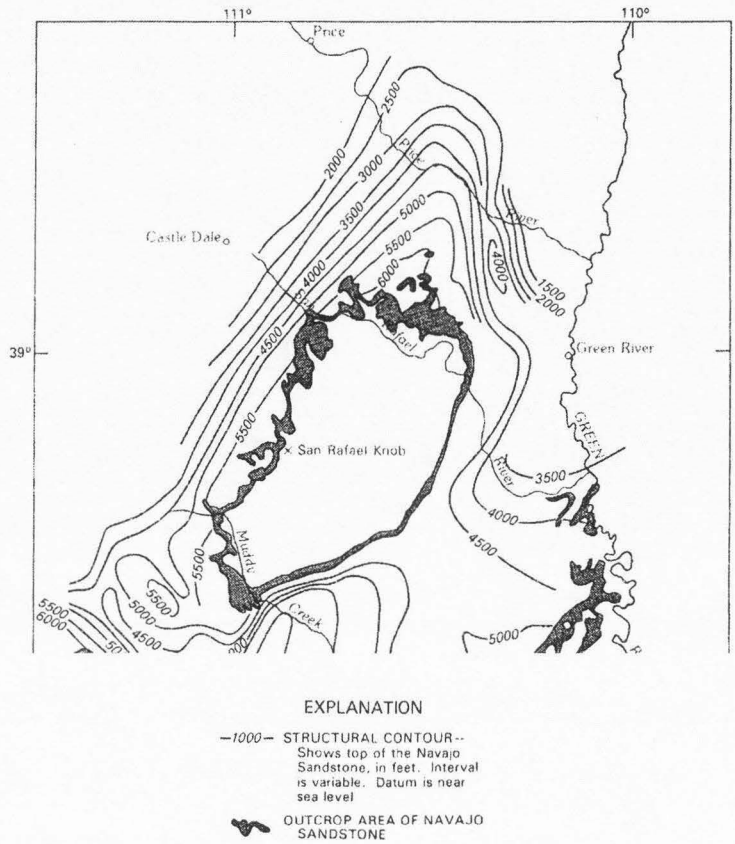

Figure 3 Outcrop and structural contours of the Navajo Sandstone in the northern San Rafael Swell (modified from Weiss, 1987).

of their large areal extent or thickness, or their potential for locally large yields: the Entrada, Navajo, Wingate, and Coconino Sandstones and rocks of Mississippian age (Table 2; Hood and Patterson, 1984). The Navajo, Wingate and Coconino Sandstones are the principal aquifers in the northern San Rafael Swell. Recharge to the aquifers occurs mainly in the winter, when prolonged wet surface conditions occur and evaporation is at a minimum. The low vertical permeabilities of most of the aquifers (0.0029 to 0.5 m/day for the three principal sandstone aquifers; Hood and Patterson, 1984) exclude recharge from short-term, high intensity precipitation events, such as thesummer thunderstorms common to the Swell. Most precipitation at these times is lost to run-off and evaporation.

TABLE 1 SUMMARY OF HYDROLOGIC ESTIMATES (MODIFIED FROM HOOD AND PATTERSON, 1984)

Complete Hydrologic System	Long-Term Average (m^3/yr)
Inflow	
Precipitation	1.419×10^9
Price River, stations 09314250 plus 09314280	8.494×10^7
San Rafael River at station 09328000	6.916×10^7
Groundwater inflow	None
Total (rounded)	1.604×10^9
Outflow	
Price River at station 09314500	8.709×10^7
San Rafael River at station 09328500	7.555×10^7
Estimated yield of ungaged areas	3.701×10^6
Discharge by wells, probable maximum	2.467×10^5
Ground-water outflow, minimum	7.401×10^5
Evapotranspiration, gross	* 1.405×10^9
Total (rounded)	1.604×10^9
Ground-Water System †	
Navajo Sandstone only §	
Recharge	
From precipitation	3.701×10^6
From ground-water inflow	None
Total	3.701×10^6
Discharge	
To San Rafael and Green Rivers	2.467×10^6
Ground-water outflow	7.401×10^5
Evapotranspiration	4.934×10^5
Total	3.701×10^6
Complete Groundwater System (includes Navajo)	
Recharge #	1.234×10^7
Storage in three major consolidated aquifers	5.427×10^{11}
Recoverable fresh to moderately saline water	** 1.974×10^{11}

* Amount calculated by difference between other individual items of inflow and outflow

† Incomplete budget because of unknowns

§ Rounded amount for each item as used or inferred from steady-state digital model for best fit of potentiometric surface

Assumed to equal long-term discharge

** Assumes complete drainage of Navajo, Wingate, and Coconino Sandstones

TABLE 2 MAJOR AQUIFERS OF THE SAN RAFAEL SWELL (MODIFIED FROM HOOD AND PATTERSON, 1984)

Aquifer	Hydrologic Properties
Entrada	Very low to moderate permeability. Water fresh near areas of recharge, deteriorating with distance from outcrop and depth. Fresh water of sodium bicarbonate type. Saline water has sulfate as dominant anion.
Navajo	Low to moderate permeability, erratically distributed fracturing, fresh to moderately saline water.
Wingate	Very low to moderate permeability. Similar hydraulic conductivity to lower Navajo but overall lower due to silt beds. Water is calcium magnesium carbonate type. Saline water is dominantly sulfate type.
Coconino	Very low to low permeability. Partly to fully drained in upper parts of Swell. Fresh near outcrops. Saline water is of sodium chloride type.
Mississippian Rocks	Very low (undisturbed carbonate) to high (where faulted, fractured or dissolved) permeability. Saline except near points of recharge from above.

Recharge is also affected by surface exposure of the aquifers, with the Navajo receiving the most recharge due to the Navajo's larger areal extent.

The Carmel Formation is considered important because, while it is not a significant aquifer, it has a large areal extent and can receive recharge directly. It overlies the Navajo Sandstone and can locally supply or receive water from it. Locally, it can be a good aquifer with discharges of approximately 1.0 m^3/s, but most discharges at springs and wells range from seepage to 1.9×10^{-3} m^3/s (Hood and Patterson, 1984). It also has large amounts of evaporites (primarily gypsum) that contribute to the deterioration of ground water quality.

Estimates of storage have been made for the Wingate, Navajo, and Coconino Sandstones. Total storage in these aquifers is 5.43×10^{11} m^3, but only 1.97×10^{11} m^3 of fresh to moderately saline water is recoverable (Table 1 and Table 3). This is the upper

TABLE 3 GROUNDWATER STORAGE IN THREE MAJOR AQUIFERS OF THE SAN RAFAEL SWELL (MODIFIED FROM HOOD AND PATTERSON, 1984)

Aquifer	Average Thickness (m)	Area (km^2)	Effective Porosity (%)	Volume of Groundwater in Storage (millions of m^3)
Navajo Sandstone	126	5960	17.7	1.16×10^5
Wingate Sandstone	122	6090	20	1.23×10^5
Coconino Sandstone	213	7460	20	2.86×10^5
Total				5.43×10^5

limit, assuming total drainage, and is not a realistic number for water development. The volume of water in all the other aquifers is probably less than in these three aquifers.

The groundwater in the Navajo Sandstone occurs under both confined and unconfined conditions. The easterly dip of the rock units creates a confined aquifer in the east where the depth to the top of the unit is great. The aquifer becomes unconfined near the axis of the monocline to the west. The potentiometric surface dips eastward in the study area, as does the ground surface and the top of the Navajo Sandstone (Hood and Patterson, 1984).

The permeability of the Navajo Sandstone ranges from very low to moderate, though it may be high locally. Measured values for hydraulic conductivity from cores and outcrop samples range from 0.001 to 1.6 m/d (Hood and Patterson, 1984). Transmissivities range from 2.5 to 60.1 m^2/d based on short-term pumping tests. Hood and Danielson (1979) estimated the specific yield to be between 0.05 and 0.10, and assumed a storativity of 0.001 for the Navajo Sandstone in the northern San Rafael Swell.

Fault Zone Architectural Style and Permeability Structures

Fault Zone Architectural Components

The two hydrologically important architectural components of the fault are the fault core and the damage zone (Figure 4). The fault core is the structural, lithologic, and morphologic portion of the fault zone where the most displacement is accommodated (Caine et al., 1996). The fault core may contain single slip surfaces (Caine et al., 1991), clay-rich gouge (Anderson et al., 1983), brecciated and geochemically altered zones (Sibson, 1977), or highly indurated cataclastic zones (Chester and Logan, 1986). Flow properties in the core are influenced by the core thickness variations, internal structure and composition (Caine et al., 1996). Grain size reduction and/or precipitation of minerals can yield fault cores with lower porosity and permeability than the surrounding protolith (Chester and Logan, 1986; Antonellini and Ayden, 1994; Goddard and Evans, 1995).

The damage zone bounds the fault core, and is a network of subsidiary structures including small faults, veins, fractures, cleavage, and folds causing heterogeneity and

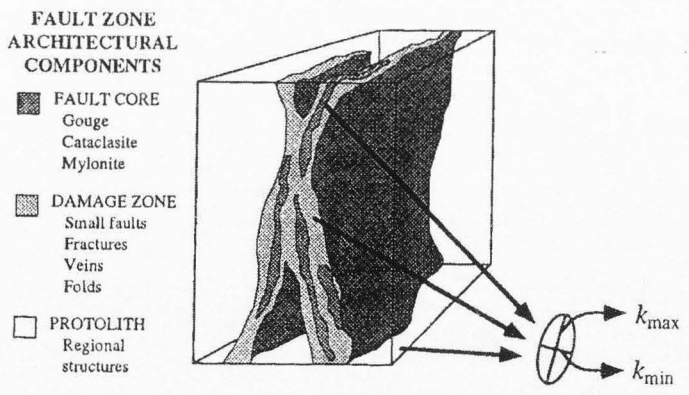

Figure 4 Fault zone architectural components (modified from Caine et al., 1996).

anisotropy in the permeability structure (Bruhn et al., 1994). These features can enhance the permeability of the fault zone relative to the core and the undeformed protolith (Chester and Logan, 1986; Smith et al., 1990; Andersson et al., 1991; Scholz and Anders, 1994; Goddard and Evans, 1995).

Barrier-conduit systems associated with fault zones are controlled by the geometry and magnitude of the contrasts between the core and the damage zone (Caine et al., 1996). Fault zone cores have a significantly smaller fracture density than damage zones (Andersson et al., 1991; Chester et al., 1993). Fault core permeability is dominated by grain-scale processes, such as grain size reduction, chemical alteration, and infilling between grains by clays. The damage zone is dominated by the hydraulic properties of the fracture network.

Permeability Structures

Fault zones exist as a range of architectures. The four end-members are each associated with a distinctive permeability structure (Table 4 and Figure 5; Chester and Logan, 1986; Bruhn et al., 1990; Forster and Evans, 1991; Moore and Vrolijk, 1992; Newman and Mitra, 1994). The four permeability structures are distributed conduit, localized conduit, localized barrier, and combined conduit barrier. They are characterized by the magnitude of the architectural components and their relative ratios. Each end member has unique properties and requires using an appropriate flow model.

The Big Hole fault consists of a fine-grained, cataclastically deformed fault core of low permeability surrounded by a damage zone (Shipton et al., 2002) and most closely matches the combined conduit-barrier model.

TABLE 4 PERMEABILITY STRUCTURES AND THEIR ASSOCIATED ARCHITECTURAL STYLE (MODIFIED FROM CAINE ET AL., 1996)

Permeability Structure	Architectural Style	Fault Core	Damage Zone	Examples	Applicable Flow Model
Localized conduit	Localized slip along a single surface or segmented planes.	Absent to poorly developed.	Absent to poorly developed.	Small faults in Shawangunk Mountains of eastern New York (Caine et al., 1991).	Discrete fractures modeled as conduits with parallel walls.
Distributed conduit	Distributed slip accommodated along distributed surfaces.	Absent to poorly developed.	Well-developed discrete slip surfaces and associated fracture networks.	Modern accretionary prisms (Moore and Vrolijk, 1992).	Equivalent porous medium.
Localized barrier	Localized slip accommodated within cataclastic zone.	Well-developed fault core cataclasites.	Absent to poorly developed.	Deformation bands in sandstones (Antonellini and Aydin, 1994).	Aquitard (fault core) within a higher-permeability aquifer (protolith).
Combined conduit-barrier	Deformation accommodated within a localized cataclastic zone subsidiary structures.	Well-developed fault core cataclasites.	Well-developed discrete slip surfaces and associated fracture networks.	Dixie Valley normal fault, Dixie Valley, Nevada (Bruhn et al., 1994).	Aquitard (fault core) sandwiched between two aquifers.

Groundwater Flow Modeling

Conceptual Modeling

Two types of models are necessary to predict fluid flow. A conceptual model describes the geology, hydrological setting, and site-specific attributes of the system.

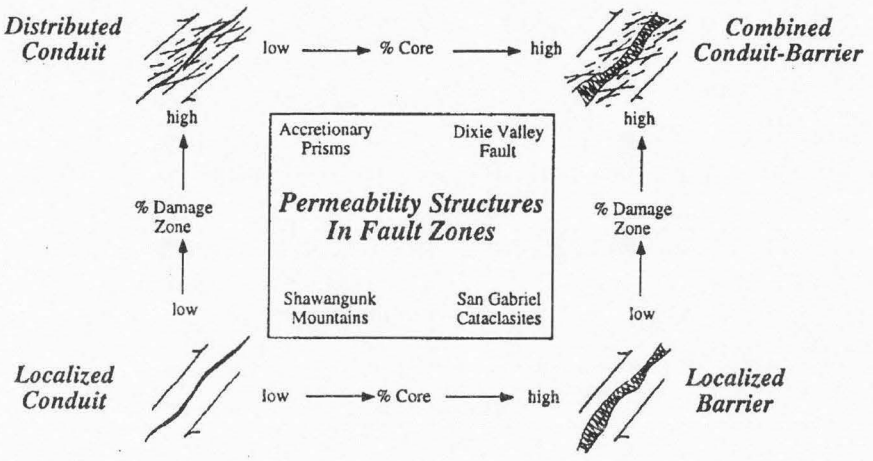

Figure 5 Fault zone permeability structures (modified from Caine et al., 1996).

Building the model requires: 1) identifying the important features of the structural system, 2) identifying the dominant fractures in the system, and 3) determining to what extent the identified structures conduct water (National Research Council, 1996). The preliminary investigation needs to identify and describe the distribution of fracture pathways, determining material properties, geometry, and stress. Two end members are generally recognized: 1) a fracture-dominated system with relatively impermeable matrix and 2) a system dominated by a fracture network within a permeable matrix (National Research Council, 1996).

The scale of interest also needs to be defined. An important question in this context is will the model deal with relatively few features that may dominate on a large scale, or will the scale be small, with a large number of interconnected features? A large-scale model normally assumes uniform properties between the features of interest. These are often properties determined by small-scale measurements that will not adequately describe the heterogeneity of the rock.

The purpose of the conceptual model must be established. A model dealing with solute transport needs to be considerably more refined than a model for simple fluid flow. Travel times and solute concentrations are more sensitive to heterogeneity in fractured systems. The purpose of the model also influences the choice of a mathematical model to describe the flow in a fractured medium.

The conceptual model for this study is the combined conduit-barrier permeability structure presented by Caine et al. (1996) (Table 4). The Big Hole fault may act as a barrier to flow perpendicular to the fault plane and a conduit parallel to the fault plane. The fault has well-developed, localized fault core cataclasites 0.06 to 0.33 m in true thickness in core samples (Shipton et al., 2002; Shipton et al., in press) that may create a flow barrier. In the surrounding Navajo Sandstone there is a distributed zone of fracturing and deformation ~ 11 to 27 m in true thickness (Shipton et al., 2002) that may act as conduits and barriers to flow.

Mathematical Modeling

Mathematical modeling serves two purposes in groundwater investigations. The first purpose is calibration. Initial conditions and properties are rarely known with certainty. The mathematical model acts as feedback to the conceptual model, revealing problems with the initial conditions that may be solved by an additional, more detailed study of the system or by redefining the conceptual model itself. The second purpose is prediction. The model predicts future flow, usually due to perturbation of the system, based on the known hydrologic properties. Mathematical models fall into three broad classes: 1) equivalent continuum models, 2) discrete network simulation models, and 3) hybrid techniques (Table 5).

TABLE 5 MATHEMATICAL MODELS BASED ON HETEROGENEITY REPRESENTATION (NATIONAL RESEARCH COUNCIL, 1996)

Representation of Heterogeneity	Key Parameters that Distinguish Models
Equivalent Continuum Models	
Single porosity	Effective permeability tensor Effective porosity
Multiple continuum (double porosity, dual permeability, and multiple interacting continuum)	Network permeability and porosity Matrix permeability and porosity Matrix block permeability Nonequilibrium matrix/fracture interaction
Stochastic continuum	Geostatistical parameters for log permeability: mean, variance, spatial correlation scale
Discrete Network Models	
Network models with simple structures	Network geometry statistics Fracture conductance distribution
Network models with significant matrix porosity	Network geometry statistics Fracture conductance distribution Matrix porosity and permeability
Network models incorporating spatial relationships between fractures	Parameters controlling clustering of fractures, fracture growth, or fractal properties of networks
Equivalent discontinuum	Equivalent conductors on a lattice
Hybrid Models	
Continuum approximations based on discrete network analysis	Network geometry statistics Fracture transmissivity distribution
Statistical continuum transport	Network geometry statistics

Equivalent Continuum Model

An equivalent continuum model assumes the volume being tested can be modeled as distinct components with consistent properties throughout. These models can be either single or dual porosity (National Research Council, 1996). Only the volume as a whole, not the individual fractures, is considered. The component volumes can be isotropic or anisotropic. The key parameters are the porosity and the permeability tensor, which describe the entire volume in a single porosity model.

The concept of double, or dual, porosity originated with Barenblatt et al. (1960) to deal with the problem of a fractured reservoir in a permeable host rock. Barenblatt et al. (1960) describe such reservoirs by treating them as two overlapping continua: a continuum of relatively low-permeability, primary porosity blocks and a continuum of high-permeability, secondary porosity fractures. The primary porosity blocks contain most of the reservoir fluid with properties controlled by lithology and depositional features. The hydraulic properties of the fracture system are the result of the thermal stress and tectonic processes that created the fracture system. Both may have properties subsequently altered by chemical precipitation, solution processes, or hydrothermal alteration.

Mathematical analysis requires simplifying the system by making assumptions about the flow in the system. One approach is to assume that the host rock permeability is low enough that all flow occurs in the fractures. Studies where fractures intersect also use the no flow assumption, and are treated as equivalent continua. Because fractures often have preferred orientations and spacings, the media is anisotropic and hydraulic conductivity is a vector quantity rather than a scalar (Snow, 1969).

In reservoirs where the permeability of the host rock cannot be discounted, two different approaches to mathematical analysis of well data have been used. One approach assumes the flow occurs under pseudo-steady state conditions (Warren and Root, 1963). The flow in a dual porosity reservoir has two controlling partial differential equations, one describing flow in the fractures and another describing the flow in the blocks of host rock. By assuming the flow at the fracture-rock interface matches in the two systems, the two controlling equations can be set equal.

The other approach assumes flow is transient and the head difference migrates away from the rock-fracture interface and into the host rock block with time (Kazemi, 1969). To achieve a solution with this approach, a block geometry must be specified. Well test data support both approaches (Moench, 1984).

Moench (1984) has proposed a resolution to the two approaches by introducing the concept of a "fracture skin." This is similar to fracture damage as presented by Cinco and Samaniego (1977). The fracture skin would act to delay flow contributions from the block to the fracture and give pressure responses similar to the predictions of the pseudo-steady state flow.

Discrete Network Model

The discrete network model assumes all flow is through individual flow paths that interconnected within the volume. Flow could be through the fracture only or the matrix could also be considered a flow path. The key is that each flow path within the model must be described separately, with its own unique properties, before being incorporated into the model of the volume as a whole. The model is dependent on the properties of the individual flow paths and the geometry of their distribution. This type of model is most easily done using computer modeling. Hydraulic field tests can contribute to fine-tuning such a model, but the initial model construction is highly dependent on physical descriptions of the fractures and matrix from the field and lab tests of the properties of the individual components. Key parameters could be the network geometry (Herbert et al., 1991) or the distribution of the fracture conductance. If the matrix is conductive, the matrix porosity and permeability must be included. Some discrete fracture models also incorporate parameters that describe clustering of fractures, fracture growth, and fractal

properties of networks (Dershowitz et al., 1991).

The cross-hole packer method (Hsieh and Neuman, 1985) used to test the Big Hole fault treats the volume as an equivalent continuum.

Hydraulic Testing

Basic hydraulic testing consists of either injecting or removing water from a borehole. This can be done either in an open borehole or in an isolated interval. Using the open borehole is more economical, but unless the entire hole exists in a homogeneous medium, there is no way to separate the flow paths being used. The results will be dominated by the most permeable layer the hole penetrates. In a fractured rock mass, this may mean all the flow is occurring in just a few fractures and there is no way to determine which fractures are providing the flow pathway. By using an interval isolated with inflatable packers, commonly called packer testing, it is possible to determine which sections of the borehole are actually providing the flow paths. The size of the interval can be varied according to the nature of the rock mass being tested and the expected number of intervals needed to adequately delineate the various flow paths.

Testing may be either in a single borehole or in multiple boreholes. In the multiple borehole scenarios, one borehole is used as an injection or pumping/extraction hole, and the other boreholes act as monitoring points. The monitoring wells may contain multiple isolated intervals, each monitored separately. This allows more flow paths to be documented in a single test. This can be a significant factor in rock with a low hydraulic conductivity where each test may take days or weeks to complete.

The most common method for evaluating hydraulic tests is comparing the results to type curves developed from the mathematical model appropriate to the conceptual

model of the rock mass being tested. These are usually graphs of either head versus time or flow versus time. By matching the curves obtained from the tests to the standard type curves, hydraulic conductivity or transmissivity and specific storage or storativity can be estimated. Deviations in the shapes of the curves can give insight into whether the type curves being used are appropriate for the rock mass being tested.

Test results from the Big Hole fault were compared to type curves developed by Hsieh and Neuman (1985). The solution assumed injection is a point source and the monitoring interval is a point. The results were also compared to standard Theis curves (1935) normally used for isotropic, homogeneous, confined reservoirs. The data curves were corrected for unconfined conditions using the Jacob's correction (Jacob, 1944).

METHODS

Site Description

Borehole Descriptions

The boreholes in the study (Shipton et al., 2002) were drilled to accomplish three different data gathering objectives. The first was to obtain continuous, oriented core across the fault, including the fault core and the damage zone. The core provided information on the boundaries of the damage zone, the width of the fault core, the fracture density, the fracture orientations, and fracture permeability at core-scale resolution. The second objective was to provide a conduit for measurement of the geophysical properties of the fault zone. This information could then be correlated with the core, to provide geophysical signatures for the different zones and relative fracture densities. The third objective was to provide access to the fault zone for permeability tests at a variety of scales, ranging from centimeters within the core samples to meters between boreholes, within and across the fault. These results would give insight into the degree of heterogeneity of the fault zone and indicate if the results of the core testing could be used to represent the hydraulic properties of the fault zone on larger scales.

Five holes (BH-1 through 5) were drilled into the fault at two sites approximately 325 m apart (Figure 6). All holes originate in the hanging wall of the fault and are either vertical or inclined towards the fault. Tonto Drilling Services (now Dynatec), out of Salt Lake City, Utah, drilled all the holes using a HQ diameter (58 mm) core barrel. Boreholes BH 1-3, at the tip zone (Site 1) (Figure 7), were drilled using single tube coring tools, and BH-4 and 5 at the wash (Site 2) (Figure 8) used a double-tube tool to

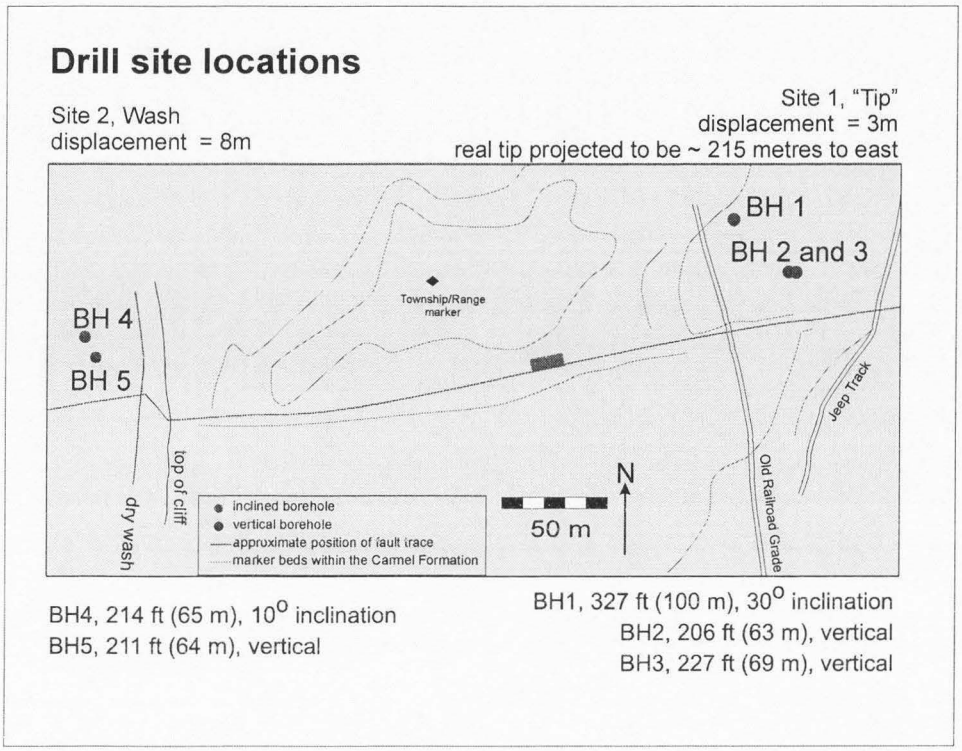

Figure 6 Drill site locations (Shipton et al., 2001).

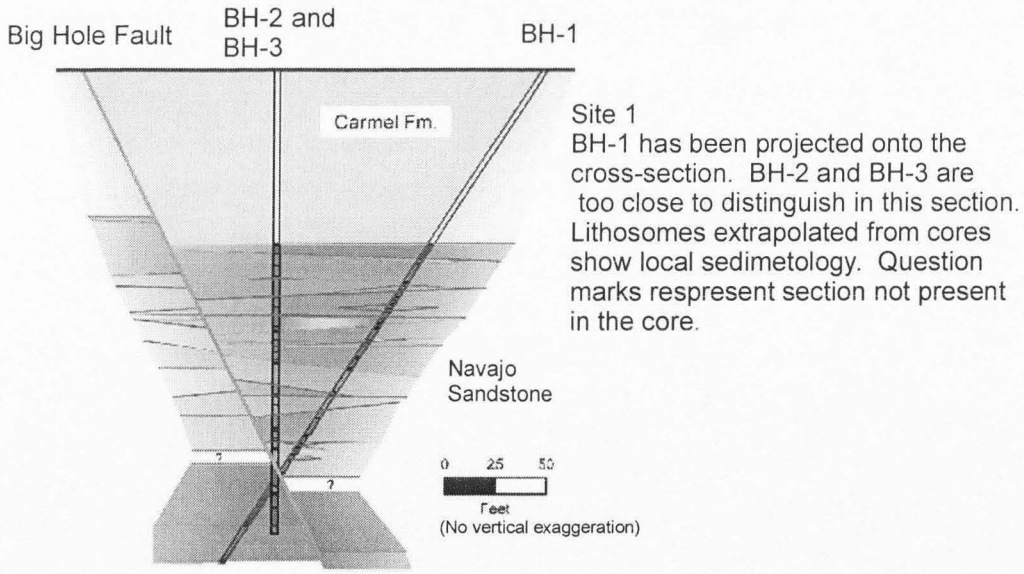

Figure 7 Cross-section of Big Hole fault and boreholes at the tip zone (Site 1) (modified from Shipton et al., 2001).

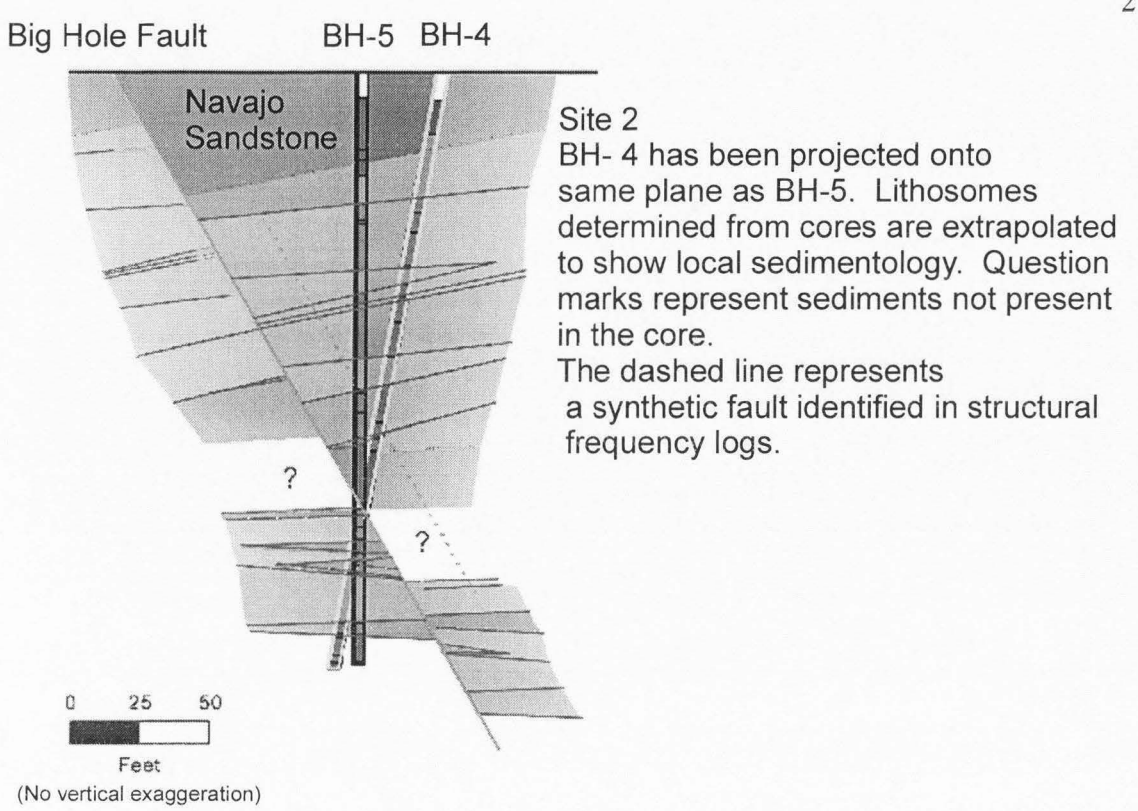

Figure 8 Cross-section of Big Hole fault and boreholes in wash (Site 2) (modified from Shipton et al., 2001).

improve recovery. The orientation work was done by Layne Christensen Services, which used a three-scribe tool with orientations photographically recorded at 2-minute intervals.

The tip zone (Site 1) has 3-5 m of slip, and is an example of a sub-seismic fault tip zone. The Carmel Formation at this location overlies the Navajo Sandstone, and the holes are collared within the Carmel. The fault offsets the upper, cross-stratified sandstone unit against the massive, fine-grained unit (Thomas et al., 2000). Borehole BH-1 was used to evaluate the boundaries of the fault zone, and was the longest (98.8 m) borehole (Table 6). It forms a 62° angle from the horizontal and forms an angle with the fault of 51°. Two vertical boreholes (BH 2 and 3) were drilled intersecting the fault plane approximately 3 m apart along strike and approximately 10 m higher than BH-1.

TABLE 6 VERTICAL DEPTHS AND ORIENTATIONS (FAULT/BOREHOLE ANGLES FROM SHIPTON ET AL., 2002)

	Borehole Depth (m)	Deviation and Azimuth (degrees)	Depth to Fault Intersection (m)	Depth to Water Table (m)	Angle between Hole and Fault (degrees)
BH-1	98.8	28, 122	68.9	43.6	51
BH-2	62.8	0	57.6	38.1	30
BH-3	68.3	0	58.7	38.1	30
BH-4	63.2	9, 191	47.8	33.5	40
BH-5	62.2	0	48.2	33.5	30

The wash (Site 2) has 8 m of slip, and the fault is exposed in the wash and on the cliff face along the side of the wash. Two boreholes were drilled at this site. BH-4 was inclined at 81° from horizontal and BH-5 is vertical. The two boreholes are 1.5 m apart in the plane of the fault and intersect the fault at approximately 47.5 m true vertical depth (TVD).

All boreholes contain four structural components corresponding to the permeability components of the fault zone: host rock, single deformation bands, the fault core, and slip surfaces (Shipton et al., 2002). The single deformation bands are planar structures offsetting bedding. Clusters of deformation bands appear with decreasing distance from the fault core. The core is composed of densely packed, anastomosing deformation bands. Slip surfaces typically lie at the edge or within the fault core, though some clusters within the deformation zone also show slip.

Permeameter Tests

Probe permeameter tests performed at 3-cm intervals on cores taken from the test sites (Shipton et al., 2002) gave values ranging from 1 to 44 mD for the fault core with most values around 1 to 2 mD. Deformation bands gave permeability values ranging

from 1 to 134 mD, with most values around 10 mD, but this value includes some of the host rock due to the width of the probe nozzle being larger than an individual deformation band. Whole-core permeability measurements (Shipton et al., 2002) revealed the anisotropic nature of the fault zone. Permeability values from the fault core showed an order of magnitude difference between orientations perpendicular and parallel to the fault plane (1.4 vs. ~ 16 mD in BH-3) and were similar to the values from the probe permeameter tests.

Test Description

Testing Method

Cross-hole testing is a field method developed by Hsieh and Neuman (1985) for determining the hydraulic conductivity tensor and specific storage in an anisotropic porous or fractured medium. The method consists of injecting fluid into (or withdrawing fluid from) a packed-off interval within a borehole. The transient response is then measured in intervals in neighboring boreholes. This method gives direct field information on whether the rock mass being tested is acting as a uniform anisotropic medium on the scale of the test.

Most methods for determining the hydraulic conductivity tensor through pumping tests assume a horizontal aquifer. Methods for determining the two-dimensional hydraulic conductivity tensor include those developed by Papadopulos (1965), Hantush and Thomas (1966) and Neuman et al. (1984). All these methods assume horizontal flow. Since flow in fractured rock is dominated by fractures that do not necessarily correspond to the vertical and horizontal directions, these methods cannot be used easily.

The cross-hole method removes the constraint of other methods, in that the

principal directions of the hydraulic conductivity ellipse do not need to be known in advance, and the boreholes need not be oriented in one of those directions. The boreholes may be oriented in whatever directions are practical for the site in question, with the stipulation that the observation intervals are not all in the same plane.

The tests were designed by Tom Lachmar, using values for the aquifer properties of the Navajo Sandstone from Hood and Patterson (1984). Distances between the monitoring intervals and the injection intervals were calculated to meet the criteria set out in Hsieh and Neuman (1985) for the point observation/point injection solution, which specifies $2R/L \geq 5$ (R equals the radial distance from the point source and L is the length of the line source). L was standardized in the packer strings as 0.6 m, requiring $R \geq 1.5$ m. After logging the boreholes it was determined two possible test configurations at the wash (Site 2) did not meet this criteria. The distance between BH-4, Zone 1 and BH-5, Zone 1 was 1.34 m and the distance between BH-4, Zone 2 and BH-5, Zone 2 was 1.48 m. The separation distance was kept small to allow testing to be completed within a reasonable time period. The initial goal was to complete each test in six days.

Injection was chosen in preference to pumping for several reasons. There was concern that if the permeability of the rock was too high the potentiometric surface would drop to the level of the pump without reaching a steady-state condition, effectively ending the test. There was also the problem of obtaining a pump capable of sufficient flow that would be small enough to fit in the borehole. Finally, the remote location made powering the pump a concern. Using constant head injection eliminated the need for any power source beyond the batteries necessary for the pressure transducers and the data loggers.

Equipment

Barbara Hall designed the packer strings (Figure 9) and Baski, Inc. of Denver, Colorado, manufactured them. The packers are fixed head with Multi-Ply™ reinforcement along the element. The patented ReFlex™ Baski packers are rated to an inflation pressure of 6.9 kPa. They were mounted on 2.54-cm threaded steel pipe and inflated with nitrogen. Pass-through ports allowed all packers to be inflated from a single line. Pass-through ports were also provided for the lines to the pressure transducers used to monitor the head changes in the observation intervals. With the packers inflated, no further support for the packer string was needed. Strings could be lowered or raised to test different sections of the boreholes by deflating the packers.

The injection boreholes used two 1.5-m packers with a 0.6-m injection interval between them (Figure 9). Water was injected directly into the iron pipe supporting the packers and was released through slotted pipe between the packers in the injection interval. Because of this easy connection to the injection zone, it was possible to measure the water level before tests with the packers in place. This allowed a check that the water table had returned to static between tests.

The packer strings in the monitoring borehole used four 0.9-m packers with 0.6-m observation intervals to create three isolated observation zones. The zones were designated as the footwall (Zone 1), the fault core (Zone 2), and the hanging wall (Zone 3). Each interval had a porous tube end connected by 0.64-cm hard plastic tubing to a pressure transducer mounted on the iron pipe above the packer string to allow monitoring the pressure head in the interval. Geokon Model 4500 vibrating-wire pressure transducers were used to monitor the pressure head in the three zones. The transducers

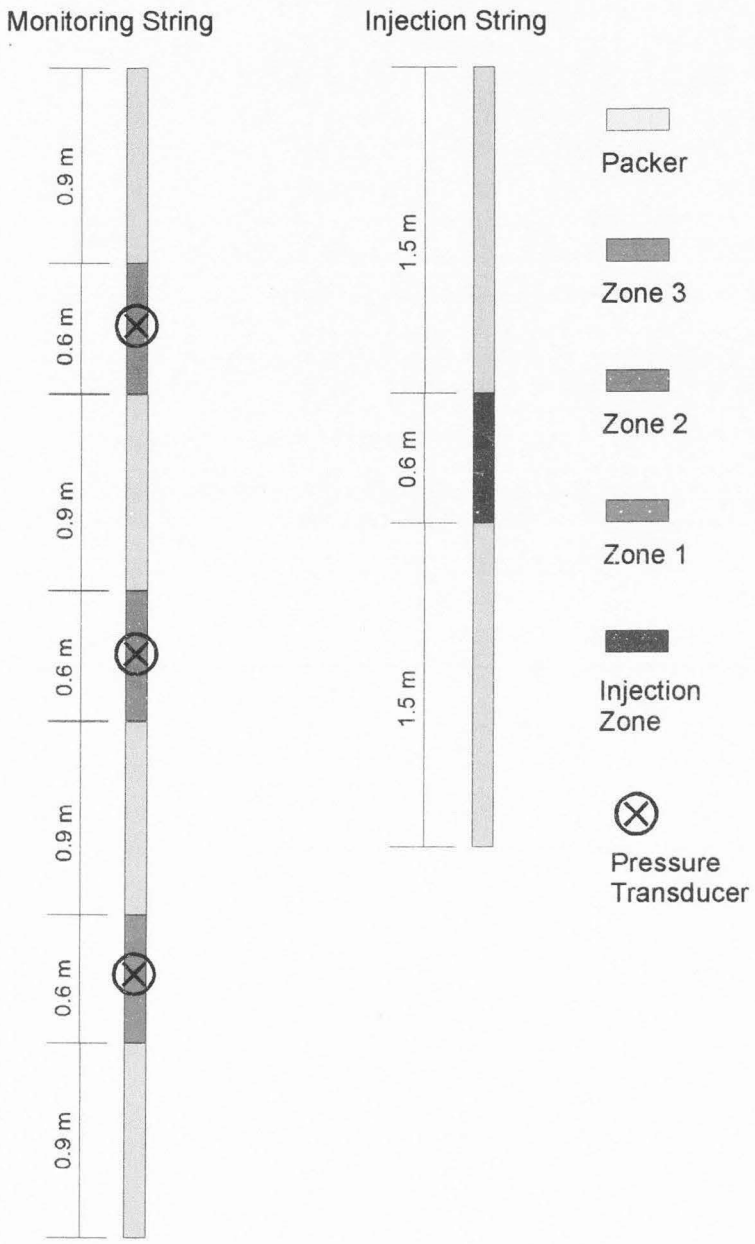

Figure 9 Schematic of packer strings for monitoring and injection.

were rated for a range of 0-34 kPa and when tested by immersion in water in the laboratory had an accuracy of ±0.34 kPa. The actual zones monitored were typically 18 m or more below the water table, and the transducers were mounted on the support pipe at ~ 3.3 m below the static water table and connected to the zones with 0.64-cm hard

plastic tubing. The transducers were calibrated for sea level, but the actual site at which they were used was approximately 1583 m above sea level. Mounting the transducers underwater compensated for the altitude, placing them near the center of their pressure range at static conditions. The water temperature was also monitored so the recorded pressures could be temperature corrected during data reduction. They were then attached to data loggers at the surface with 4-wire waterproof cable.

A CR10X datalogger manufactured by Campbell Scientific, Inc. of Logan, Utah, was used to power and monitor the test equipment. The datalogger is fully programmable with a non-volatile memory. It was used in conjunction with the AVW4 add-on component to provide the additional capabilities necessary for using the vibrating wire pressure transducers. The AVW4 provides the signal conditioning necessary for measuring the sensor's temperature and noise reduction for the vibrating-wire signal. To increase the battery time for the CR10X and eliminate concern about power loss due to cold night-time temperatures, the internal battery was not used. Instead, the CR10X was powered externally using a 12V deep cycle battery. The datalogger was programmed, and periodically monitored, using a standard laptop computer with the Windows operating system.

To eliminate concern about changes in atmospheric pressure during the course of the testing, a CS105 Barometric Pressure Sensor, also manufactured by Campbell Scientific, Inc., was mounted in the datalogger enclosure and monitored by the CR10X. Because the Navajo Sandstone is an unconfined aquifer at the test site, changes in atmospheric pressure should have no effect on the pressure under the water table, and the barometric pressure sensor was only used to confirm this.

The flow to the injection borehole was measured using an Omega FP-5060 Micro-Flow Sensor. The flowmeter has a flow range of 1.89×10^{-6} to 4.41×10^{-5} m^3/s. It was chosen because it should not have had a significant pressure drop over the anticipated flow range ($< 6.3 \times 10^{-6}$ m^3/s). During initial testing, it became apparent that there was a pressure drop at low flow rates. Additional testing in the lab produced a linear calibration curve that could be used for data correction, if the pressure drop was later determined significant. During tests 3 and 6 the flow rate was well beyond the capabilities of the flowmeter, and the tests were run with the flowmeter removed and flow estimated from water usage.

A CR10 datalogger was used at Site 1 to monitor BH-1. It has capabilities similar to the CR10X. The flow and barometric pressure were only measured using the CR10X.

During each test, the CR10X was programmed to measure the pressure and temperature of all three pressure transducers from one borehole, the flow rate, and the barometric pressure. It then calculated a temperature-corrected pressure for each pressure transducer and calculated the pressure change by subtracting the initial pressure reading at the start of the test. All data were then put into storage. During the initial phase of each test, when the rate of change in pressure was most rapid, the datalogger took measurements every minute to increase the resolution of the data. In later stages of the test, when the pressure change rate had slowed, measurements were taken every 10 minutes.

Packer strings were inserted in BH-1, BH-2, and BH-4 configured for the observation intervals, and packers inserted in BH-3 and BH-5 were positioned for injection as shown in Table 7 and Table 8 and Figure 10 and Figure 11. Positions were

TABLE 7 PACKER POSITIONS MEASURED DOWN BOREHOLE

	BH-1 (m)	BH-2 (m)	BH-3 (m)	BH-4 (m)	BH-5 (m)
First packer (top)	66.1	54.6	56.8	45.1	46.0
First packer (bottom)	67.1	55.5	58.4	46.0	47.9
Second packer (top)	67.7	56.4	59.0	46.6	48.5
Second packer (bottom)	68.6	57.3	60.5	47.5	49.7
Third packer (top)	69.2	58.2		48.2	
Third packer (bottom)	70.1	59.1		49.1	
Fourth packer (top)	70.7	60.0		49.7	
Fourth packer (bottom)	71.6	61.0		50.6	

chosen based on the results of core logging. The injection strings were repositioned between tests, so each test had different distances between injection and monitoring zones (Table 9).

Testing Procedures

Three tests were conducted at each site, for six tests total. Each test was scheduled to run six days, but the test would be terminated early if equilibrium conditions were reached. Water was injected into a different zone (footwall, fault core, or hanging wall) for each of the three tests at each site. After a test was completed at one site, the equipment was moved to the other site for the next test. This allowed the water table to return to its static level between tests. Due to the need to cycle equipment between sites, the actual head varied for each test (Table 10). Each test cycle began by measuring the depth to water inside the injection pipe, as a final check that the water levels had completely recovered from the previous test. The transducer pressure for each monitoring zone was recorded and the values incorporated into the datalogger programming as a baseline for measuring the pressure changes during the test.

The testing required simulating an instantaneous increase of pressure to the

TABLE 8 POSITION OF BOREHOLES AND SIGNIFICANT FEATURES

Well	Significance	Borehole Depth (m)	East (m)	North (m)	Vertical (m)
BH-1	Ground Surface	0.00	14.943	20.437	-2.547
BH-1	Water Table	43.59	33.092	9.896	-40.725
BH-1	Transducer Bundle	47.24	36.588	7.579	-48.576
BH-1	Center of Zone 3	67.36	42.295	3.754	-61.761
BH-1	Fault/Center of Zone 2	68.89	42.870	3.490	-63.116
BH-1	Center of Zone 1	70.41	43.450	3.051	-64.471
BH-1	Total Depth	98.78	53.681	-4.063	-89.990
BH-2	Ground Surface	0.00	45.295	-2.809	-2.502
BH-2	Water Table	38.10	45.292	-2.810	-40.604
BH-2	Transducer Bundle	41.45	45.291	-2.810	-43.957
BH-2	Center of Zone 3	55.93	45.290	-2.810	-58.436
BH-2	Fault	57.61	45.290	-2.810	-60.112
BH-2	Center of Zone 2	57.76	45.290	-2.810	-60.282
BH-2	Center of Zone 1	59.59	45.294	-2.810	-62.325
BH-2	Total Depth	62.79	45.300	-2.810	-65.900
BH-3	Ground Surface	0.00	43.202	-3.151	-2.610
BH-3	Water Table	38.10	42.873	-2.994	-40.708
BH-3	Center of Zone 3	57.15	42.538	-3.185	-59.722
BH-3	Fault/ Center of Zone 2	58.67	42.512	-3.209	-61.270
BH-3	Center of Zone 1	60.20	42.477	-3.230	-62.797
BH-3	Total Depth	68.33	42.320	-3.360	-70.900
BH-4	Ground Surface	0.00	-292.383	-44.548	-3.128
BH-4	Water Table	33.53	-291.009	-49.881	-36.198
BH-4	Tansducer Bundle	36.88	-290.929	-50.363	-39.515
BH-4	Center of Zone 3	46.33	-290.750	-51.673	-49.239
BH-4	Fault/Center of Zone 2	47.85	-290.720	-51.890	-50.900
BH-4	Center of Zone 1	49.38	-290.698	-52.058	-51.894
BH-4	Total Depth	63.25	-290.528	-53.819	-65.511
BH-5	Ground Surface	0.00	-288.869	-52.695	-2.525
BH-5	Water Table	33.53	-289.513	-53.172	-36.026
BH-5	Center of Zone 3	46.63	-290.795	-53.290	-49.015
BH-5	Fault/Center of Zone 2	48.16	-290.890	-53.300	-50.500
BH-5	Center of Zone 1	49.68	-290.987	-53.339	-52.149
BH-5	Total Depth	62.24	-291.825	-53.503	-64.681

Note: East, North and Vertical refer to distance from the survey origin.

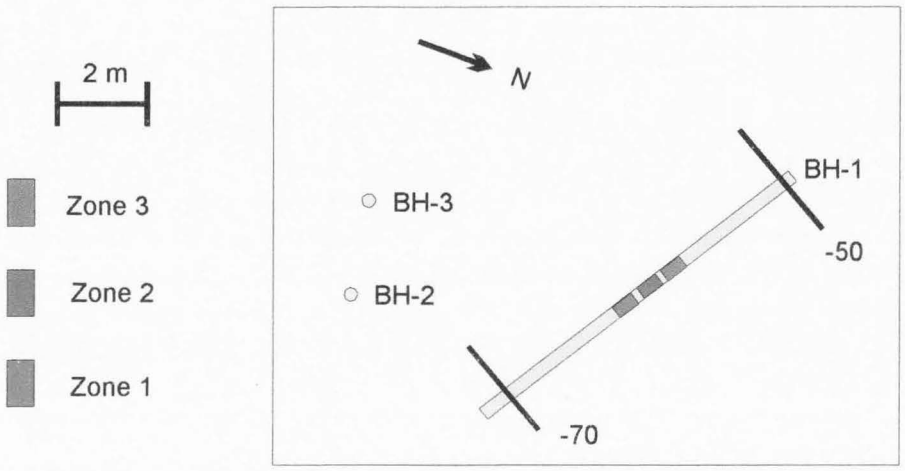

Plan View

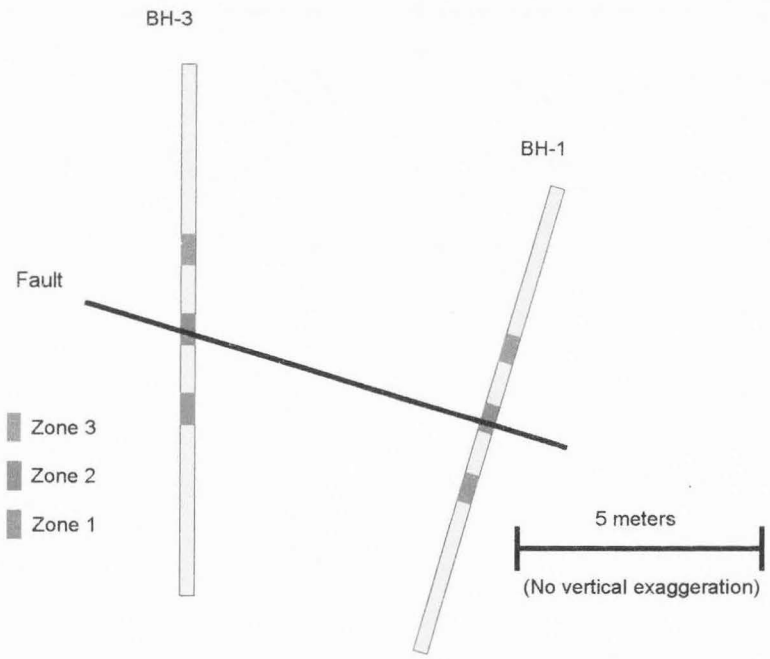

Cross-Section

Figure 10 Plan view and cross-section of boreholes at tip zone (Site 1). Plan view shows BH-1 between 50 and 70 m depth. (BH-1 projected onto the plane of the cross-section).

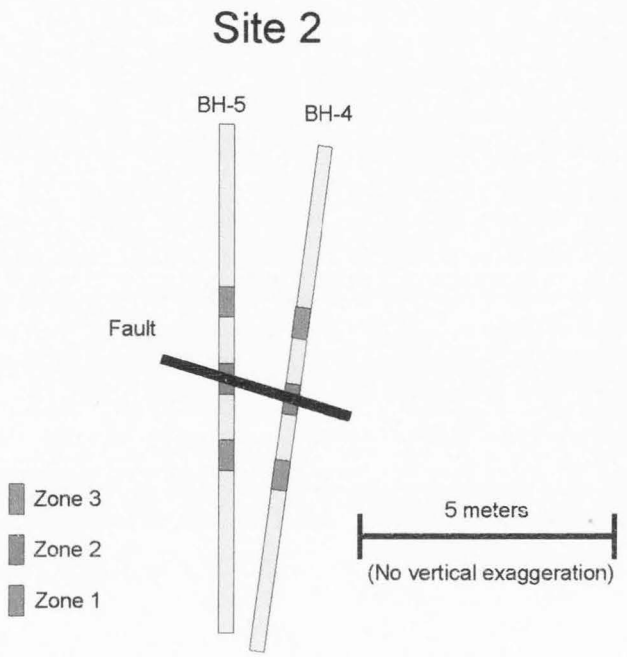

Figure 11 Cross-section of boreholes and injection zones at wash (Site 2) (BH-4 is projected onto plane perpendicular to fault).

injection zone, but the flowmeter acted as a flow limiter for this portion of the test. To solve this problem, the standpipe used for direct head measurement was removed at the top of the tee connecting the pipe, the standpipe, and the flowmeter. The test began with the initiation of the datalogger. Water was then poured directly into the tee from tanks to allow fast filling. The standpipe was then reconnected and the system reached equilibrium by water passing from the constant head tank and through the flowmeter. The entire process took only a few minutes, and the actual, non-instantaneous head increase was not observable in the final data curves. Injection heads were then determined by measuring the water level in the standpipe.

Because of the difficulty in supplying water to the test sites, water usage was minimized. After the system reached equilibrium, the inflow valve to the constant head tank was adjusted to minimize the overflow out of the constant head tank. This generally

TABLE 9 DISTANCES BETWEEN ZONE CENTERS IN THE INJECTION AND MONITORING WELLS

Site	Injection Well	Injection Zone	Monitoring Well	Monitoring Zone	Separation (m)
1	BH-3	Fault	BH-1	Footwall	7.09
1	BH-3	Fault	BH-1	Fault	6.96
1	BH-3	Fault	BH-1	Hanging wall	6.98
1	BH-3	Fault	BH-2	Footwall	3.00
1	BH-3	Fault	BH-2	Fault	2.98
1	BH-3	Fault	BH-2	Hanging wall	3.99
1	BH-3	Footwall	BH-1	Footwall	6.57
1	BH-3	Footwall	BH-1	Fault	6.74
1	BH-3	Footwall	BH-1	Hanging wall	7.06
1	BH-3	Footwall	BH-2	Footwall	2.89
1	BH-3	Footwall	BH-2	Fault	3.80
1	BH-3	Footwall	BH-2	Hanging wall	5.21
1	BH-3	Hanging wall	BH-1	Footwall	7.89
1	BH-3	Hanging wall	BH-1	Fault	7.50
1	BH-3	Hanging wall	BH-1	Hanging wall	7.24
1	BH-3	Hanging wall	BH-2	Footwall	3.81
1	BH-3	Hanging wall	BH-2	Fault	2.83
1	BH-3	Hanging wall	BH-2	Hanging wall	3.06
2	BH-5	Fault	BH-4	Footwall	1.88
2	BH-5	Fault	BH-4	Fault	1.48
2	BH-5	Fault	BH-4	Hanging wall	2.06
2	BH-5	Footwall	BH-4	Footwall	1.34
2	BH-5	Footwall	BH-4	Fault	1.93
2	BH-5	Footwall	BH-4	Hanging wall	3.36
2	BH-5	Hanging wall	BH-4	Footwall	3.13
2	BH-5	Hanging wall	BH-4	Fault	2.35
2	BH-5	Hanging wall	BH-4	Hanging wall	1.63

took several minutes of trial-and-error, and then required no further adjustment for the remainder of the test.

The dataloggers accomplished all further data collection. Test progress was monitored in real time several times daily by interfacing the laptop computer with the data logger. This provided a check for malfunctions in the monitoring equipment, and

TABLE 10 INJECTION HEADS FOR TESTS

Test	Site	Injection Zone	Start Date	Injection Head (m)	Test Duration (min)
1	2	2	9/12/99	35.69	9841
2	1	2	9/23/99	39.93	10069
3	2	1	10/07/99	36.33	3786
4	1	1	10/10/99	39.93	9776
5	2	3	11/06/99	34.17	4273
6	1	3	11/12/99	38.41	6079

allowed ending the tests early, if an equilibrium state had been reached.

RESULTS

Overview

Response curves are shown in Figure 12 to Figure 19. Measured responses were obtained in 19 of 27 observation intervals during the six tests, 12 of 18 at the fault tip (Site 1), and 7 of 9 for the wash (Site 2). Several problems occurred during testing. First, usable results for fault injection (Zone 2) at the fault tip (Site 1) in BH-1 were not obtained due to wiring problems with the datalogger. Second, a loss of pressure head during fault injection (Zone 2) at the wash (Site 2) resulted in a temporary dip in pressure values at ~ 4400 min (Figure 17). A programming error in the CR10 resulted in a loss of data for the first 38 minutes of the hanging wall injection (Zone 3) test at the fault tip (Site 1) for BH-1 (Figure 15).

Response Descriptions

Each curve represents the increase in pressure head in a specific monitoring zone during injection into one of the injection zones (fault, footwall or hanging wall). The curves vary greatly in shape. The footwall injection curves show a sharp initial rise in pressure attributed to the use of constant head injection. There is also a slight dip in the hanging wall (Zone 3) curve during hanging wall injection (Zone 3) at the tip zone (Site 1) in BH-2 (Figure 16) between 7 and 30 minutes. The most striking curve is the fault response (Zone 2) with hanging wall injection (Zone 3) at the wash (Site 2) (Figure 19). The curve has a series of jagged jumps in pressure response.

Response times are summarized in Table 12. Several zones at each site showed no pressure response. In these cases, no hydraulic connection exists between the

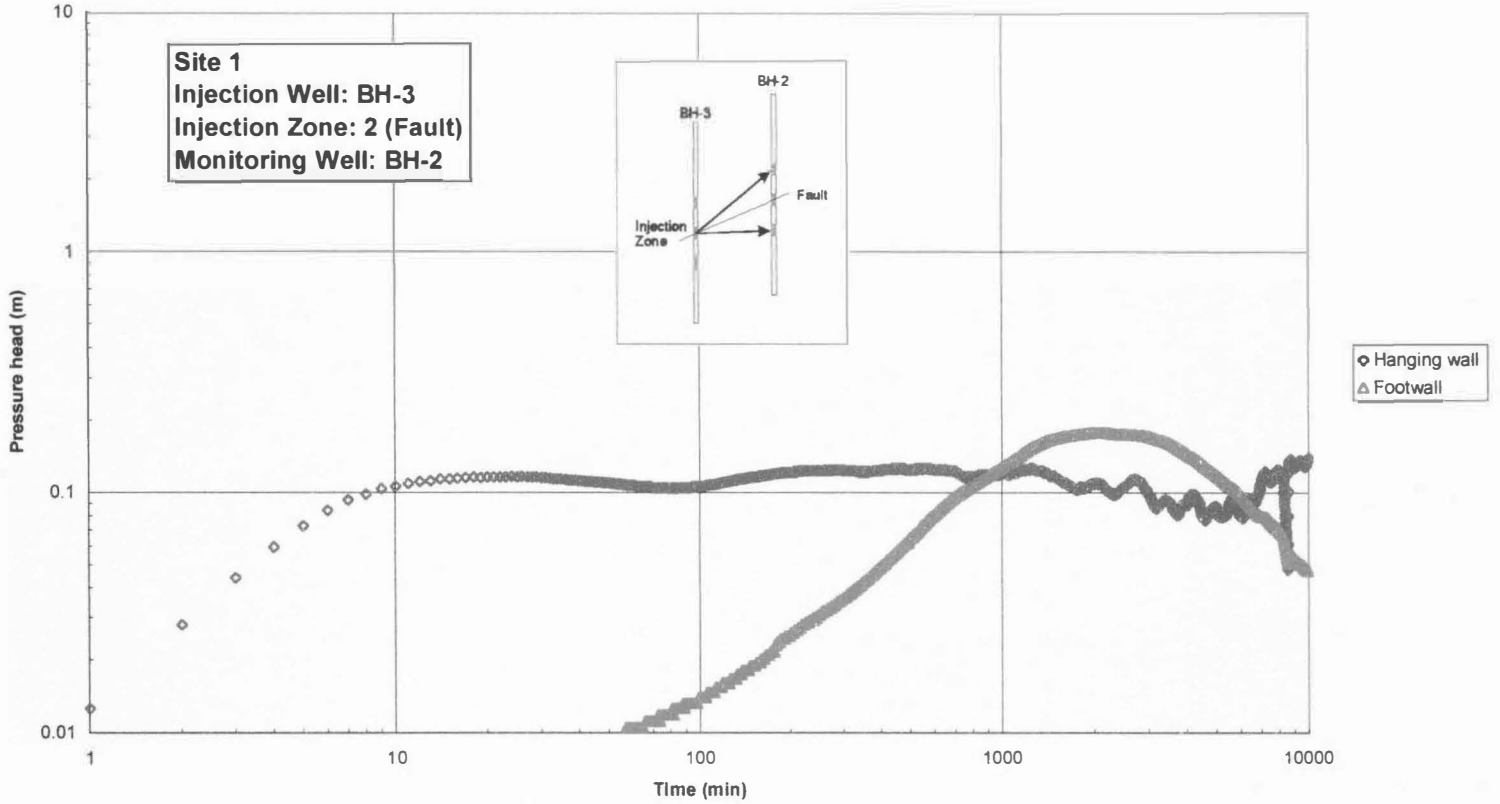

Figure 12 Test 2 pressure head response for fault injection (Zone 2) at tip zone (Site 1) monitored in BH-2.

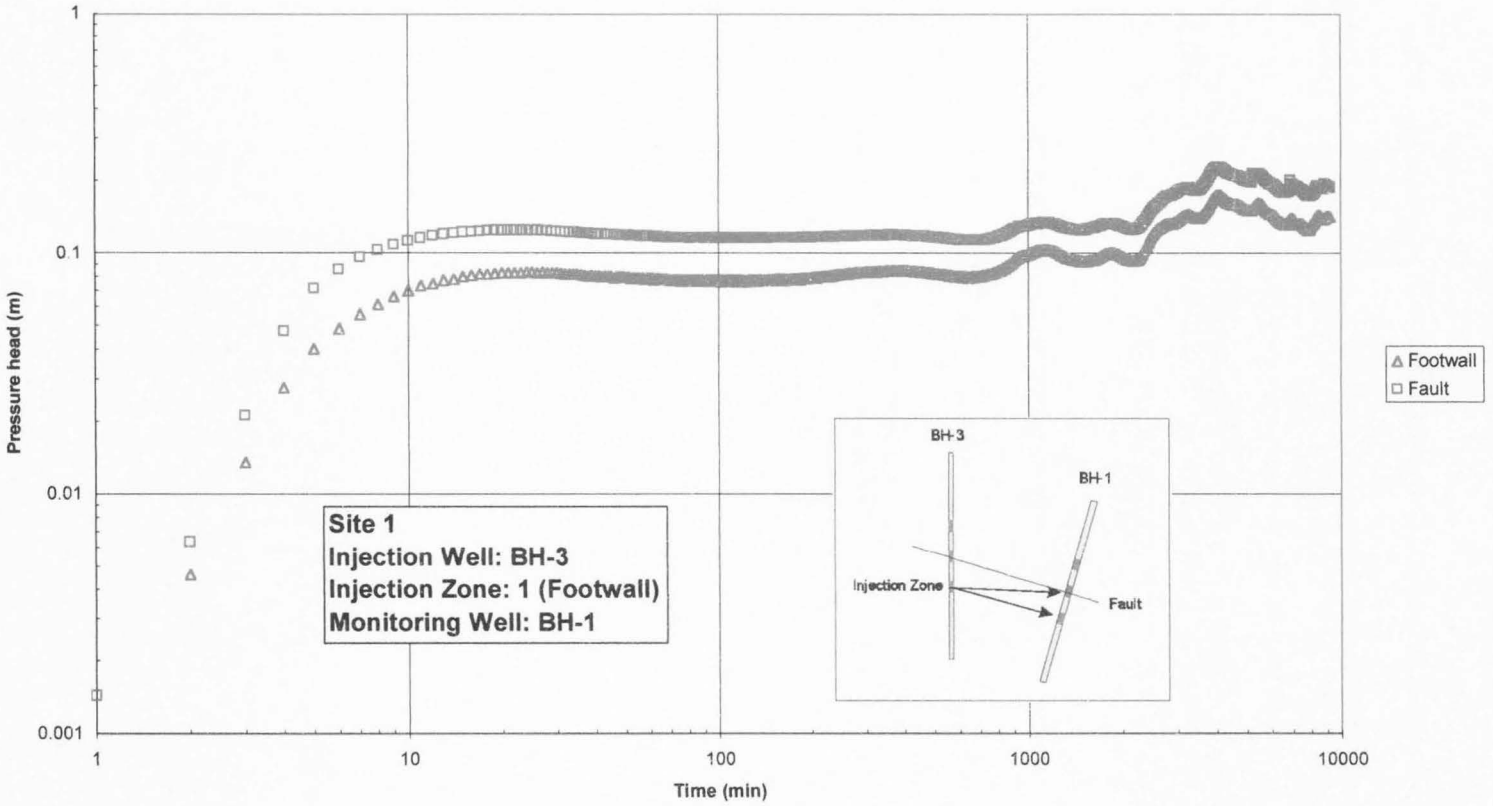

Figure 13 Test 4 pressure head response for footwall injection (Zone 1) at tip zone (Site 1) monitored in BH-1.

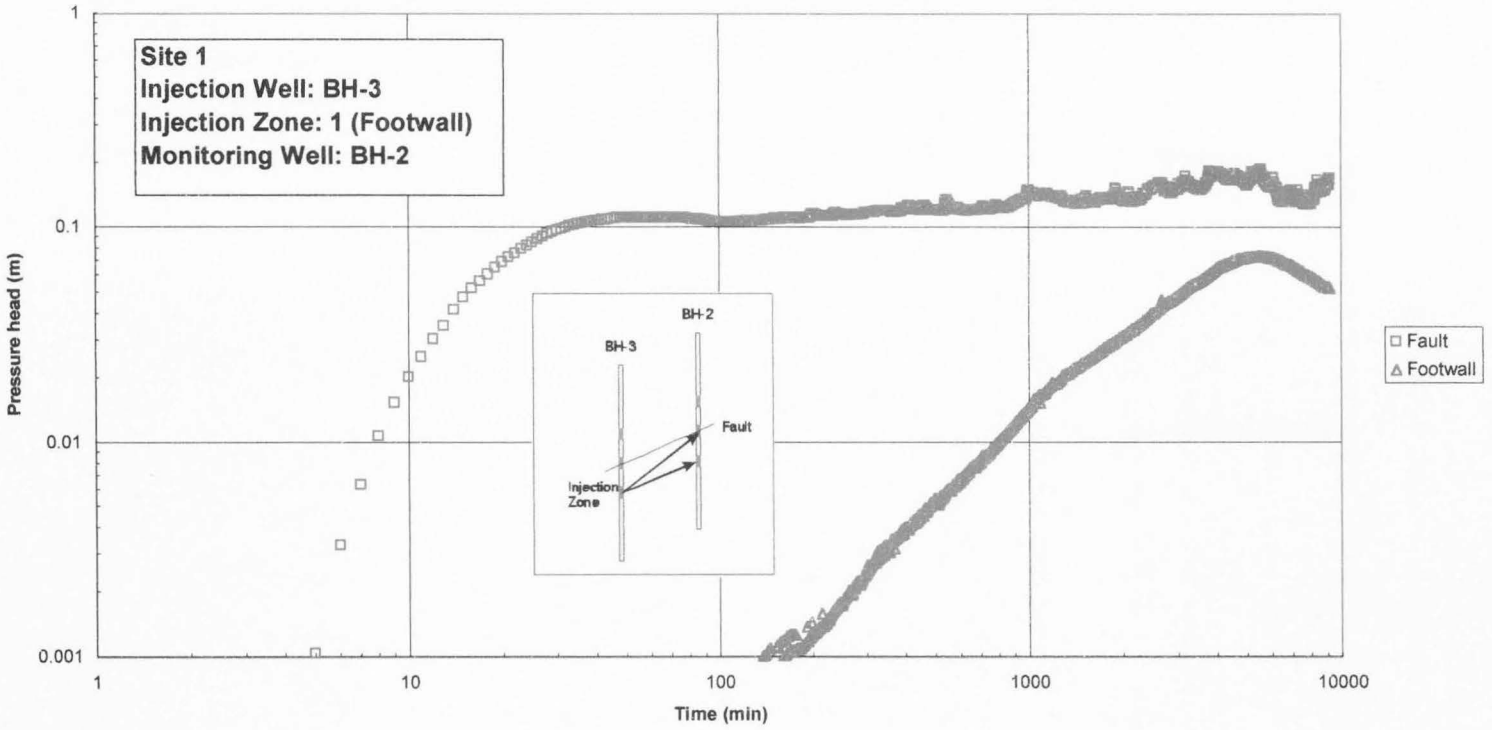

Figure 14 Test 4 pressure head response for footwall injection (Zone 1) at tip zone (Site 1) monitored in BH-2.

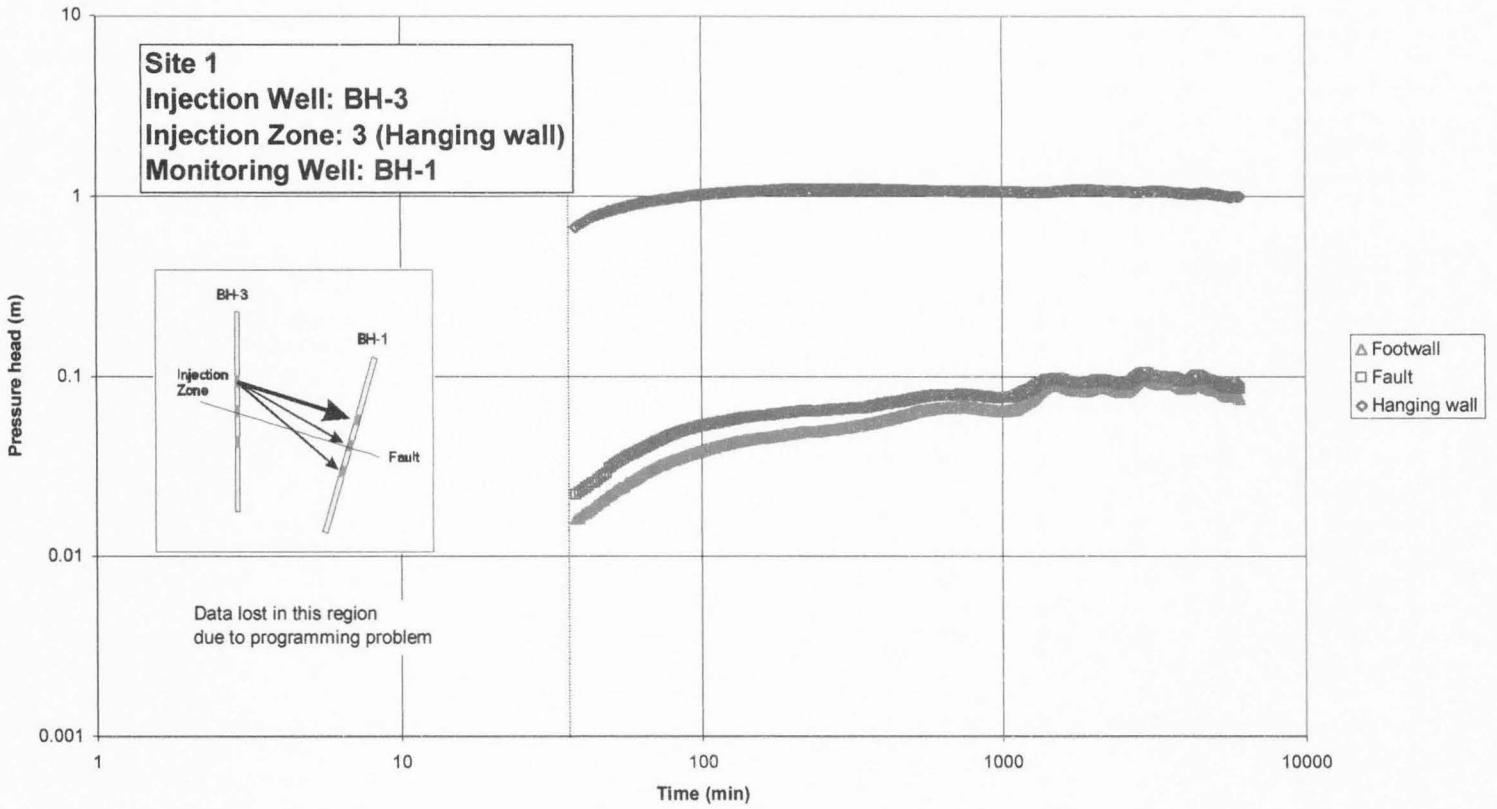

Figure 15 Test 6 pressure head response for hanging wall injection (Zone 3) at tip zone (Site 1) monitored in BH-1.

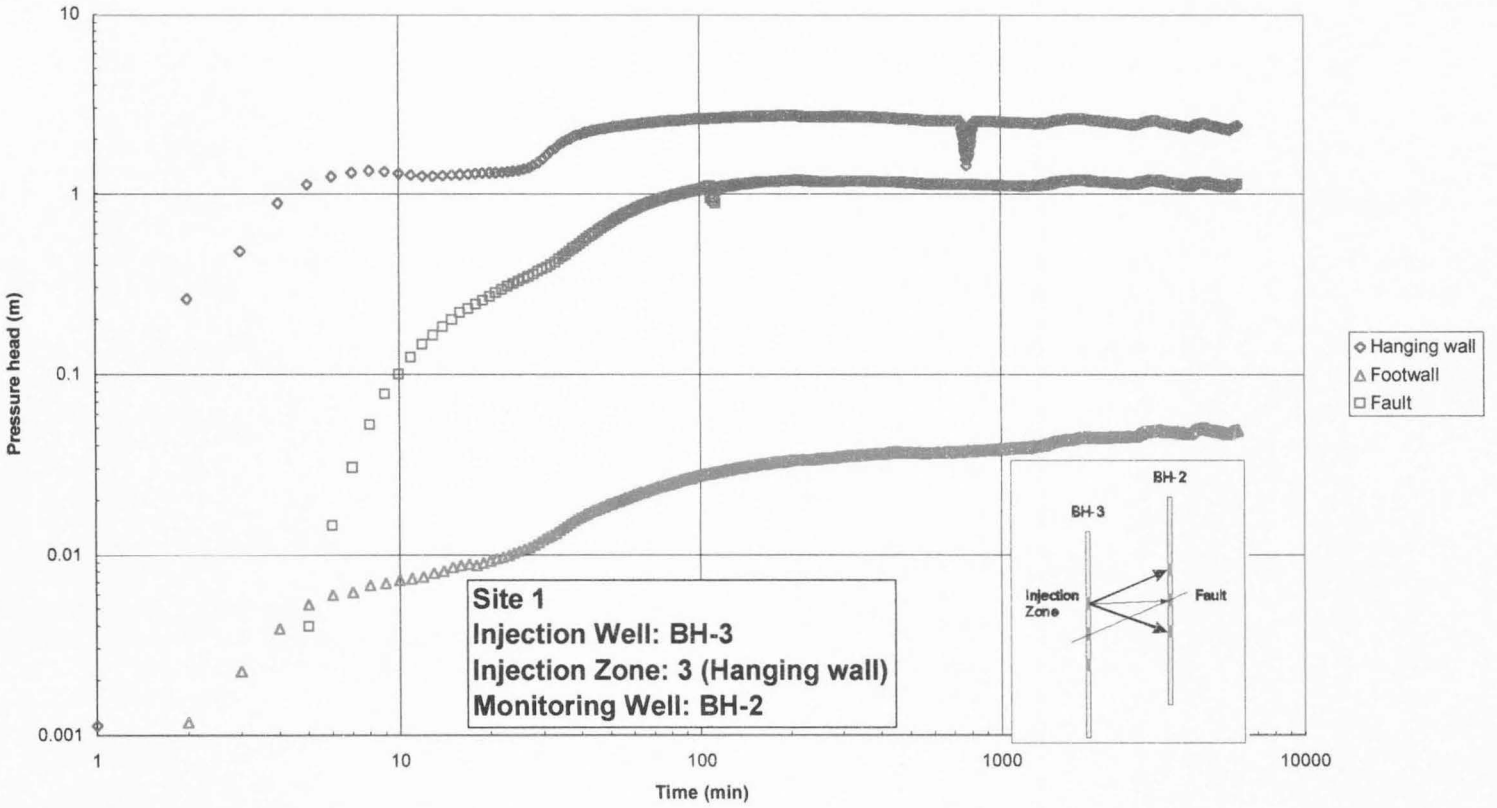

Figure 16 Test 6 pressure head response for hanging wall injection (Zone 3) at tip zone (Site 1) monitored in BH-2.

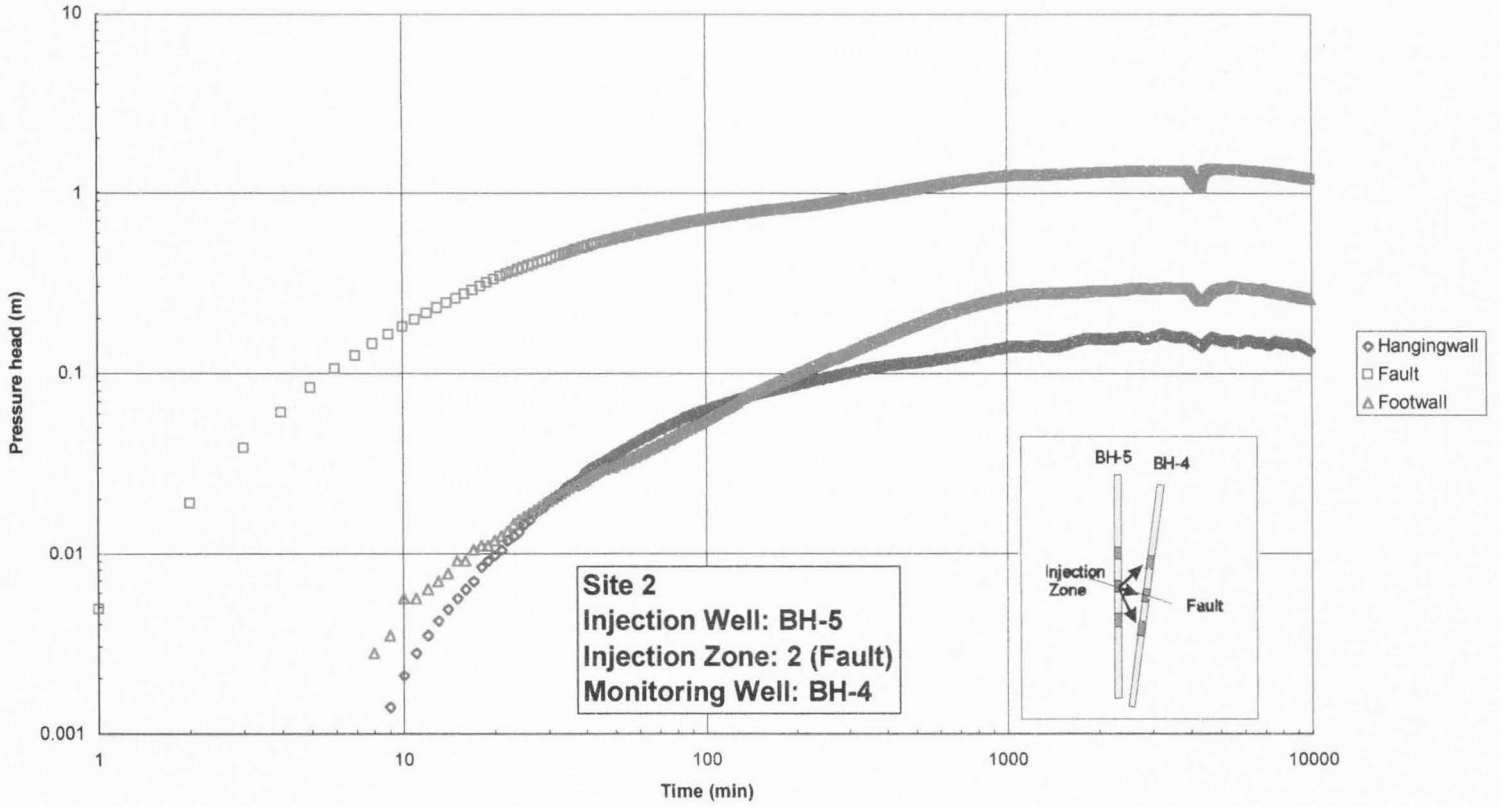

Figure 17 Test 1 pressure head response for fault injection (Zone 2) at wash (Site 2) monitored in BH-4.

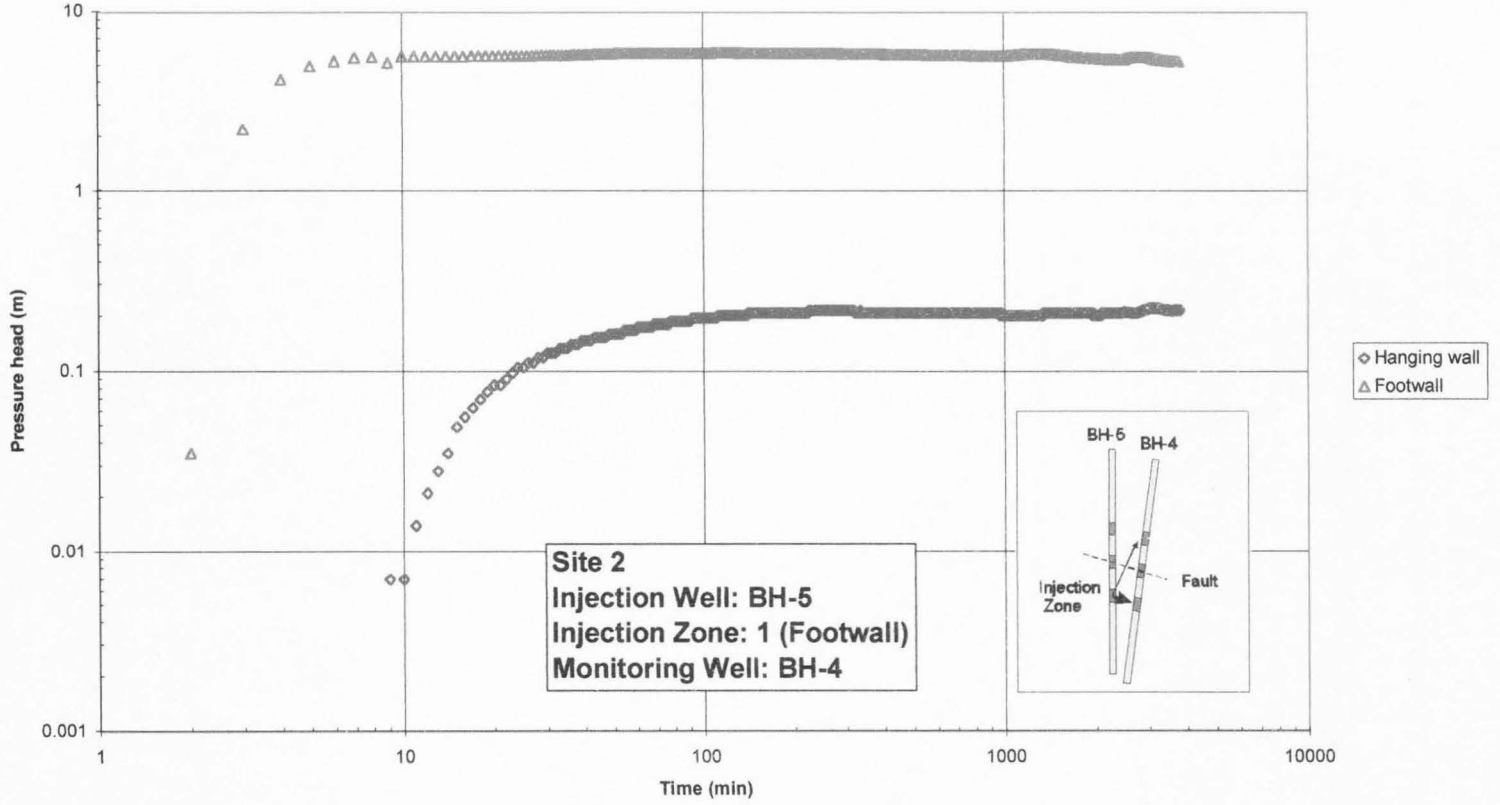

Figure 18 Test 3 pressure head response for footwall injection (Zone 1) at wash (Site 2) monitored in BH-4.

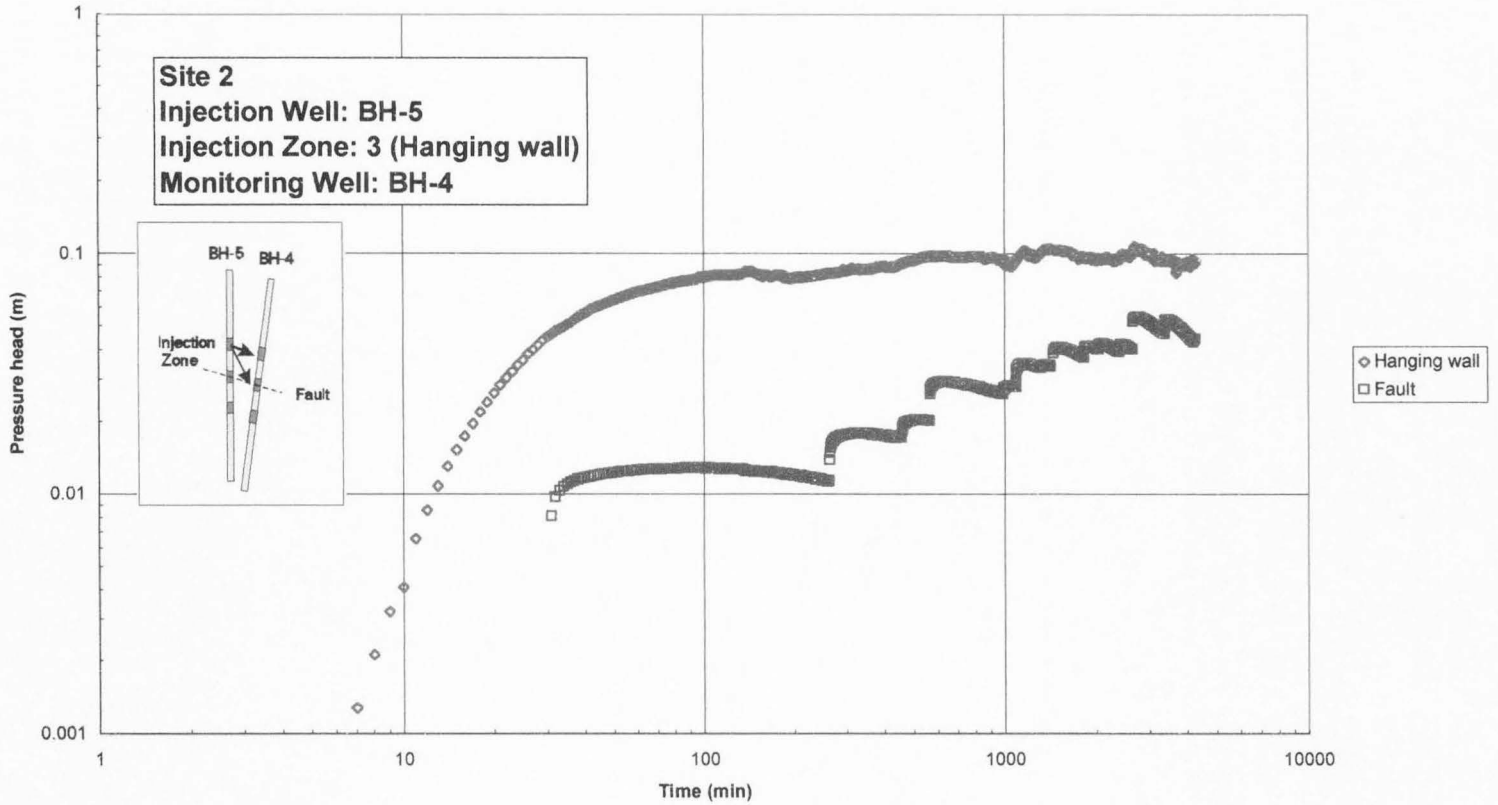

Figure 19 Test 5 pressure head response for hanging wall injection (Zone 3) at wash (Site 2) monitored in BH-4.

TABLE 11 TIME AND PRESSURE VALUES FOR FAULT TIP (SITE 1) AND WASH (SITE 2)

Site	Test	Injection Well	Injection Zone	Monitoring Well	Monitoring Zone	T_i (min)	T_{max} (min)	P_{max} (m H_2O)
1	2	BH-3	Fault	BH-2	Footwall	57	1945	0.18
1	2	BH-3	Fault	BH-2	Fault	No response	N.A.	N.A.
1	2	BH-3	Fault	BH-2	Hanging wall	1	24	0.12
1	4	BH-3	Footwall	BH-1	Footwall	2	26	0.08
1	4	BH-3	Footwall	BH-1	Fault	1	23	0.13
1	4	BH-3	Footwall	BH-1	Hanging wall	No response	N.A.	N.A.
1	4	BH-3	Footwall	BH-2	Footwall	138	5496	0.07
1	4	BH-3	Footwall	BH-2	Fault	5	57	0.11
1	4	BH-3	Footwall	BH-2	Hanging wall	No response	N.A.	N.A.
1	6	BH-3	Hanging wall	BH-1	Footwall	Unknown*	2949	0.10
1	6	BH-3	Hanging wall	BH-1	Fault	Unknown*	2979	0.10
1	6	BH-3	Hanging wall	BH-1	Hanging wall	Unknown*	210	1.10
1	6	BH-3	Hanging wall	BH-2	Footwall	2	4369	0.05
1	6	BH-3	Hanging wall	BH-2	Fault	4	213	1.18
1	6	BH-3	Hanging wall	BH-2	Hanging wall	1	207	2.75
2	1	BH-5	Fault	BH-4	Footwall	8	3282	0.30
2	1	BH-5	Fault	BH-4	Fault	1	3782	1.33
2	1	BH-5	Fault	BH-4	Hanging wall	9	3552	0.17
2	3	BH-5	Footwall	BH-4	Footwall	2	10	5.60
2	3	BH-5	Footwall	BH-4	Fault	No response	N.A.	N.A.
2	3	BH-5	Footwall	BH-4	Hanging wall	9	222	0.22
2	5	BH-5	Hanging wall	BH-4	Footwall	No response	N.A.	N.A.
2	5	BH-5	Hanging wall	BH-4	Fault	32	2724	0.05
2	5	BH-5	Hanging wall	BH-4	Hanging wall	7	2684	0.11

* Data not available due to programming error

injection zone and the monitoring zone in the volume being tested. Initial response time in the other zones ranged from less than 1 minute to 138 minutes. Maximum pressure responses ranged from 0.05 to 5.60 m. The time to reach maximum pressure ranged from 10 to 5500 minutes.

Fault injection (Zone 2) at the tip zone (Site 1) (Figure 12) produced a low response (< 0.2 m) in the footwall (Zone 1) and the hanging wall (Zone 3). There was no response in the fault (Zone 2). The footwall response occurred much later (t > 50 min), rising to a maximum and then falling off later. This test had equipment problems and no

results were obtained from BH-1.

Footwall injection (Zone 1) at the tip zone (Site 1) (Figure 13 and Figure 14) produced weak responses (< 0.2 m) in the footwall (Zone 1) and the fault (Zone 2) at both boreholes. There was no response in the hanging wall (Zone 3) at either borehole. This would indicate the fault zone acted as a barrier to flow normal to the fault plane. The footwall (Zone 1) response time in BH-2 is ~ two orders of magnitude larger than the others (t > 100 min).

Hanging wall injection (Zone 3) at the tip zone (Site 1) (Figure 15 and Figure 16) produced the strongest responses (> 1 m) in the hanging wall (Zone 3) of both BH-1 and BH-2 and the fault (Zone 2) at BH-2. These were also characterized by fast response times (t < 10 min in BH-2). The response in the footwall (Zone 1) of both boreholes and the fault (Zone 2) in BH-1 was an order of magnitude less (≤ 0.1 m).

During fault injection (Zone 2) at the wash (Site 2), all three zones showed responses in t < 10 min (Figure 17). The fault had the strongest response (> 1 m) and the other two zones had responses ~ one order of magnitude less (~ 0.1 m).

Footwall injection (Zone 1) at the wash (Site 2) (Figure 18) produced responses in the hanging wall (Zone 3) and the footwall (Zone 1). The footwall (Zone 1) showed the strongest response of all the tests (~ 5 m), and had a fast response time (t < 2 min). The hanging wall (Zone 3) response was an order of magnitude less (~ 0.2 m). No response was recorded in the fault (Zone 2).

During hanging wall injection (Zone 3) at the wash (Site 2) (Figure 19), the fault (Zone 2) response showed one of the most distinctive of all the results. The curve increases in a series of steps. This is the strongest indication of the heterogeneity of the

fault zone seen in any of the data curves. In contrast, the hanging wall (Zone 3) curve shows a smooth and steady increase in pressure head at early times ($t < 40$ min) and then flattens. No response occurred in the footwall (Zone 1), which is consistent with the fault acting as a barrier to flow normal to the fault plane.

Injection Rates

Injection rates for each injection zone provide a qualitative measure of which zones are acting as barriers to flow and where the maximum flow is occurring. At Site 1 (Table 12), the largest flow occurs in the hanging wall (Zone 3), where the injection rate is an order of magnitude larger than in the other two zones. This test also injected the largest volume of water (9.5 m^3), indicating a higher porosity in the hanging wall. The response in the monitoring zones is also highest in the hanging wall (Figure 15 and Figure 16). When injecting into the footwall (Zone 1), the fault acts as a barrier to flow, and no response is seen in the hanging wall (Figure 13 and Figure 14).

Injection at Site 2 (Table 12) is highest in the footwall, by an order of magnitude. The largest head response is also in the footwall (Figure 18), and the second largest injected volume of water (3.7 m^3). This seems to indicate the footwall has a

TABLE 12 INJECTION RATES

Test	Site	Injection Zone	Injection Well	Start Date	Total Head (m)	Injection Rate (m^3/s)	Test Duration (min)	Total volume Injected (m^3)
1	2	Fault	BH-5	9/12/99	35.69	1.9E-06	9841	1.12
2	1	Fault	BH-3	9/23/99	39.93	1.6E-06	10069	0.95
3	2	Footwall	BH-5	10/7/99	36.33	1.6E-05	3786	3.71
4	1	Footwall	BH-3	10/10/99	39.93	1.3E-06	9776	0.74
5	2	Hanging wall	BH-5	11/6/99	34.17	6.2E-07	4273	0.16
6	1	Hanging wall	BH-3	11/12/99	38.41	2.6E-05	6079	9.51

higher porosity than the other two zones, possibly indicating a higher fracture density.

The two sites have opposite responses to injection, with high porosity in the hanging wall at the tip zone (Site 1) and high porosity in the footwall in the wash (Site 2).

Hsieh Type Curve

The cross-hole packer method (Hsieh and Neuman, 1985; Hsieh et al., 1985) uses type curve matching to obtain dimensionless head and time values. The assumption is made that the tested volume can be modeled as an equivalent continuum on the scale of the test. The dimensionless form is derived from the governing flow equation for a homogeneous, anisotropic medium assuming an initial uniform head distribution and an infinite flow domain. The solution used for this analysis is for point injection/point observation. The solution can be written in the dimensionless form:

$$\Delta h_{pd}=\text{erfc}\{1/(4t_d)^{1/2}\}$$

where Δh_{pd} is the dimensionless head and t_d is the dimensionless time. These terms are defined as:

$$\Delta h_{pd} = (4\pi R\Delta h/Q)[D/K_d(e)]^{1/2}$$

and

$$t_d = K_d(e)t/(R^2S_s).$$

where R is the separation distance between the center of the injection zone and the center of the monitoring interval, Δh is the change in head with time, Q is the injection rate, **K** is the hydraulic conductivity tensor, D is the determinant of **K**, $K_d(e)$ is the directional hydraulic conductivity in the e direction, S_s is the specific storage of the rock, and t is time.

The type curve matches are shown in Figure A-1 through Figure A-19 in

Appendix A, and the values for t and Δh are shown in Table 13. The type curve was designed for constant discharge testing, and when used for constant head injection the initial values may be higher than the curve. Matching is done based on the initial response time and the later time steady-state value of the pressure head. The quality of the match between the type curve and the data curves is Hsieh's first criterion for considering the volume to be an equivalent continuum.

During fault injection (Zone 2) at the tip zone (Site 1), the hanging wall (Zone 3) matched the type curve for $t < 10$ minutes and then flattened (Figure A-2). This suggests a constant head boundary according to Hsieh and Neuman's (1985) theory. Since no source of water exists at the test sites that could create this condition, this flattening may result from the radius of influence intersecting a conduit, such as a fracture network. The footwall (Zone 1) does not match the type curve (Figure A-1), and the fault (Zone 2) had no response.

During footwall injection (Zone 1) at the tip zone (Site 1) (Figure A-3 and Figure A-5) the fault (Zone 2) matches the type curve for $t < 20$ min in both boreholes. After that time the curves flatten. The footwall (Zone 1) in BH-1 matches the type curve for $t <$ 10 min and then flattens (Figure A-4). The footwall (Zone 1) in BH-2 does not match the type curve, and the late initial response time ($t > 100$ min) indicates a longer flow path than the others (Figure A-6). The hanging wall (Zone 3) had no response in either BH-1 or BH-2.

During hanging wall injection (Zone 3) at the tip zone (Site 1), the footwall (Zone 1) response in BH-1 matched the type curve (Figure A-8). The responses in the fault (Zone 2) and the hanging wall (Zone 3) in BH-1 matched the type curve for $t < 100$ min

TABLE 13 MATCH POINTS FOR HSIEH TYPE CURVES ($T_D = 1$, $\Delta H_{PD} = 1$)

Site	Test	Injection Well	Injection Zone	Monitoring Well	Monitoring Zone	Time (min)	Δh (m)
1	2	BH-3	Fault	BH-2	Footwall	1800	0.37
1	2	BH-3	Fault	BH-2	Hanging wall	8	0.20
1	4	BH-3	Footwall	BH-1	Footwall	22	0.25
1	4	BH-3	Footwall	BH-1	Fault	20	0.40
1	4	BH-3	Footwall	BH-2	Footwall	5000	0.14
1	4	BH-3	Footwall	BH-2	Fault	90	0.50
1	6	BH-3	Hanging wall	BH-1	Footwall	150	0.09
1	6	BH-3	Hanging wall	BH-1	Fault	160	0.14
1	6	BH-3	Hanging wall	BH-1	Hanging wall	70	2.0
1	6	BH-3	Hanging wall	BH-2	Footwall	22	0.04
1	6	BH-3	Hanging wall	BH-2	Fault	82	1.8
1	6	BH-3	Hanging wall	BH-2	Hanging wall	12	3.0
2	1	BH-5	Fault	BH-4	Footwall	350	0.34
2	1	BH-5	Fault	BH-4	Fault	50	1.4
2	1	BH-5	Fault	BH-4	Hanging wall	140	0.17
2	3	BH-5	Footwall	BH-4	Footwall	30	80
2	3	BH-5	Footwall	BH-4	Hanging wall	80	0.50
2	5	BH-5	Hanging wall	BH-4	Fault	110	0.05
2	5	BH-5	Hanging wall	BH-4	Hanging wall	110	0.25

and then flattened (Figure A-7 and Figure A-9). None of the responses in BH-2 matched the type curve (Figure A-10) through Figure A-12). All three show a dip in response before climbing to their final values that isn't compatible with Hsieh and Neuman's technique.

During fault injection (Zone 2) at the wash (Site 2), the hanging wall (Zone 3) matched the type curve (Figure A-15). The fault (Zone 2) showed a higher response for t < 12 min and then roughly matched the type curve (Figure A-13). The footwall did not match the type curve (Figure A-14).

During footwall injection (Zone 1) at the wash (Site 2), neither the footwall (Zone 1) nor the hanging wall (Zone 3) matched the type curve well (Figures A-16 and A-17). Both response curves flattened at later times. The fault (Zone 2) had no response.

During hanging wall injection (Zone 3) at the wash (Site 2), the hanging wall (Zone 3) matched the type curve for early times ($t < 30$ min) and flattened (Figure A-19). The fault (Zone 2) did not match (Figure A-18). The footwall (Zone 1) had no response.

From the values for t and Δh obtained from the type curve matches (Table 13), the inverse diffusivity tensor, $\mathbf{U} = S_s\mathbf{K}^{-1}$, is computed according to the method outlined by Hsieh et al. (1985), and then S_s and $\mathbf{K}$ are computed (Appendices B and C). At least six measurements are adequate to determine the hydraulic conductivity tensor. An ordinary least squares method was used to compute $\mathbf{K}$ for these tests to allow using more than six measurements to try and obtain a better fit.

The computed values for the tip zone (Site 1) resulted in a negative value for $\mathbf{K}$, and the wash (Site 2) had imaginary values for both S_s and $\mathbf{K}$ (Figure 20). The conclusion is that the fault can not be represented as an equivalent, continuous anisotropic medium on the scale of this test, despite the close matches on many of the curves. The fault is responding differently depending on the injection zone.

$$Ss = 6.72\times 10^{-3}$$

$$K = \begin{pmatrix} -5.609\times 10^{-6} & 7.86\times 10^{-5} & -2.853\times 10^{-5} \\ 7.86\times 10^{-5} & -2.588\times 10^{-4} & 9.647\times 10^{-5} \\ -2.853\times 10^{-5} & 9.647\times 10^{-5} & -4.967\times 10^{-5} \end{pmatrix}$$ **Site 1**

$$Ss = 3.22i\times 10^{-4}$$

$$K = \begin{pmatrix} 4.646i\times 10^{-8} & 1.39i\times 10^{-6} & -1.132i\times 10^{-6} \\ 1.39i\times 10^{-6} & 2.194i\times 10^{-5} & -8.234i\times 10^{-6} \\ -1.132i\times 10^{-6} & -8.234i\times 10^{-6} & -8.069i\times 10^{-7} \end{pmatrix}$$ **Site 2**

Figure 20 Specific storage (S_s) and hydraulic conductivity tensors (K) for both sites.

Three types of deviations from the Hsieh type curve can be seen in the matches (Table 14). The data curve flattening below the type curve implies a constant head boundary (Freeze and Cherry, 1979). This may be a conduit acting as a sink for the water. In the fault zone such a conduit would most likely be a fracture network.

TABLE 14 DEVIATIONS FROM HSIEH TYPE CURVE

Site	Test	Injection Well	Injection Zone	Monitoring Well	Monitoring Zone	Feature
1	2	BH-3	Fault	BH-2	Footwall	early rise
1	2	BH-3	Fault	BH-2	Hanging wall	constant head boundary
1	4	BH-3	Footwall	BH-1	Fault	constant head boundary
1	4	BH-3	Footwall	BH-1	Footwall	constant head boundary
1	4	BH-3	Footwall	BH-2	Fault	constant head boundary
1	4	BH-3	Footwall	BH-2	Footwall	early rise
1	6	BH-3	Hanging wall	BH-1	Fault	constant head boundary
1	6	BH-3	Hanging wall	BH-1	Footwall	good match
1	6	BH-3	Hanging wall	BH-1	Hanging wall	constant head boundary
1	6	BH-3	Hanging wall	BH-2	Fault	double porosity
1	6	BH-3	Hanging wall	BH-2	Footwall	double porosity
1	6	BH-3	Hanging wall	BH-2	Hanging wall	double porosity
2	1	BH-5	Fault	BH-4	Fault	early rise
2	1	BH-5	Fault	BH-4	Footwall	early rise
2	1	BH-5	Fault	BH-4	Hanging wall	good match
2	3	BH-5	Footwall	BH-4	Footwall	constant head boundary
2	3	BH-5	Footwall	BH-4	Hanging wall	constant head boundary
2	5	BH-5	Hanging wall	BH-4	Fault	step pattern
2	5	BH-5	Hanging wall	BH-4	Hanging wall	constant head boundary

The second deviation type is a double porosity curve (Moench, 1984). The first section of the curve is flow in the fractures. The second, flat section, is water moving into the matrix block. The third section is a combination of flow in both the fractures and the matrix.

The third deviation is an early rise in the data curve above the type curve. This deviation can't be interpreted based on any existing models. One possibility is flow from a single vertical fracture in a low permability zone. This changes to pseudo-radial flow

with time.

The constant head boundary response appears in all three monitoring zones and in five of the six tests, the exception being Test 1 (fault (Zone 2) injection at the wash (Site 2)). Also, no constant head boundary response was noted in any of the three zones in BH-2 during Test 6 (hanging wall (Zone 3) injection at the tip zone (Site 1)).

The double porosity response appears in all three monitoring zones, but only in BH-2 at the tip zone (Site 1) during hanging wall (Zone 3) injection. The early rise response appears only in the footwall (Zone 1) at the tip zone (Site 1).

Theis Type Curves

Curve matches for the Theis (1935) type curve are shown in Appendix D (Figure D-1 through Figure D-19). The test procedure violates a number of the assumptions behind the Theis equation. Theis curves are primarily for confined aquifers with full penetration of the aquifer by the screened portion of the well. The curves are presented here to obtain a general idea of what values may exist in the aquifer and how the zones compare relative to each other. A correction for unconfined aquifers has been applied to the data curves (Jacob, 1944). The values for transmissivity and storativity are show in Table 15. The values for transmissivity range over four orders of magnitude and storativity ranges over three orders of magnitude. Transmissivity values obtained from previous low-discharge, short-term aquifer testing in unfaulted Navajo Sandstone ranged from 2.9×10^{-5} to 7.0×10^{-4} m^2/s (Hood and Patterson, 1984). The average values from these tests, 2.2×10^{-5} m/s^2 for transmissivity and 4.8×10^{-3} for storativity, compare favorably with those values.

TABLE 15 TRANSMISSIVITY AND STORATIVITY VALUES BASED ON THEIS CURVE MATCHING (W(U) = 1, 1/U = 1)

Test	Injection Zone	Site	Borehole	Monitoring Zone	Time (min)	Δh (m)	T (m^2/s)	S
2	Fault	1	BH-2	Footwall	250	0.12	1.0E-06	7.0E-03
2	Fault	1	BH-2	Hanging wall	0.9	0.05	2.5E-06	3.4E-05
4	Footwall	1	BH-1	Footwall	4.0	0.10	1.0E-06	2.2E-05
4	Footwall	1	BH-1	Fault	4.0	0.20	5.0E-07	1.1E-05
4	Footwall	1	BH-2	Footwall	700	0.040	2.5E-06	5.1E-02
4	Footwall	1	BH-2	Fault	12	0.14	7.2E-07	1.4E-04
6	Hanging wall	1	BH-1	Footwall	18	0.025	8.3E-05	5.8E-03
6	Hanging wall	1	BH-1	Fault	27	0.060	3.5E-05	4.0E-03
6	Hanging wall	1	BH-1	Hanging wall	10	0.65	3.2E-06	1.5E-04
6	Hanging wall	1	BH-2	Footwall	2.5	0.008	2.6E-04	1.1E-02
6	Hanging wall	1	BH-2	Fault	12	0.60	3.5E-06	1.2E-03
6	Hanging wall	1	BH-2	Hanging wall	1.8	0.90	2.3E-06	1.1E-04
1	Fault	2	BH-4	Footwall	18	0.050	3.0E-06	3.7E-03
1	Fault	2	BH-4	Fault	3.0	0.20	7.5E-07	2.5E-04
1	Fault	2	BH-4	Hanging wall	20	0.045	3.3E-06	3.8E-03
3	Footwall	2	BH-4	Footwall	5.0	30	4.3E-08	2.9E-05
3	Footwall	2	BH-4	Hanging wall	32	1.0	1.3E-06	8.8E-04
5	Hanging wall	2	BH-4	Fault	10	0.010	5.0E-06	2.2E-03
5	Hanging wall	2	BH-4	Hanging wall	20	0.10	5.0E-07	9.0E-04

SUMMARY, CONCLUSIONS, AND RECOMMENDATIONS

Summary

Six injection tests were conducted in the Big Hole fault to determine the flow patterns and relative permeability of the hydraulic architectural elements of the fault. The tests used inflatable packers to isolate zones within the fault for testing. The zones to be tested were determined by core logging and geophysical logging. The scale of the tests was on the order of several meters. The cross-hole packer method (Hsieh and Neuman, 1985) was used to evaluate the results. The Theis method (Theis, 1935) with correction for an unconfined aquifer (Jacob, 1944) was also used.

The inflatable packers and pressure transducers worked well. The above ground equipment did not work as well and the configuration should be modified for any future testing. The injection rate varied over two orders of magnitude, which was beyond the capability of the flow meter. As a result, the flow meter had to be removed during two tests and the flow estimated from the water being added to the supply tanks. This also required doing a series of measurements of the overflow from the constant head tank, to obtain an average value of the overflow, to be subtracted out of the total water usage.

The start of each test also presented problems with establishing the constant head. Approximately one minute was lost at the beginning of each test as water was added to fill the pipe leading from the ground surface to the injection zone. This was done with the standpipe removed, and the constant head tank and flow meter disconnected. Then both were reconnected when the water level in the pipe reached the tee connecting the pipe to the other components. Tests 3 and 6 had to be delayed due to problems with the flow meter. Since the pressure head had been established to the top of the pipe, the entire

test had to be delayed a day while the water level in the pipe subsided to the static level.

Because of the remote location, and the need to truck water in during the course of the test, it was desirable to minimize the water usage. This meant monitoring the overflow from the constant head tank and adjusting the flow both into and out of the tank manually until a stable configuration could be found.

The testing equipment was designed under the assumption that the testing would all occur under favorable temperature conditions. Testing actually continued into November, when night-time temperatures in the San Rafael Swell went below freezing. One test was ended when the supply lines all froze. Another test was run with the supply lines disconnected at night. A heater was placed in the constant head tank to prevent freezing, and heat tape applied to all piping from the constant head tank to where the supply pipe entered the borehole. A catch tank was used to capture the heated overflow water. A pump was then used to re-circulate the heated water, with additional water added to the catch tank as necessary.

The tests all reached steady-state conditions within the six days allotted in the test design parameters. Most tests reached or were near the steady-state condition after only 100 min, indicating the permeability of the fault zone was greater than anticipated in the design stage.

Three items stand out in the pressure head responses. The volume being tested is too heterogeneous to assume direct flow paths. This is most evident in the footwall (Zone 1) response to fault injection (Zone 2) and footwall injection (Zone 1) in BH-2 at the tip zone (Site 1) (Figure 12 and Figure 14). Both these response curves show a much later response time (~ 100 min) than the other curves. This may indicate a much longer

path than the direct distance between the injection and monitoring intervals. This response occurred only in BH-2, which was positioned closest to the fault tip, indicating that the nature of the response changed in a very short distance, on the order of several meters at most. Responses in BH-1 all appeared in 10 min or less.

The Big Hole fault, like many faults in high-porosity sandstone, accommodates slip with a fault core of intensely crushed rock between slip surfaces. The fault cannot be modeled as open fractures between low porosity rock. It is a mix of open fractures, closed or filled fractures, low permeability faults, and sandstone that changes permeability based on the degree of deformation (compression, grain crushing). The response may indicate a widening of the fault core (a zone of low permeability faults and deformed, low porosity, low permeability sandstone), blocking flow both normal to and within the fault plane. This indicates that slip surfaces at this location may not connect, or are filled with cement.

At the tip zone (Site 1), six response curves that showed partial matches with the Hsieh type curve showed a flattening at later times (Figures A-2 to A-5, A-7 and A-9). This behavior occurred for all three injection zones. At the wash (Site 2), this behavior occurred in three of the four responses obtained from footwall injection (Zone 1) and hanging wall injection (Zone 3) (Figures A-16, A-17 and A-19). This is consistent with a conduit being present, created by a fracture network.

The lack of consistently good fits to the Hsieh type curves indicates the volume being tested fails the first of the criteria for a homogenous, anisotropic medium. The second criterion is for the hydraulic conductivity tensor to be positive definite. Application of the Hsieh cross-hole method indicates the tensor is not positive definite.

Results for the tip zone (Site 1) give negative directional hydraulic conductivities, which is physically impossible. The results for the wash (Site 2) give imaginary values for both the storativity and the hydraulic conductivities.

The final item is the most obvious. Several tests had no response in some of the zones, indicating the fault zone was a total barrier to flow. The complexity of the fault zone is illustrated by the lack of consistency in the barrier. This is best illustrated in the response for footwall injection (Zone 1) at the wash (Site 2) (Figure 18). The fault (Zone 2) is the only zone that does not show a response, while the other zones do respond. For the hanging wall to respond there must be flow normal to the fault plane, while the lack of response in the fault zone indicates there is no flow within or parallel to the fault plane.

Interpretation using the Theis (1935) method gives an average value for transmissivity of 2.2×10^{-5} m/s^2 and a storativity of 4.8×10^{-3}. This agrees well with earlier studies (Hood and Patterson, 1984), but the values range over four and three orders of magnitude, respectively, indicating a heterogeneous volume.

Conclusions

The fault can and does act as a barrier to flow perpendicular to the fault plane, but not for all test configurations. No definite conclusion can be drawn from these tests on whether there is enhanced flow parallel to the fault plane. The Big Hole fault most closely matches the combined conduit-barrier conceptual model (Caine et al., 1996), but the heterogeneous nature of the fault means this changes over distances of as little as several meters. This may be the result of changes in the density of slip surfaces and/or the density of the deformation bands.

Numerical hydraulic conductivity values can't be established for the permeability

components based on these tests. The heterogeneity of the fault prevents successful use of the cross-hole packer method (Hsieh and Neuman, 1985) due to poor curve fits resulting in negative and imaginary values for hydraulic conductivity. Previous studies by Hsieh using this technique (Hsieh et al., 1985) were conducted in fractured granite, where presumably the hydraulic properties were spatially consistent. Faults in high-porosity sandstone, with high spatial variation in hydraulic properties, can not be evaluated using either the cross-hole packer method or standard Theis analysis.

No correlation was seen between fault displacement and the hydraulic properties of the fault. The magnitude of the response did not vary greatly from site to site and no discernable pattern appeared in the responses. The fault core thickness at the Big Hole fault is highly variable and does not correlate with the amount or number of slip surfaces (Shipton et al., in press). The lack of consistent results from the injection tests indicates a high variability in the hydraulic properties of the fault that could be a result of the variations in the thickness and nature of the fault core rather than the amount of total displacement. Since deformation band faulting is the dominant faulting style in high porosity, reservoir quality sandstones, injection testing at this intermediate scale is not an effective method in determining the hydraulic properties of faults in sandstone reservoirs. This testing may be effective for faulting in non-porous rock where the storage is in the fractures rather than the rock.

Recommendations

If further testing is done with this equipment setup, a number of modifications should be made if economically feasible. The flow meter should be eliminated. Since the flow is constant after a very short initial time interval, the flow should be calculated

from water usage. To do this, the overflow should be eliminated from the system. Instead, a float valve should be used to control the flow into the constant head tank. Measurement of the water added to the storage tanks would then provide an accurate measure of total water used. This would eliminate the need to manually balance the inflow and outflow at the beginning of each test and minimize water usage.

A valve should be added to the packer string located in the injection zone and controlled from the surface. The piping could then be filled and the constant head tank connected prior to the start of the test. The standpipe could also be eliminated since the constant head tank would give an accurate measure of the head without the flow meter in the loop.

Testing should be planned to avoid freezing conditions. Heating the water only worked because of the low volume used. Tests with greater flow would be impractical with this workaround.

The cross-hole packer method does not appear to be a viable method to evaluate the Big Hole fault at this location and scale. The fault did show faster response times than expected, and it might be possible to expand the scale of the test by increasing the distance between the injection and monitoring zones. It would be necessary to expand the spread of the packed-off intervals in the boreholes to get a large enough variation in the direction vectors. Using the packer strings as currently configured would be too close to have all the vectors identical at this scale of test.

If the goal is to create averaged values for the hydraulic properties of the fault zone as a whole, evaluating the response curve using simple Theis analysis would appear to be effective, but with the larger volume the properties of the fault would be

overwhelmed by the properties of the undeformed rock volume, giving essentially a hydraulic conductivity value for undeformed Navajo Sandstone.

Further injection testing at this site would serve no purpose. Increasing the scale of the test would test the rock, not the fault. If any additional testing is done, it should be at a different location on the fault, to determine if the results were a product of properties unique to this section of the fault.

REFERENCES

Anderson, L.J., Osborne, R.H., and Palmer, D.F., 1983, Cataclastic rocks of the San Gabriel fault-An expression of deformation at deeper crustal levels in the San Andreas fault zones: Tectonophysics, v. 98, p. 209-251.

Andersson, J.E., Ekman, L., Nordqvist, R., and Winberg, A., 1991, Hydraulic testing and modeling of a low-angle fracture zone at Finnsjon, Sweden: Journal of Hydrology, v. 126, p. 45-77.

Antonellini, M. and Aydin, A., 1994, Effect of faulting on fluid flow in porous sandstones: Petrophysical properties: AAPG Bulletin, v. 78, p. 355-377.

Antonellini, M., Aydin, A. and Orr, L., 1999, Outcrop aided characterization of a faulted hydrocarbon reservoir: Arroyo Grande oil field, California, USA, *in* Haneberg, W.C., et al., eds., Faults and subsurface fluid flow in the shallow crust: American Geophysical Union Geophysical Monograph 113, p. 7-26.

Aydin, A., 1978, Small faults formed as deformation bands in sandstone: Pure and Applied Geophysics, v. 116, p. 931-942.

Baars, D.L., and Stevinson, G.M., 1981, Tectonic evolution of the Paradox Basin, Utah and Colorado, *in* Wiegand, D.L., ed., Guidebook to the geology of the Paradox Basin: 1981 Field Conference, Rocky Mountain Association of Geologists, p. 23-31.

Barenblatt, G.I., Zheltov, Iu. P., and Kocina, I.N., 1960, Basic concepts in the theory of seepage of homogeneous liquids in fissured rocks (strata): Journal of Applied Mathematics and Mechanical Engineering English Translation, v. 24, p. 1286-1303.

Bruhn, R.L., Yonkee, W.E., and Parry, W.T., 1990, Structural and fluid-chemical properties of seismogenic normal faults: Tectonophysics, v. 175, p. 139-157.

Bruhn, R.L., Parry, W.T., Yonkee, W.A., and Thompson, T., 1994, Fracturing and hydrothermal alteration in normal fault zones: Pure and Applied Geophysics, v. 142, p. 609-644.

Byerlee, J.D., 1993, Model for episodic flow of high pressure water in fault zones before earthquakes: Geology, v. 21, p. 303-306.

Caine, J.S., Coates, D.R., Timoffeef, N.P., and Davis, W.D., 1991, Hydrogeology of the Northern Shawangunk Mountains: New York State Geological Survey Open-File Report 1g806, 72 p. and maps.

Caine, J.S., Evans, J.P., and Forster, C.B., 1996, Fault zone architecture and permeability structure: Geology, v. 24, p. 1025-1028.

Chester, F.M., Evans, J.P., and Biegel, R.L., 1993, Internal structure and weakening mechanisms of the San Andreas fault: Journal of Geophysical Research (B), Solid Earth and Planets, v. 98, p. 771-786.

Chester, F.M., and Logan, J.M., 1986, Composite planar fabric of gouge from the Punchbowl fault, California: Journal of Structural Geology, v. 9, p. 621-634.

Cinco, L.H., and Samaneigo, V., 1977, Effect of wellbore storage and damage on the transient pressure behavior of vertically fractured wells: Paper SPE 6752, Dallas, Texas, Society of Petroleum Engineers, n.p.

Cowie, P.A., and Shipton, Z.K., 1998, Fault tip displacement gradients and process zone dimensions: Journal of Structural Geology, v. 10, p. 983-997.

David, T.W., Michener, S.R., Dolan, T.J., and Cavagrotti, R.R., 1999, An integrated

approach to the characterization and remediation of gasoline in a fractured, sedimentary bedrock setting, *in* Proceedings of the 2000 Petroleum Hydrocarbons and Organic Chemicals in Ground Water; Prevention, Detection and Remediation Conference and Exposition: Westerville, OH, Ground Water Publishing Company, p. 316-330.

Davison, C.C., and Wang, C.Y., 1988, Hydrogeologic characteristics of major fracture zones in a large granitic batholith of the Canadian shield, *in* Proceedings, 4th Canadian-American Conference on Hydrogeology: Banff, Alberta, Canada, n.p.

Dershowitz, W., Wallman, P., and Kindred, S., 1991, Discrete fracture modeling for the Stripa site characterization and validation drift inflow predictions, SKE Report 91-16: Stockholm, Swedish Nuclear Power and Waste Management Company, n.p.

Forster, C.B., and Evans, J.P., 1991, Hydrogeology of thrust faults and crystalline thrush sheets: Results of combined field and modeling studies: Geophysical Research Letters, v. 18, p. 979-982.

Fossen, H., and Hesthammer, J., 2000, Possible absence of small faults in the Gulfaks field, northern North Sea: implications for downscaling of faults in some porous sandstones: Journal of Structural Geology, v. 22, p. 851-863.

Fouch, T.D., Lawton, T.F., Nichols, D.J., Cashion, W.B., and Cobban, W.A., 1983, Patterns and timing of synorogenic sedimentation in Upper Cretaceous rocks of central and northeast Utah, *in* Reynolds, M.W., ed., Mesozoic paleogeography of the west-central United States: Rocky Mountain Paleogeography Symposium, v. 2, p. 305-336.

Freeze, R.A., and Cherry, J.A., 1979, Groundwater: Englewood Cliffs, New Jersey, Prentice-Hall Inc., 604 p.

Gibson, R.G., 1994, Fault-zone seals in siliciclastic strata of the Columbus Basin, offshore Trinidad: AAPG Bulletin, v. 78, p. 1372-1385.

Gilluly, J., 1929, Geology and oil prospects of parts of the San Rafael Swell and some adjacent areas in Utah: U.S. Geological Survey Bulletin B-0806C, p. 69-130.

Goddard, J.V., and Evans, J.P., 1995, Chemical changes and fluid-rock interaction in faults of crystalline thrust sheets, northwestern Wyoming, USA: Journal of Structural Geology, v. 17, p. 533-547.

Hantush, M.S., and Thomas, R.G., 1966, A method for analyzing a drawdown test in an anisotropic aquifer: Water Resources Research, v. 2, p. 281-285.

Herbert, A., Gale, J., Lanyon, G., and MacLeod, R., 1991, Modeling for the Stripa site characterization and validation drift inflow: prediction of flow through fractured rock, SKE Report 91-35: Stockholm, Swedish Nuclear Power and Waste Management Company, n.p.

Hood, J.W., and Danielson, T.W., 1979, Aquifer tests of the Navajo Sandstone near Caineville, Utah: Salt Lake City, Utah Department of Natural Resources Technical Publication No. 66, 69 p.

Hood, J.W., and Patterson, D.J., 1984, Bedrock aquifers of the northern San Rafael Swell area, Utah, with special emphasis on the Navajo Sandstone: Salt Lake City, Utah Department of Natural Resources, Technical Publication No. 78, 128 p.

Hsieh, P.A., and Neuman, S.P., 1985, Field determination of the three-dimensional hydraulic conductivity tensor of anisotropic media: 1. Theory: Water Resources

Research, v. 21, p. 1655-1665.

Hsieh, P.A., Neuman, S.P., Stiles, G.K., and Simpson, E.S., 1985, Field determination of the three-dimensional hydraulic conductivity tensor of anisotropic media: 2. Methodology and application to fractured rocks: Water Resources Research, v. 21, p. 1667-1676.

Jacob, C.E., 1944, Notes on determining permeability by a pumping test under water-table conditions: Jamaica, New York, United States Geological Survey, 25 p.

Jakobsen, P.R., and Klint, K.E.S., 1999, Fracture distribution and occurrence of DNAPL in a clayey lodgement till: Nordic Hydrology, v. 30, p. 285-300.

Kazemi, H., 1969, Pressure transient analysis of naturally fractured reservoirs with uniform fracture distribution: Transactions of the Society of Petroleum Engineers AIME, v. 246, p. 451-462.

Krantz, R.W., 1988, Multiple fault sets and three-dimensional strain: theory and application: Journal of Structural Geology, v. 10, p. 225-237.

Lawton, T.F., 1986, Fluvial systems in the Upper Cretaceous Mesa Verde Group, and Paleocene North Horn Formation, central Utah: a record of transition from thin-skinned to thick-skinned deformation in the foreland region, *in* Peterson, J.A., ed., Paleotectonics and sedimentation in the Rocky Mountain region: AAPG Memoir 41, p. 423-442.

Magnavita, L. P., 2000, Deformation mechanisms in porous sandstones; implications for development of fault seal and migration paths in the Reconcavo Basin, Brazil, *in* Mello, M.R, et al., eds., Petroleum systems of South Atlantic margins: Tulsa, Oklahoma, American Association of Petroleum Geologists, p. 195-215.

Moench, A.F., 1984, Double-porosity models for a fissured groundwater reservoir with fracture skin: Water Resources Research, v. 20, p. 831-846.

Moore, J.C., and Vrolijk, P., 1992, Fluids in accretionary prisms: Review of Geophysics, v. 30, p. 113-135.

Moretti, I., Labaume, P., Sheppard, S., and Boulegue, J., 2000, Compartmentalization of fluid flow by thrust faults, Sub-Andean Zone, Bolivia: Journal of Geochemical Exploration, v. 69-70, p. 493-497.

National Research Council, 1996, Rock Fractures and Fluid Flow: Contemporary Understanding and Applications: Washington, D.C., National Academy Press, 551 p.

Newman, J. and Mitra, G., 1994, Fluid-influenced deformation and recrystallization of dolomite at low-temperatures along a natural fault zone, Mountain City Window, Tennessee: Geological Society of America Bulletin, v. 106, p. 1267-1280.

Neuman, S.P., Walter, G.R., Bentley, H.W., Ward, J.J., and Gonzaliz, D.D., 1984, Determination of horizontal aquifer anisotropy with three wells: Ground Water, v. 22, p. 66-72.

Papadopulos, I.S., 1965, Nonsteady flow to a well in an infinite anisotropic aquifer, *in* Hydrology of Fractured Rocks, Vol. 1, *in* Proceedings Debrovnik Symposium: Debrovnik, Yugoslavia, International Association of Scientific Hydrology, p. 21-31.

Parnell, J., 1997, Fluid migration history in the North Irish Sea-North Channel region, *in* Meadows, N.S., et al., eds., Petroleum geology of the Irish Sea and adjacent areas: London, United Kingdom, Geological Society of London, p. 213-228.

Riley, R.A., Harper, J.A., Baranoski, M.T., Laughrey, C.D., and Carlton, R.W., 1993, Measuring and predicting reservoir heterogeneity in complex depositions; the Late Cambrian Rose Run Sandstone of eastern Ohio and western Pennslyvania: Morgantown, West Virginia, Appalachian Oil and Natural Gas Research Consortium, p. 257.

Scholz, C.H., and Anders, M.H., 1994, The permeability of faults, *in* Proceedings of Workshop LXIII; U.S.G.S. Red-Book conference on the mechanical involvement of fluids in faulting: U.S. Geological Survey Open-File Report 94-228, p. 247-253.

Shipton, Z.K., 1999, Fault displacement profiles and off-fault deformation: interpreting the records of fault growth at the Chimney Rock fault array, Utah, USA [Ph.D. thesis]: Edinburgh, United Kingdom, Edinburgh University, 251 p.

Shipton, Z.K. and Cowie, P.A., 2001, Damage zone and slip-surface evolution over μm to km scales in high-porosity Navajo Sandstone, Utah: Journal of Structural Geology, v. 23, p. 1825-1844.

Shipton, Z. K., Evans, J. P., Lachmar, T. E., Thomas, K., Forster, C. B., and Snelgrove, S., 2001, The three-dimnesional structure of fault damage zone and implications for permeability: Bighole Fault Drilling Project, Final Report to Industry Consortium Members, 93 p.

Shipton, Z.K., Evans, J.P., Robeson, K., Forster, C.B., and Snelgrove, S., 2002, Structural heterogeneity and permeability in faulted eolian sandstone: Implications for subsurface modeling of faults: AAPG Bulletin, v. 86, p. 863-883.

Shipton, Z.K., Evans, J.P., and Thompson, L.B., in press, The geometry and thickness of

deformation band fault core, and its influence on the deformation band fault zone sealing characteristics, *in* Sorkhabi, R., ed., AAPG Memoir on Fault Sealing.

Sibson, R.H., 1977, Fault rocks and fault mechanisms: Journal of the Geological Society of London, v. 133, p. 191-231.

Smith, L., Forster, C.B., and Evans, J.P., 1990, Interaction of fault zones, fluid flow, and heat transfer at basin scale, *in* Hydrogeology of permeability environments: Verlag Heinz Heise, Hanover, Germany, p. 41-67.

Snow, D.T., 1969, Anisotropic permeability of a fractured media: Water Resources Research, v. 5, p. 1273-1289.

Theis, C.V., 1935, The relationship between the lowering of the piezometric surface and the rate and duration of discharge of a well using ground water storage: Transactions, American Geophysical Union, p. 518-524.

Thomas, K., Shipton, Z.K., and Evans, J.P., 2000, Stratigraphic and structural heterogeneities in faulted eolian sandstone from borehole geophysics and cores: Geological Society of America Abstracts with Programs, v. 32, p. A411.

Warren, J.E., and Root, P.J., 1963, The behavior of naturally fractured reservoirs: Transactions of the Society of Petroleum Engineering AIME, v. 228, p. 245-255.

Weiss, E., 1987, Ground-water flow in the Navajo Sandstone in parts of Emery, Grand, Carbon, Wayne, Garfield, and Kane Counties, southeast Utah: U.S. Geological Survey Water-Resources Investigations Report 86-4012, 41 p.

Willhite, S.M., Garner, E.D., and Stanley, C.C., 1986, Role of geologic characterization in determining migration of hydrocarbon spills: a case study, *in* Proceedings of the NWMA/API Conference on Petroleum Hydrocarbons and Organic Chemicals

in Groundwater: Prevention, Detection and Restoration: Dublin, Ohio, National Water Well Association, p. 343-356.

Witkind, I. J., 1991, Implications of distinctive fault sets in the San Rafael Swell and adjacent areas, east-central Utah, *in* Chidsey, T.C. Jr., ed., Geology of East-Central Utah: Salt Lake City, Utah Geological Association Guidebook no. 19, p. 141-148.

APPENDICES

Appendix A. Hsieh Type Curve Matches

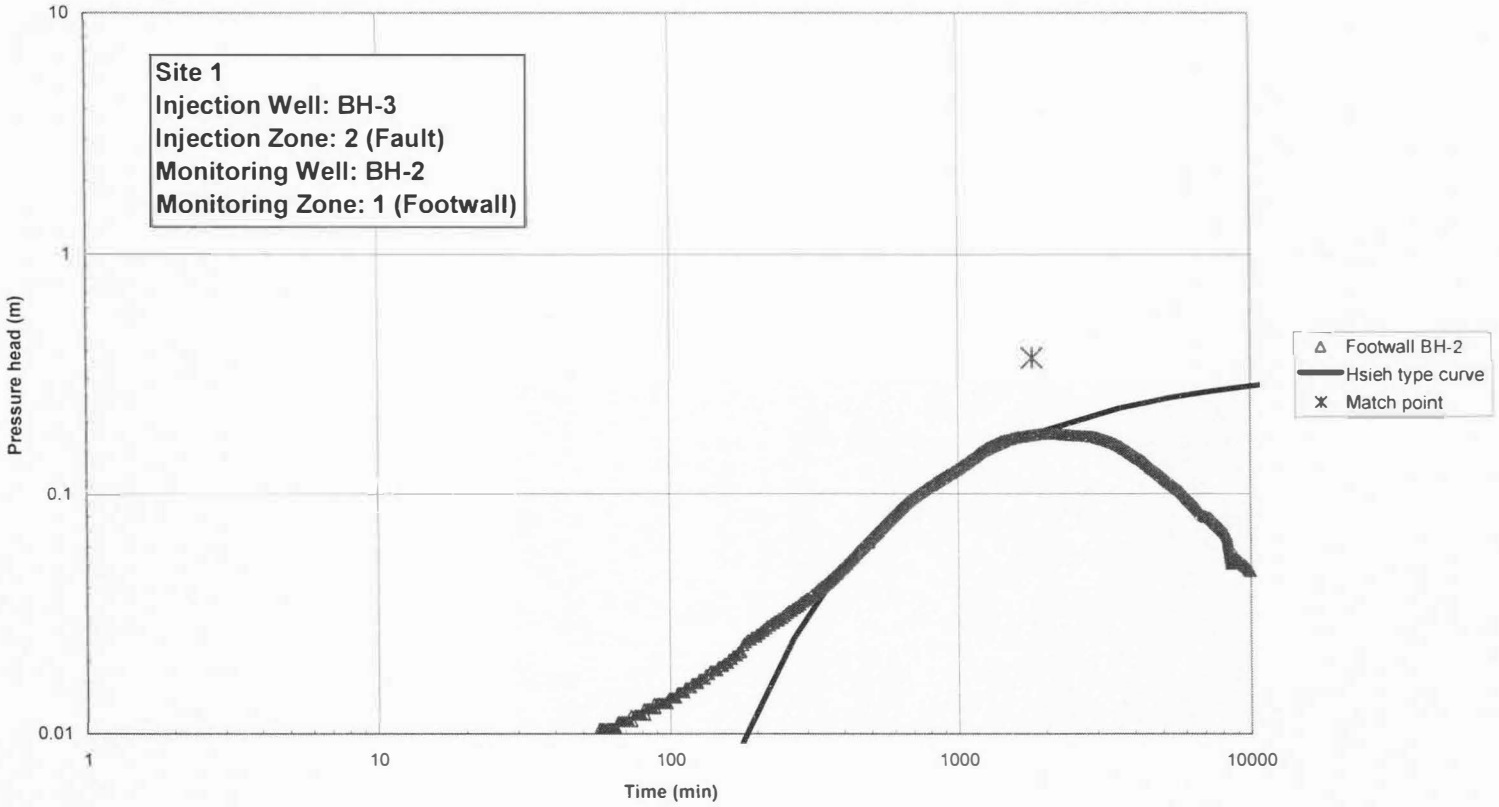

Figure A-1 Test 2 footwall pressure head response for fault injection (Zone 2) at tip zone (Site 1) monitored in BH-2 with Hsieh type curve.

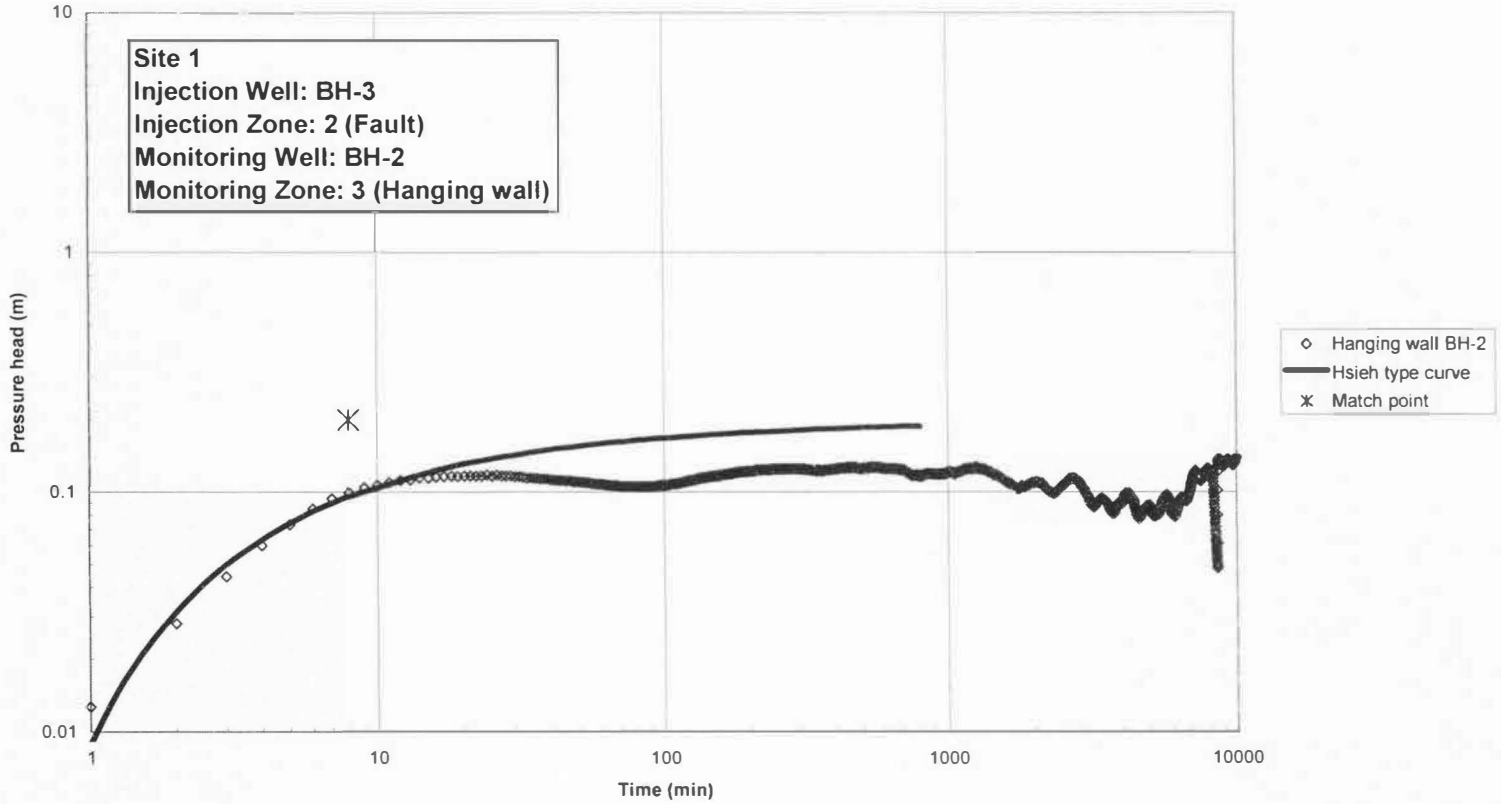

Figure A-2 Test 2 hanging wall pressure head response for fault injection (Zone 2) at tip zone (Site 1) monitored in BH-2 with Hsieh type curve.

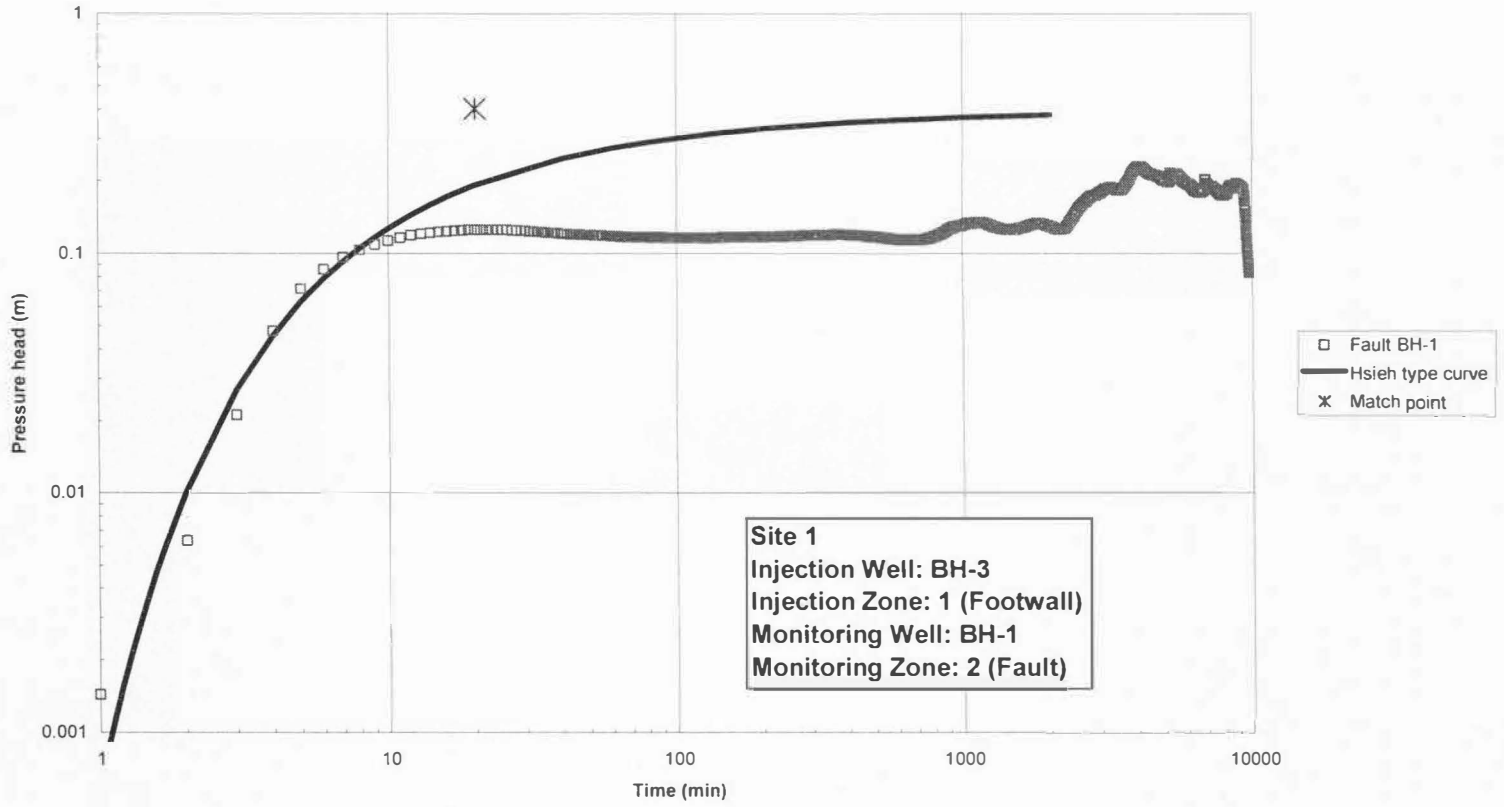

Figure A-3 Test 4 fault pressure head response for footwall injection (Zone 1) at tip zone (Site 1) monitored in BH-1 with Hsieh type curve.

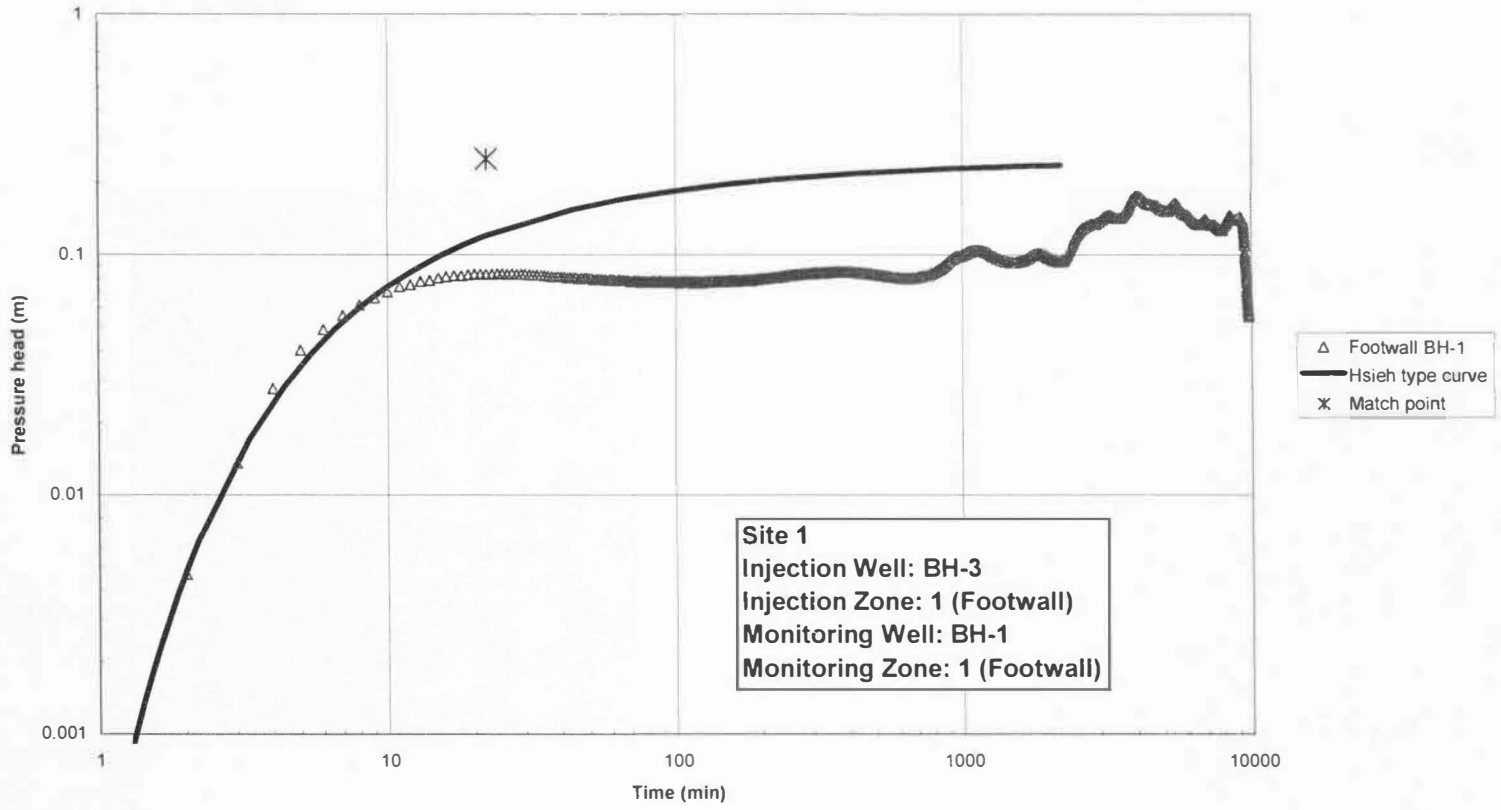

Figure A-4 Test 4 footwall pressure head response for footwall injection (Zone 1) at fault tip (Site 1) monitored in BH-1 with Hsieh type curve.

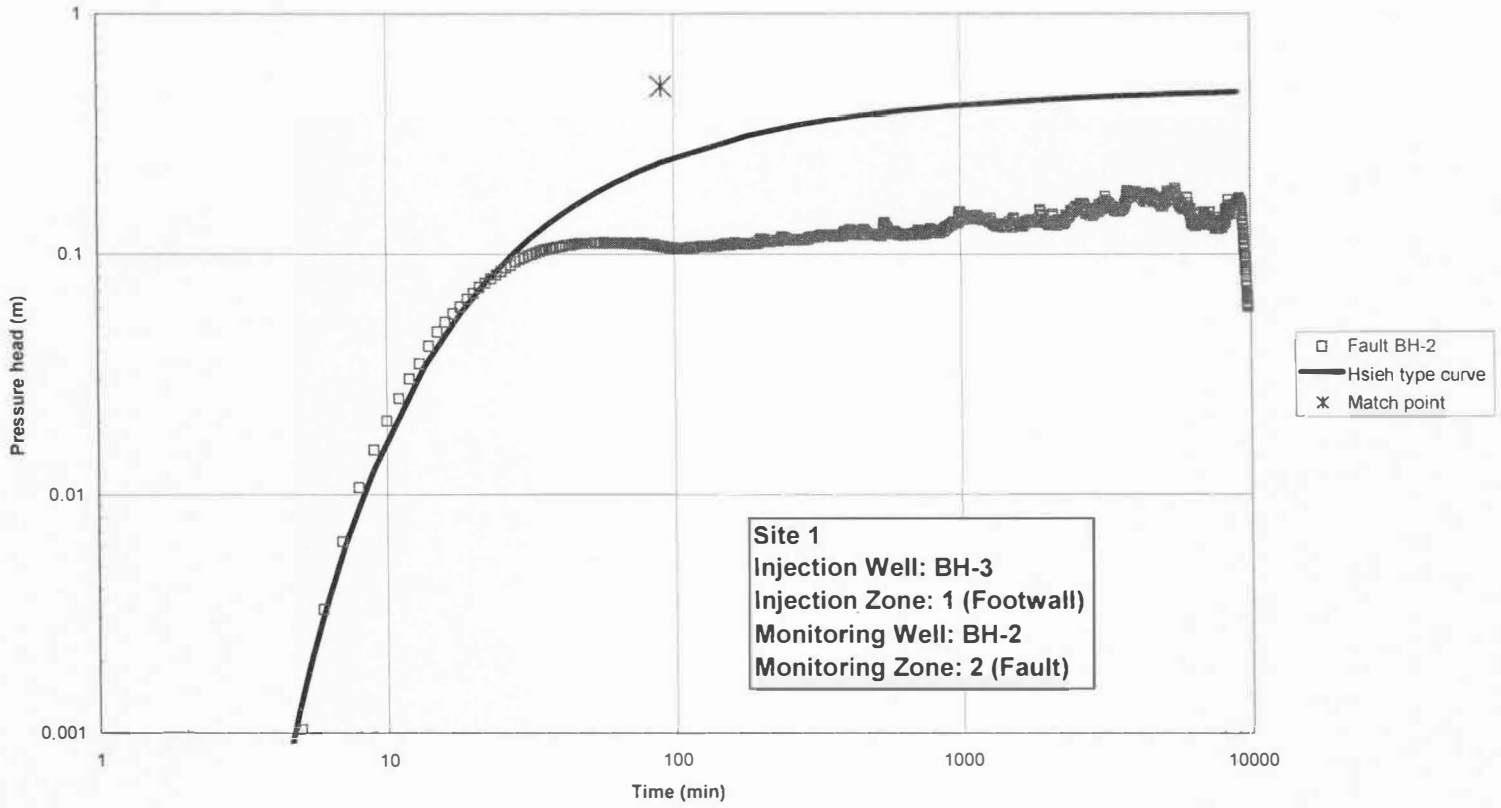

Figure A-5 Test 4 fault pressure head response for footwall injection (Zone 1) at fault tip (Site 1) monitored in BH-2 with Hsieh type curve.

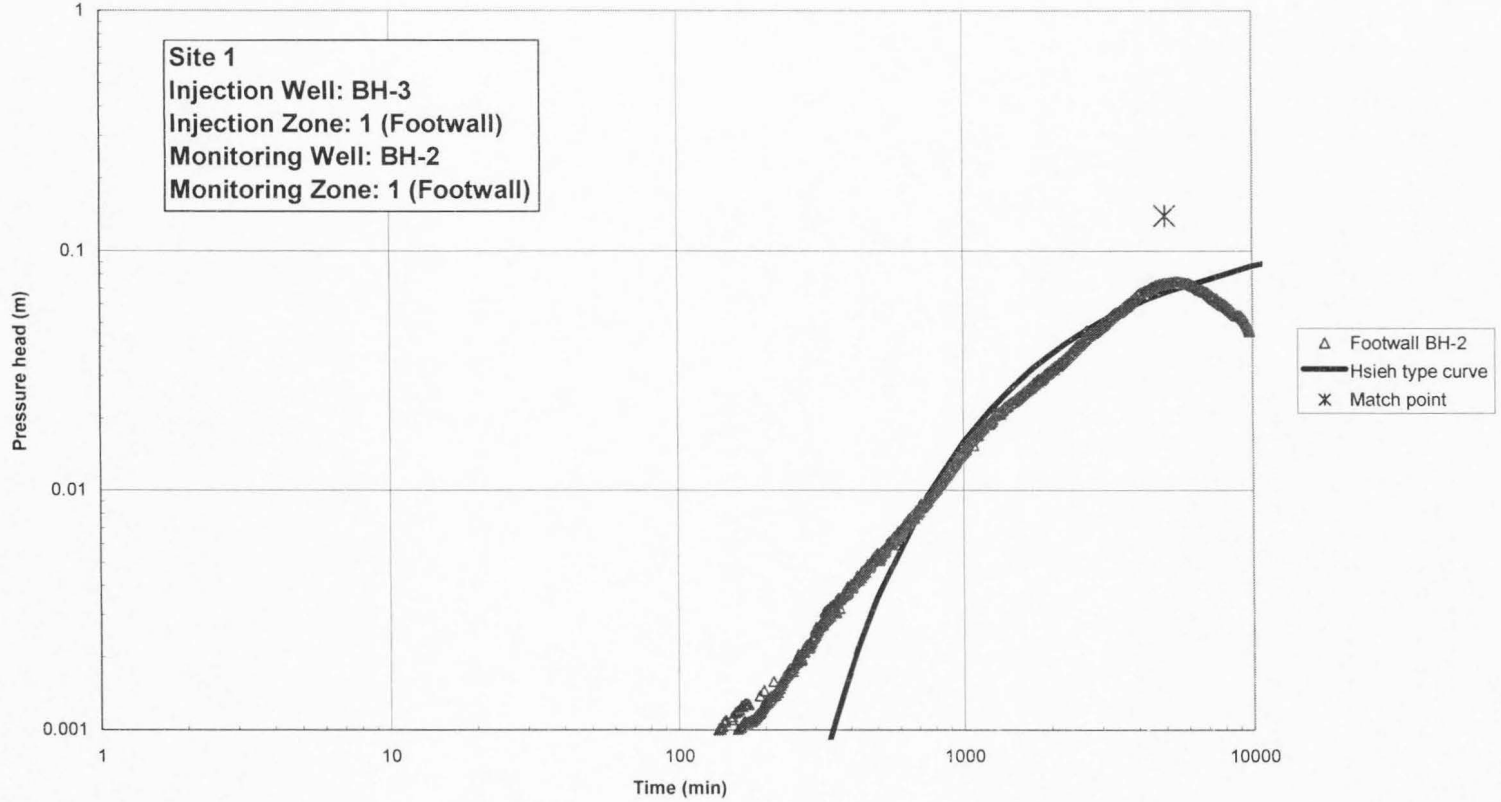

Figure A-6 Test 4 footwall pressure head response for footwall injection (Zone 1) at fault tip (Site 1) monitored in BH-2 with Hsieh type curve.

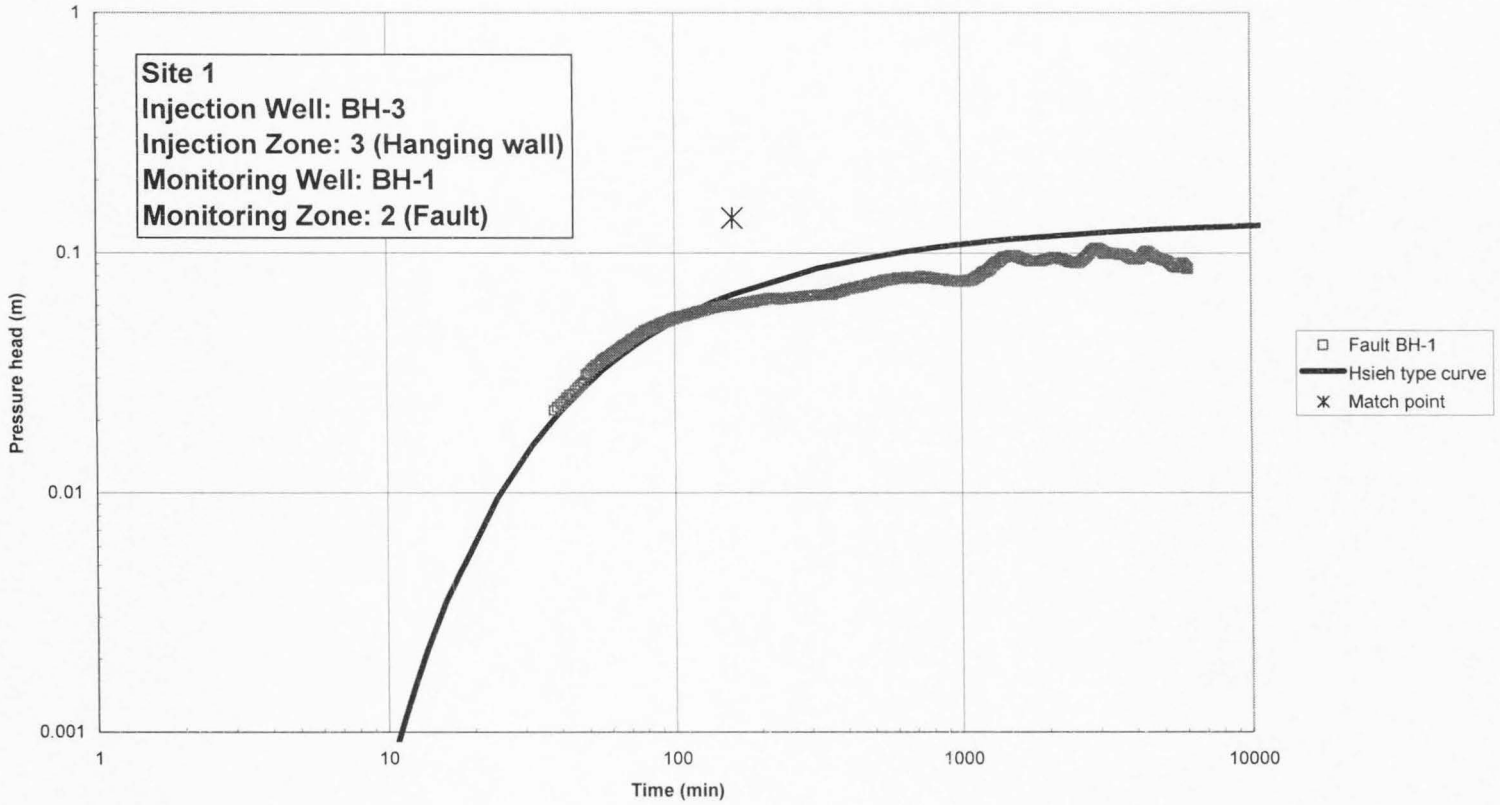

Figure A-7 Test 6 fault pressure head response for hanging wall injection (Zone 3) at fault tip (Site 1) monitored in BH-1 with Hsieh type curve.

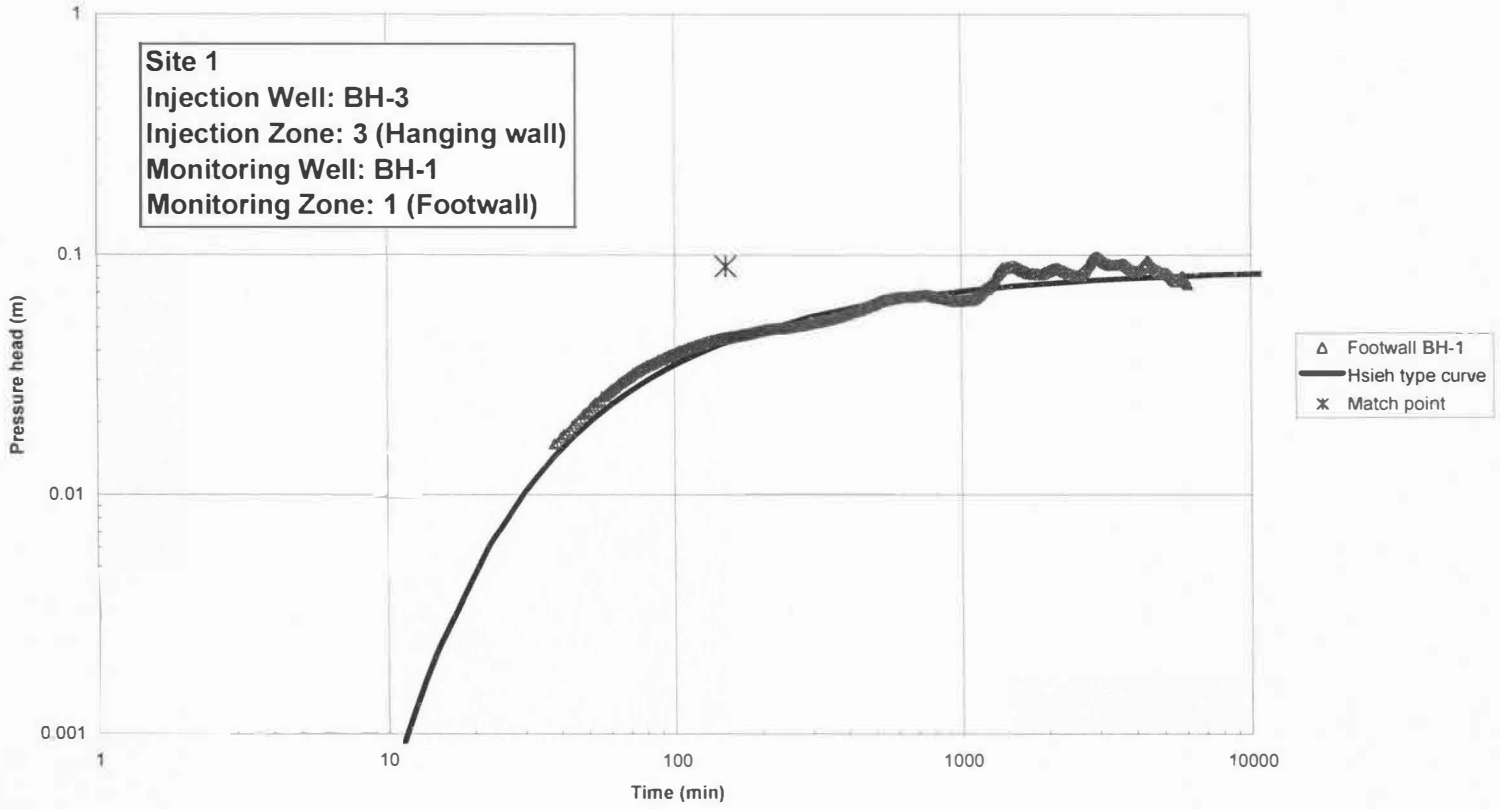

Figure A-8 Test 6 footwall pressure head response for hanging wall injection (Zone 3) at fault tip (Site 1) monitored in BH-1 with Hsieh type curve.

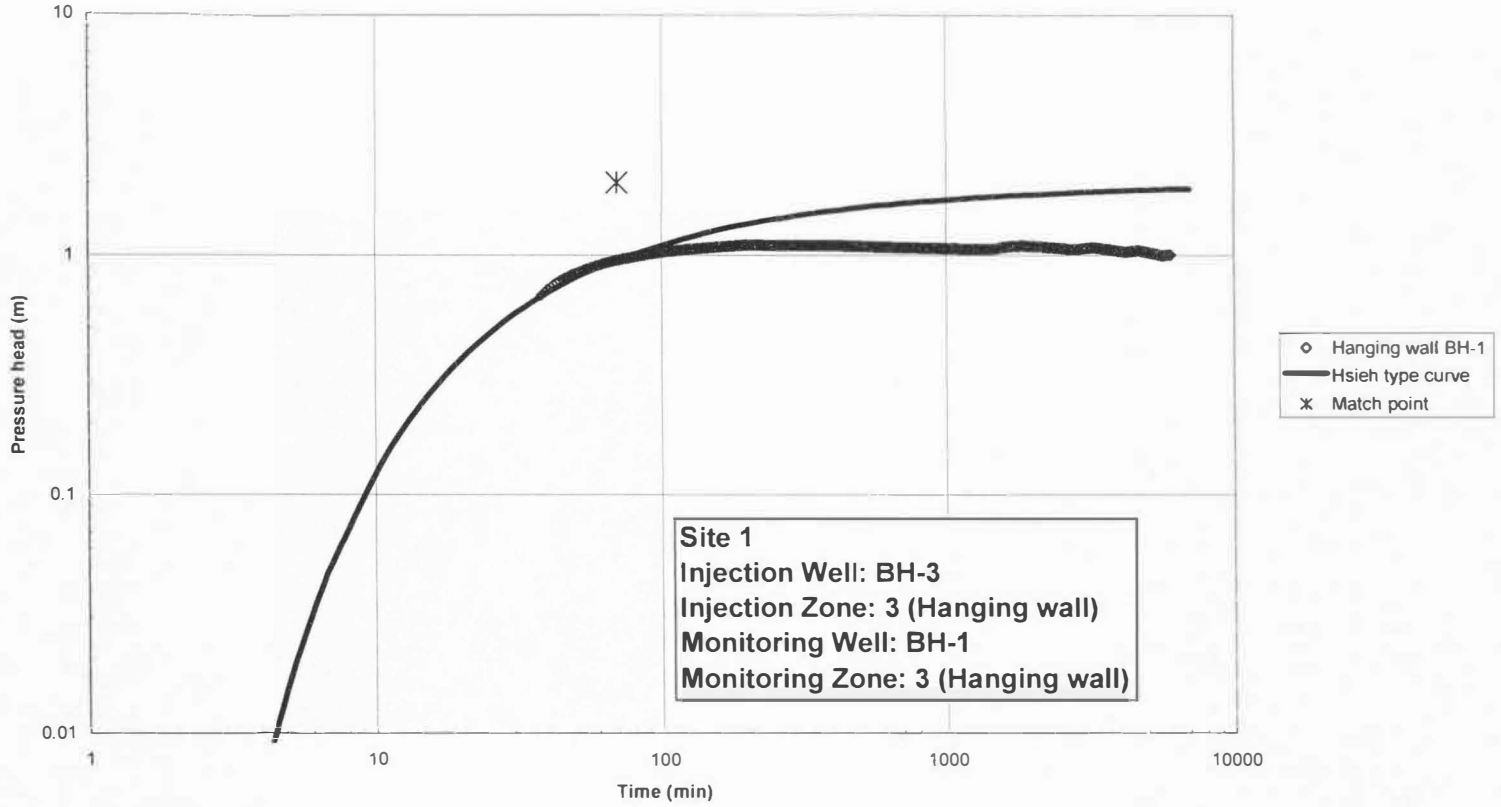

Figure A-9 Test 6 hanging wall pressure head response for hanging wall injection (Zone 3) at fault tip (Site 1) monitored in BH-1 with Hsieh type curve.

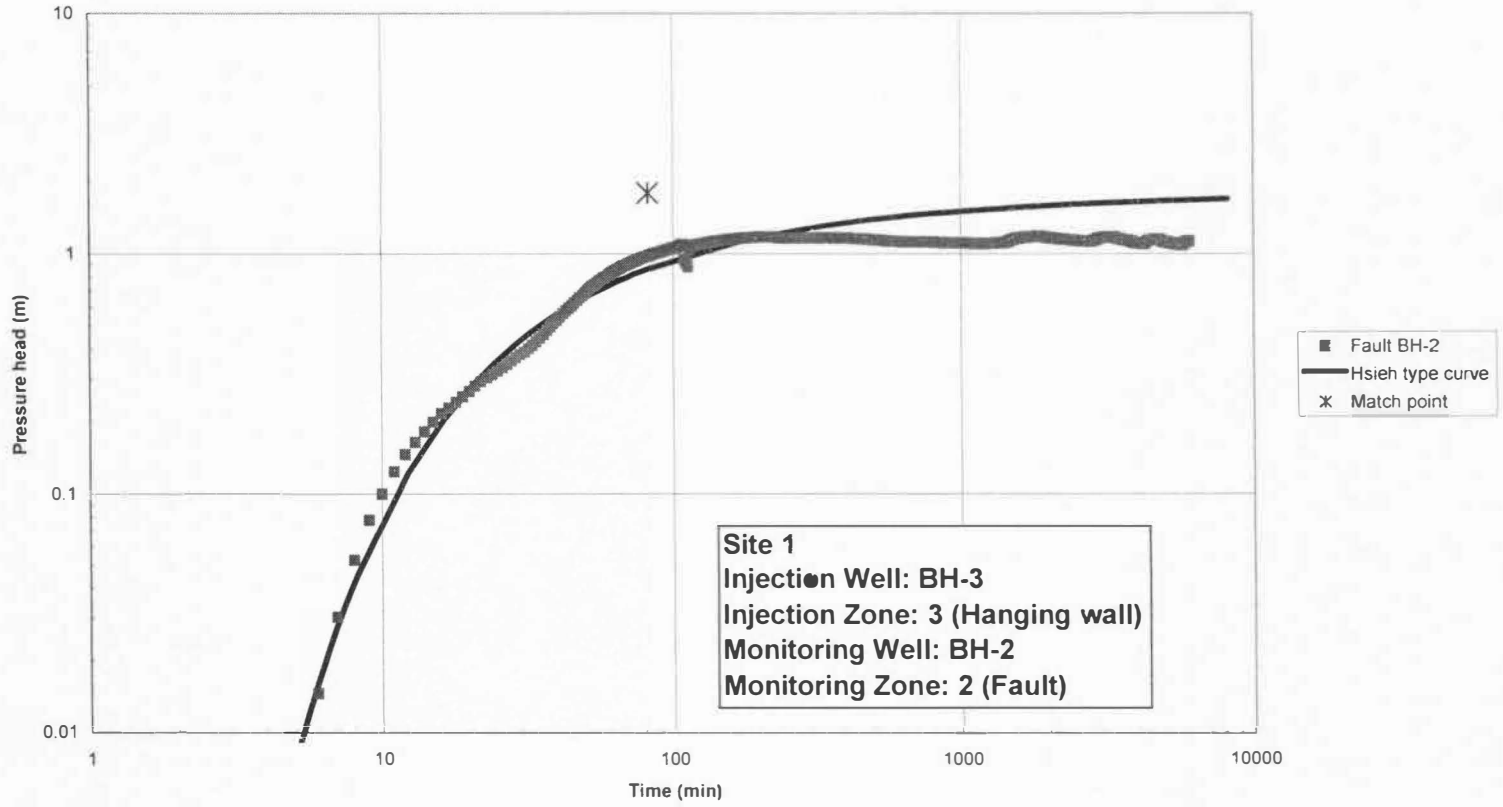

Figure A-10 Test 6 fault pressure head response for hanging wall injection (Zone 3) at fault tip (Site 1) monitored in BH-2 with Hsieh type curve.

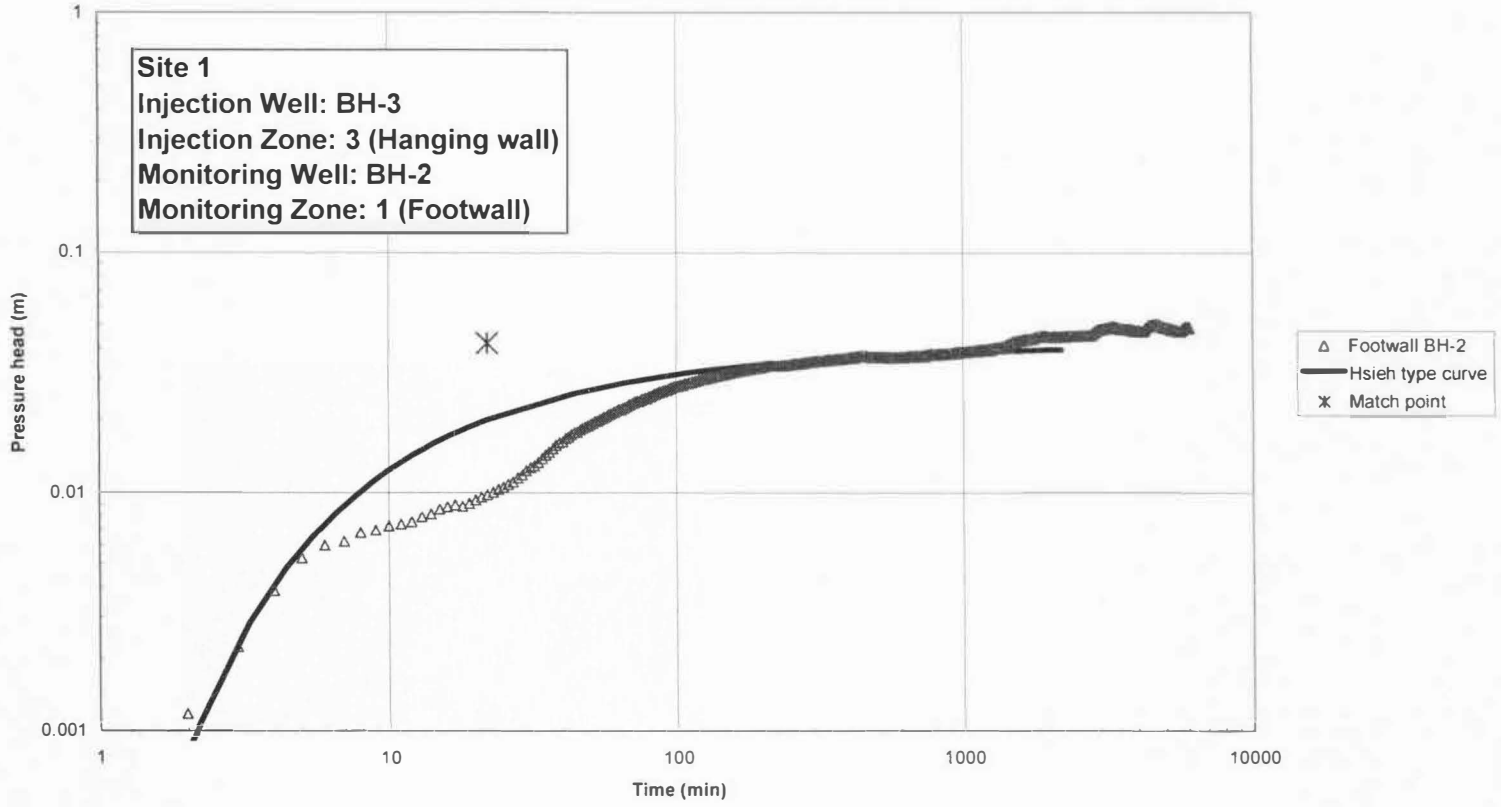

Figure A-11 Test 6 footwall pressure head response for hanging wall injection (Zone 3) at fault tip (Site 1) monitored in BH-2 with Hsieh type curve.

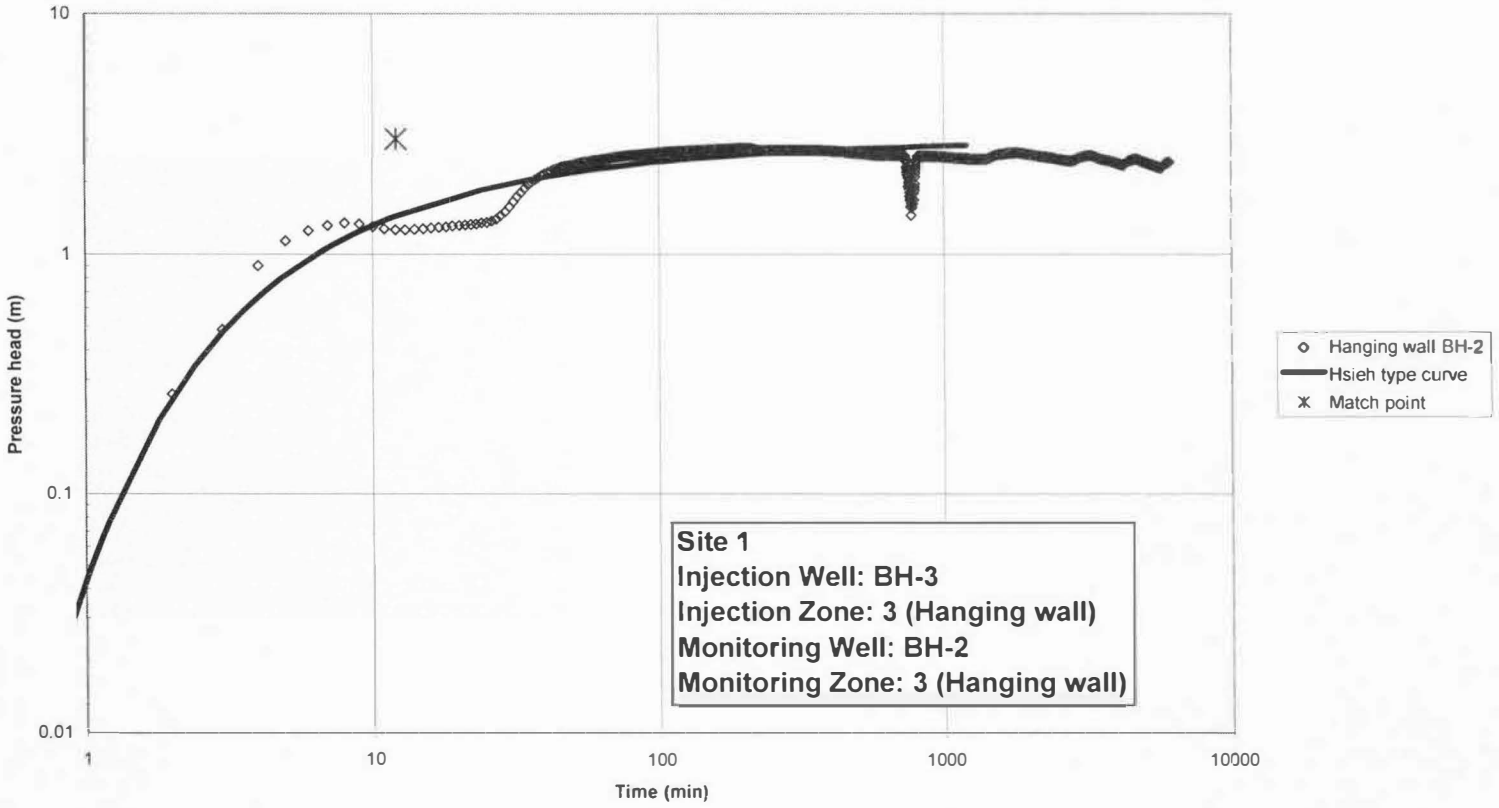

Figure A-12 Test 6 hanging wall pressure head response for hanging wall injection (Zone 3) at fault tip (Site 1) monitored in BH-2 with Hsieh type curve.

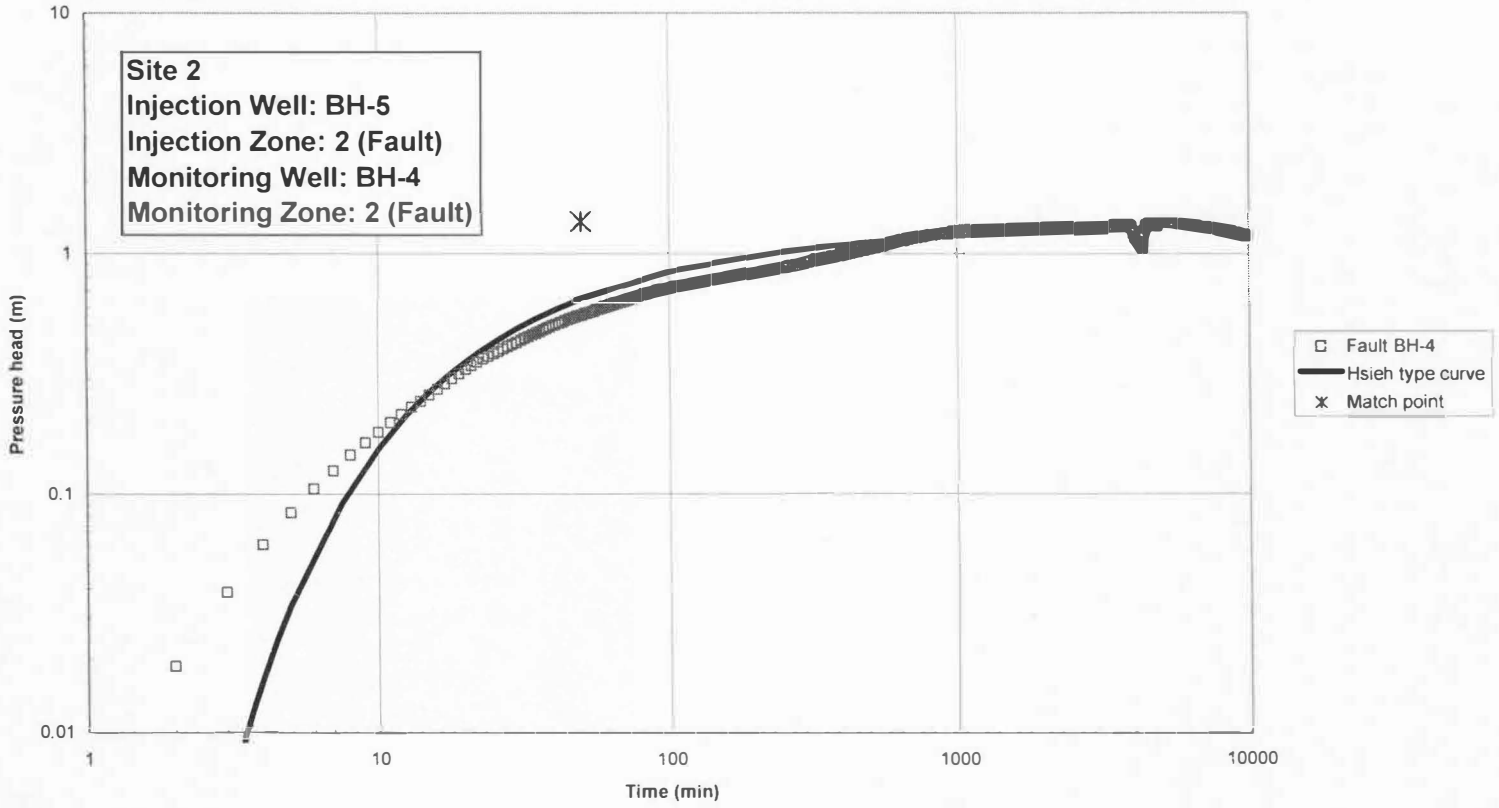

Figure A-13 Test 1 fault pressure head response for fault injection (Zone 2) at wash (Site 2) monitored in BH-4 with Hsieh type curve.

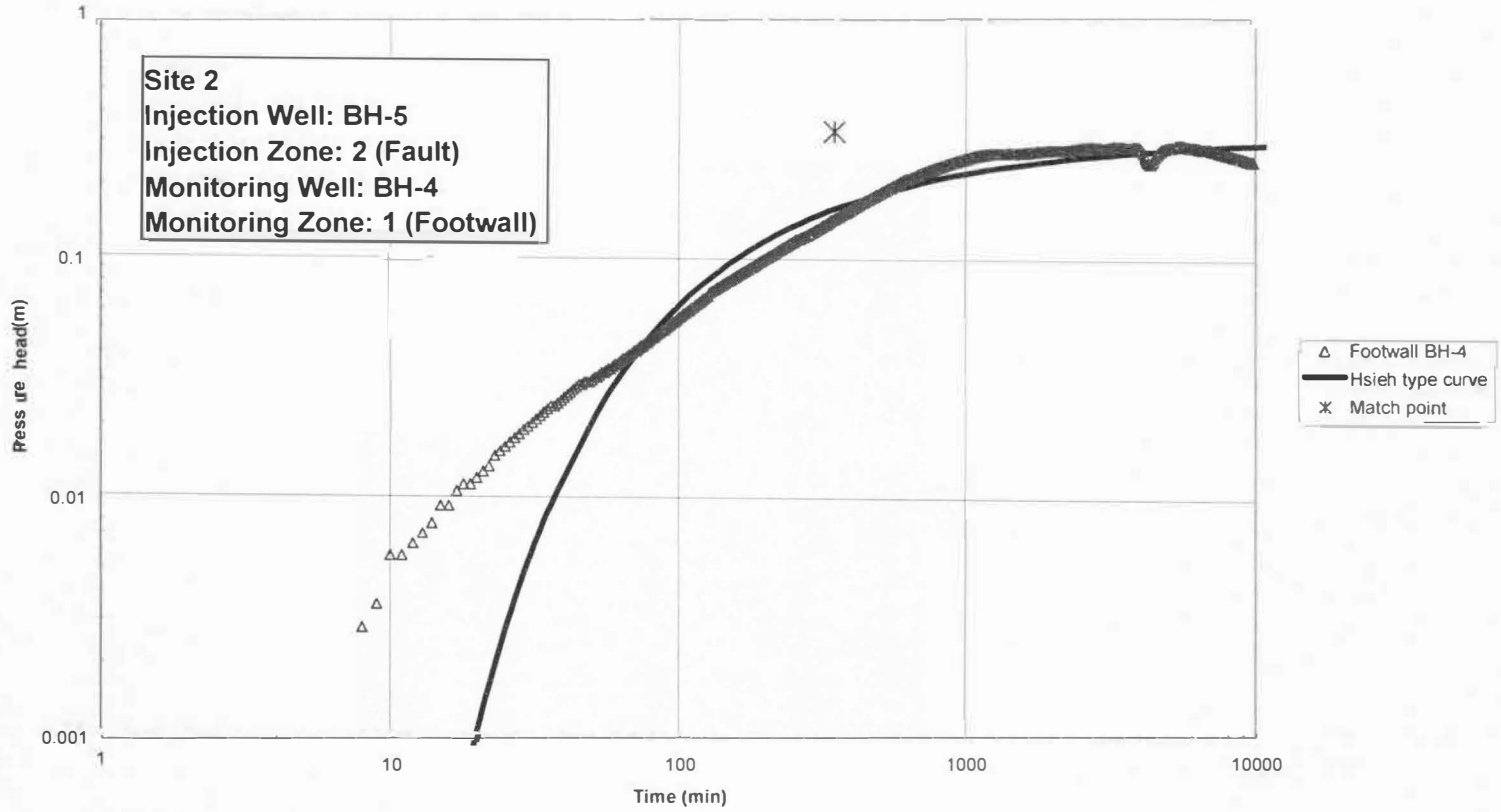

Figure A-14 Test 1 footwall pressure head response for fault injection (Zone 2) at wash (Site 2) monitored in BH-4 with Hsieh type curve.

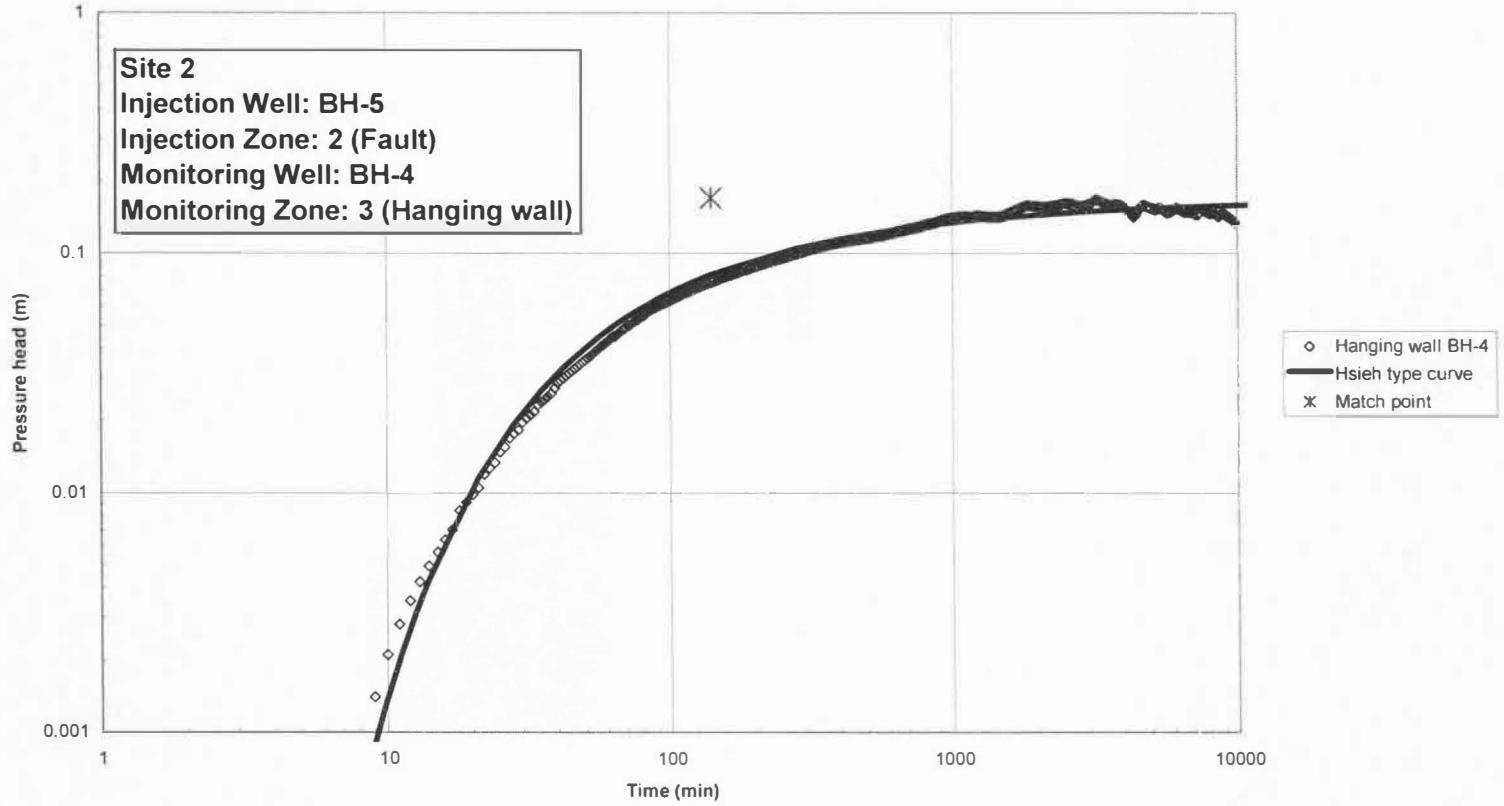

Figure A-15 Test 1 hanging wall pressure head response for fault injection (Zone 2) at wash (Site 2) monitored in BH-4 with Hsieh type curve.

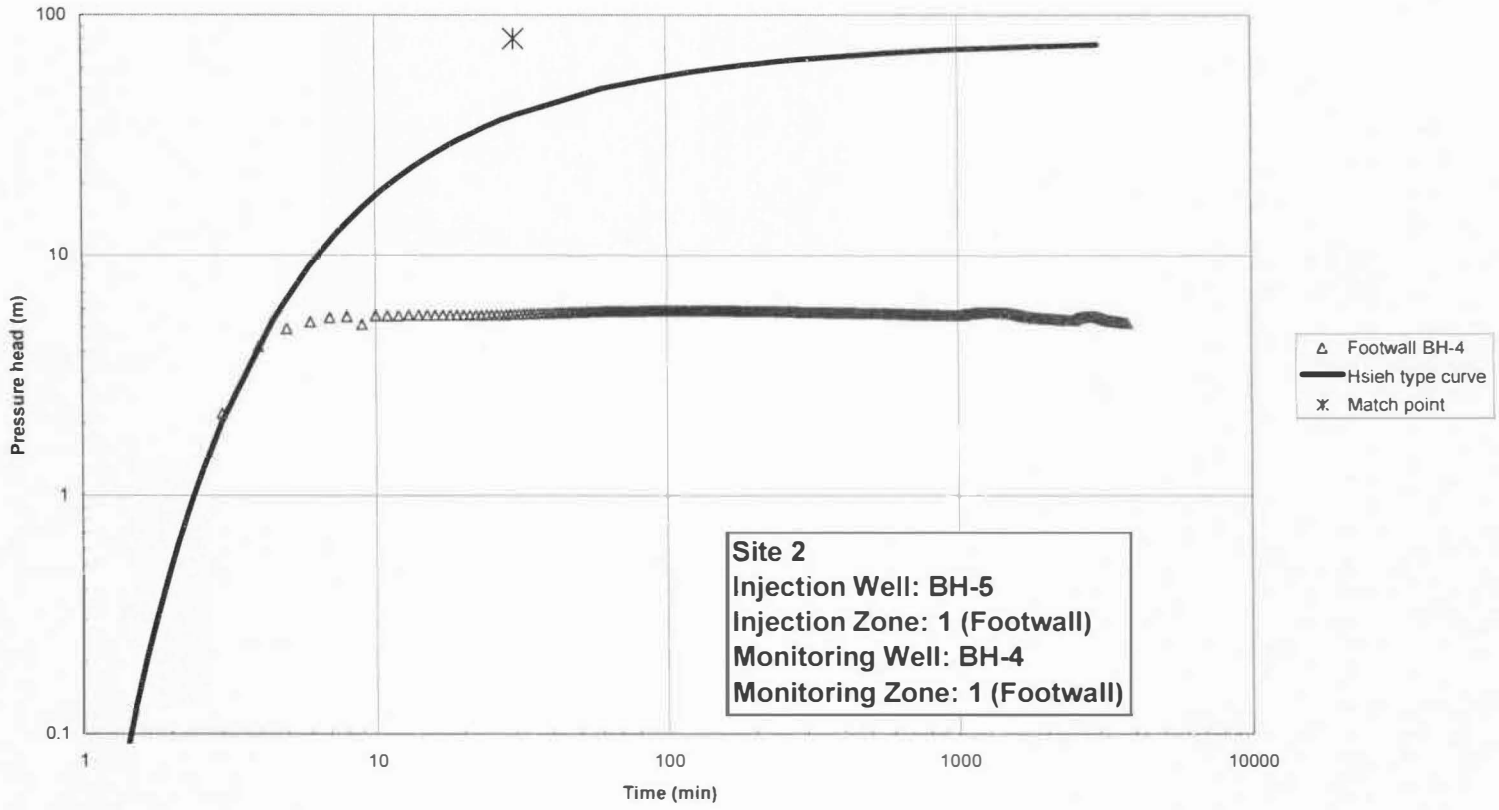

Figure A-16 Test 3 footwall pressure head response for footwall injection (Zone 1) at wash (Site 2) monitored in BH-4 with Hsieh type curve.

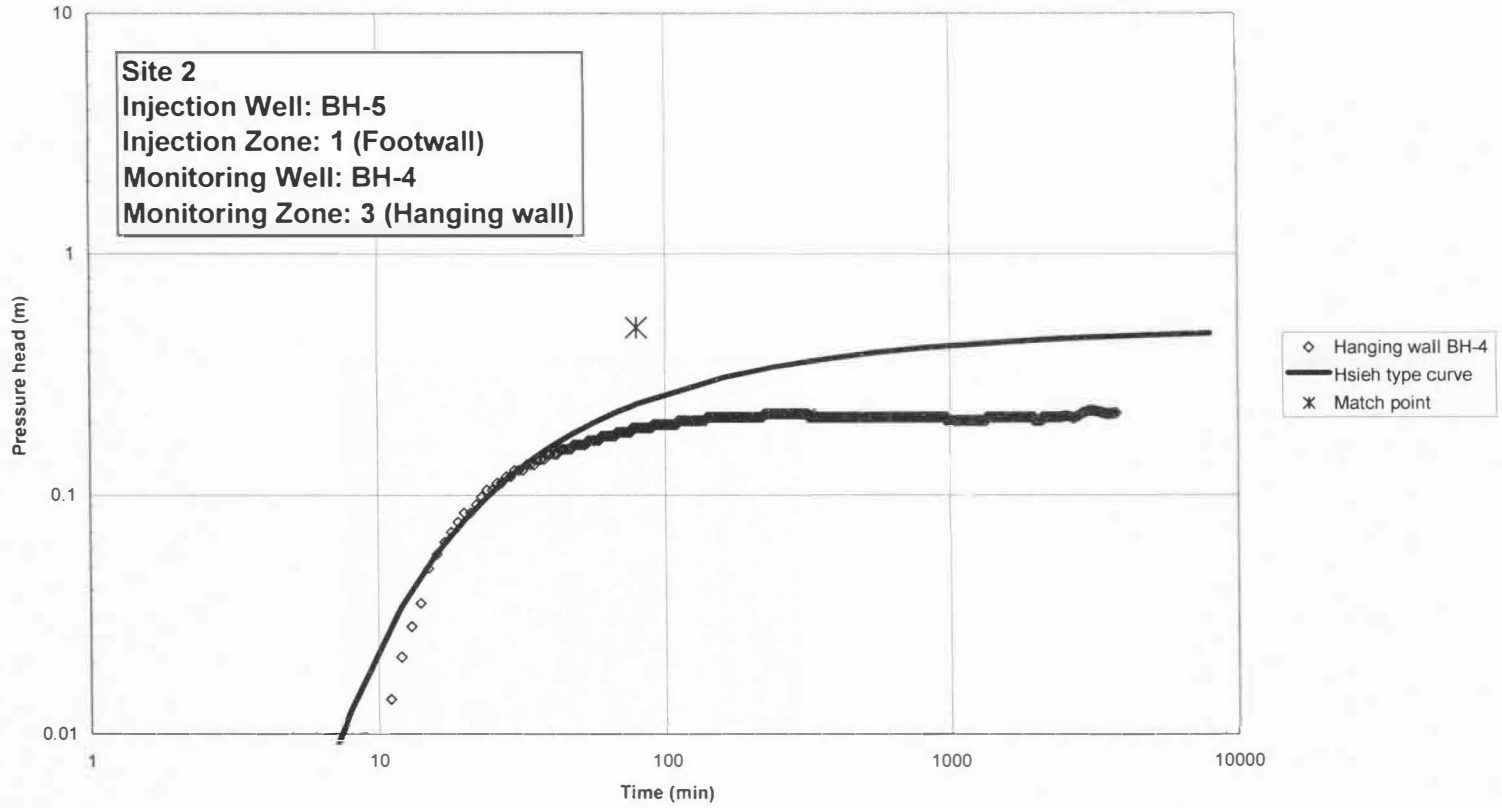

Figure A-17 Test 3 hanging wall pressure head response for footwall injection (Zone 1) at wash (Site 2) monitored in BH-4 with Hsieh type curve.

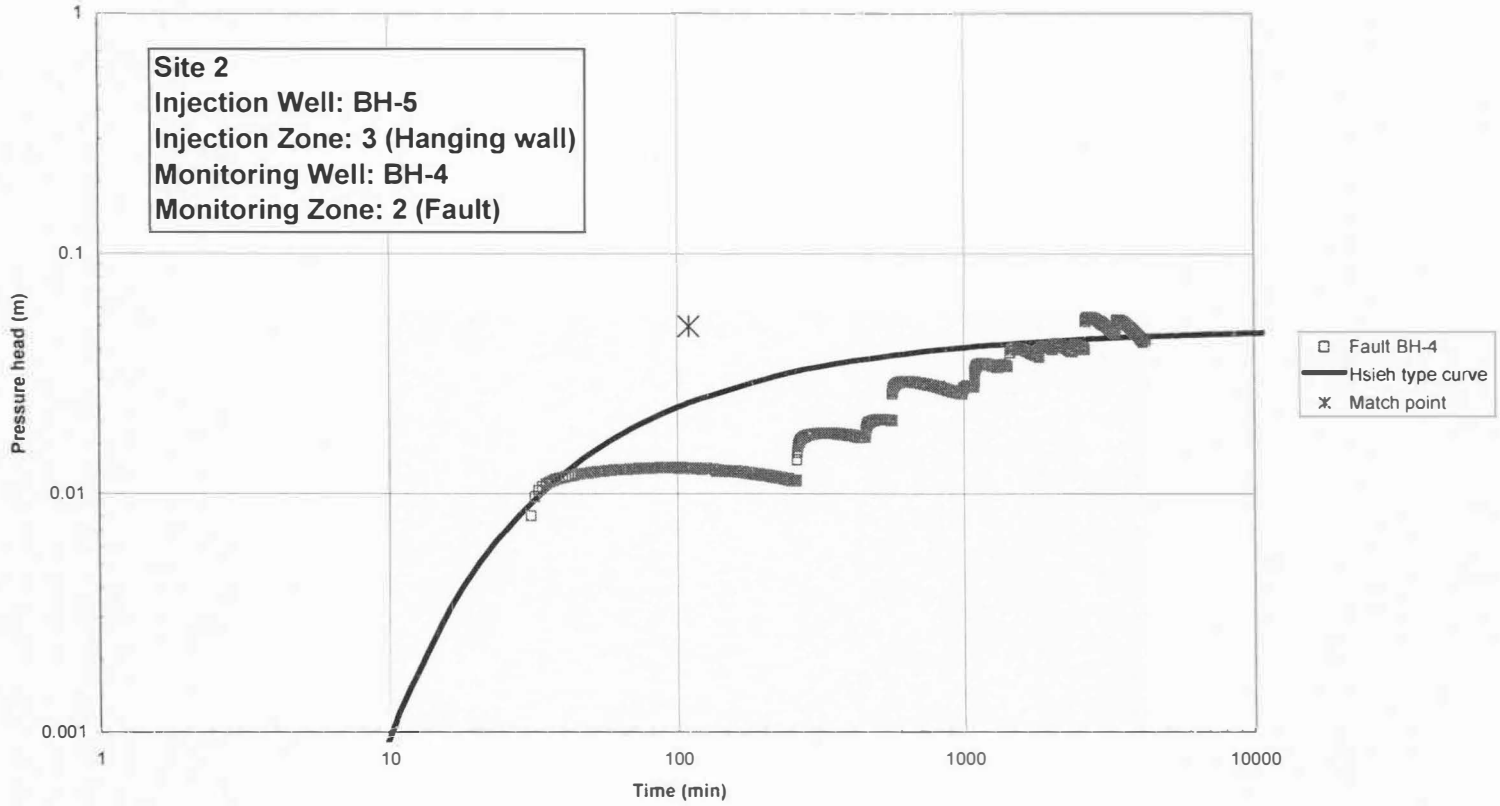

Figure A-18 Test 5 fault pressure head response for hanging wall injection (Zone 3) at wash (Site 2) monitored in BH-4 with Hsieh type curve.

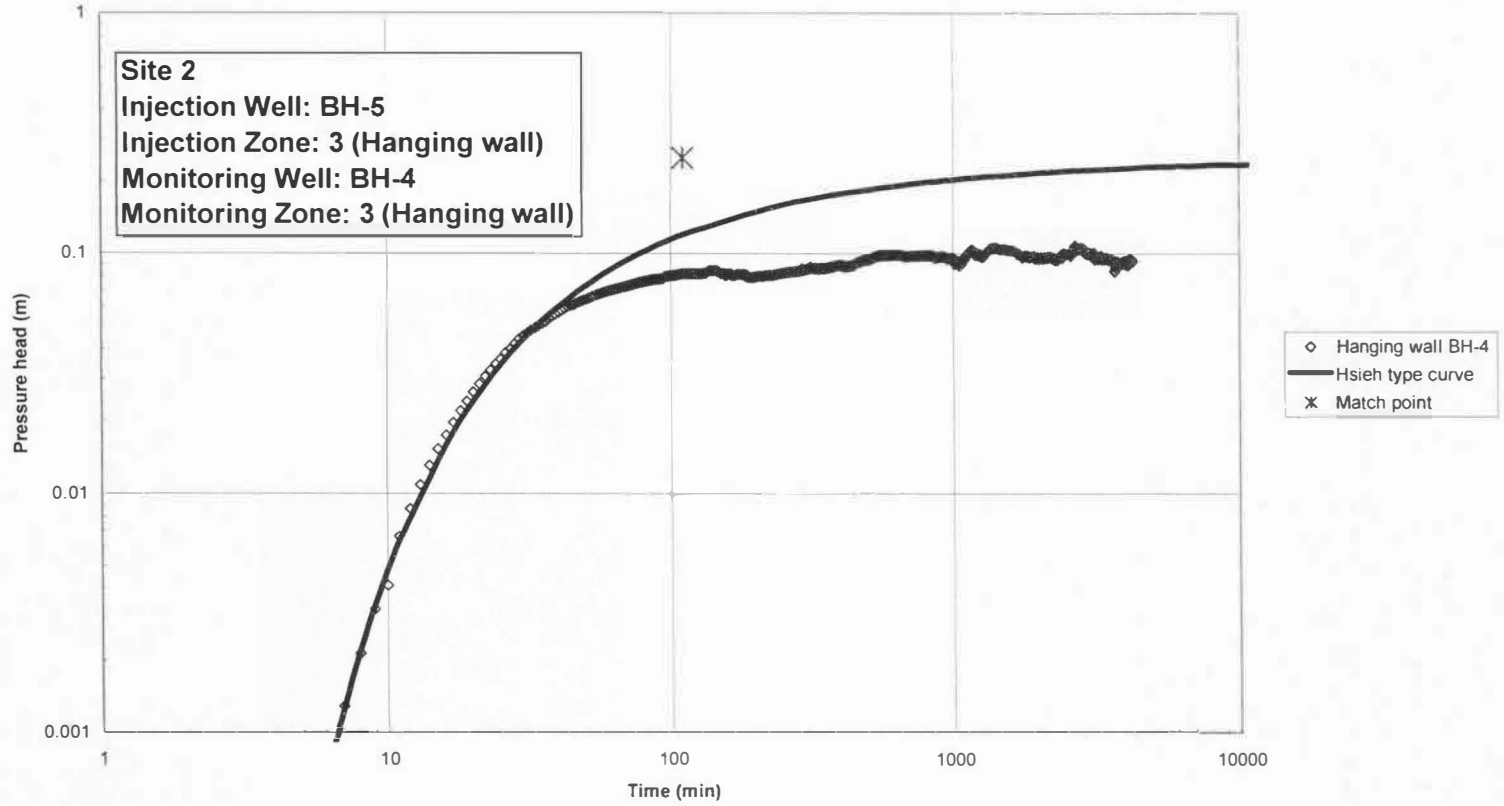

Figure A-19 Test 5 hanging wall pressure head response for hanging wall injection (Zone 3) at wash (Site 2) monitored in BH-4 with Hsieh type curve.

Appendix B. Table of Values to Compute Hsieh Solution for Hydraulic Conductivity (K)

TABLE B-1 VALUES TO COMPUTE HSIEH SOLUTION FOR K

Injection Well/Zone	Monitoring Well/Zone	Separation (m)	Q (m^3/s)	h* (m)	t* (min)	D/K	K/S	D/S
Site 1								
BH-3/2	BH-2/1	3.00	1.58E-06	0.37	1800	1.27342E-14	0.005006	6.37478E-17
BH-3/2	BH-2/3	3.99	1.58E-06	0.20	8	2.46813E-14	1.98895	4.90898E-14
BH-3/1	BH-1/1	6.57	1.26E-06	0.25	22	3.72346E-15	1.963683	7.31171E-15
BH-3/1	BH-1/2	6.74	1.26E-06	0.40	20	1.38345E-15	2.270952	3.14175E-15
BH-3/1	BH-2/1	2.89	1.26E-06	0.14	5000	6.15646E-14	0.001666	1.02588E-16
BH-3/1	BH-2/2	3.80	1.26E-06	0.50	90	2.79038E-15	0.160131	4.46826E-16
BH-3/3	BH-1/1	7.89	2.61E-05	0.09	150	8.53905E-12	0.415154	3.54502E-12
BH-3/3	BH-1/2	7.50	2.61E-05	0.14	160	3.91092E-12	0.351188	1.37347E-12
BH-3/3	BH-1/3	7.24	2.61E-05	2.00	70	2.05597E-14	0.748205	1.53829E-14
BH-3/3	BH-2/1	3.81	2.61E-05	0.04	22	1.68288E-10	0.659509	1.10988E-10
BH-3/3	BH-2/2	2.83	2.61E-05	1.80	82	1.65599E-13	0.097899	1.62120E-14
BH-3/3	BH-2/3	3.06	2.61E-05	3.00	12	5.10860E-14	0.780674	3.98815E-14
Site 2								
BH-5/2	BH-4/1	1.88	1.89E-06	0.34	350	5.55390E-14	0.010067	5.59085E-16
BH-5/2	BH-4/2	1.48	1.89E-06	1.35	50	5.70135E-15	0.04354	2.48237E-16
BH-5/2	BH-4/3	2.06	1.89E-06	0.17	140	1.83808E-13	0.030417	5.59085E-15
BH-5/1	BH-4/1	1.34	1.63E-05	80.	30	1.47180E-16	0.059686	8.78455E-18
BH-5/1	BH-4/3	3.36	1.63E-05	0.50	80	5.96761E-13	0.141316	8.43316E-14
BH-5/3	BH-4/2	2.35	6.30E-07	0.05	110	1.82135E-13	0.050181	9.13963E-15
BH-5/3	BH-4/3	1.63	6.30E-07	0.25	110	1.50727E-14	0.024255	3.65585E-16

Note: matching done at $t_d = 1$, $h_{pd} = 1$

Appendix C. Mathcad Worksheet Calculating Hydraulic Conductivity Values According to the Hsieh Cross-Hole Method

Equation for the inverse diffusivity tensor:
$U = S_s K^{-1} = e_{j,1}^{\ 2} U_{11} + e_{j,2}^{\ 2} U_{22} + e_{j,3}^{\ 2} U_{33} + 2e_{j,1}e_{j,2} U_{12} + 2e_{j,2}e_{j,3} U_{23} + 2e_{j,1}e_{j,3} U_{13}$
$e_{j,i}$ = unit vector component pointing from injection point to monitoring point
i = component direction (1=east, 2=north, 3=vertical)
j = test number
X = jX6 matrix of coefficients identical to those in equation defining inverse diffusivity tensor
y = vector containing S_s/K_d (e_j) values obtained from testing
u = vector representing six unknown terms in U
uols = vector u solved by ordinary least squares

$$e := \begin{pmatrix} 0.926713901 & 0.132919591 & -0.351473653 \\ 0.696462977 & 0.100033996 & 0.71058604 \\ 0.147984753 & 0.955619551 & -0.254738662 \\ 0.058264638 & 0.99717604 & -0.047383297 \\ 0.975755803 & 0.145621913 & 0.163385653 \\ 0.740976886 & 0.110722228 & 0.662339674 \\ 0.115519139 & 0.790248525 & -0.601799466 \\ 0.04423687 & 0.890527143 & -0.452774234 \\ -0.033632663 & 0.95889936 & -0.281746093 \\ 0.723380239 & 0.098553612 & -0.683379994 \\ 0.132494677 & 0.132494677 & -0.197730939 \\ 0.899047952 & 0.122659877 & 0.420318136 \end{pmatrix} \qquad j := 1..12$$

$X_{j,1} := (e_{j,1})^2$ $\qquad X_{j,4} := 2e_{j,1} \cdot e_{j,2}$ $\qquad$ Calculate constants for X

$X_{j,2} := (e_{j,2})^2$ $\qquad X_{j,5} := 2e_{j,2} \cdot e_{j,3}$

$X_{j,3} := (e_{j,3})^2$ $\qquad X_{j,6} := 2e_{j,1} \cdot e_{j,3}$

Figure C-1 Least squares solution for directional hydraulic conductivity, tip zone (Site 1).

$$X = \begin{pmatrix} 0.859 & 0.018 & 0.124 & 0.246 & -0.093 & -0.651 \\ 0.485 & 0.01 & 0.505 & 0.139 & 0.142 & 0.99 \\ 0.022 & 0.913 & 0.065 & 0.283 & -0.487 & -0.075 \\ 0.003 & 0.994 & 0.002 & 0.116 & -0.094 & -0.006 \\ 0.952 & 0.021 & 0.027 & 0.284 & 0.048 & 0.319 \\ 0.549 & 0.012 & 0.439 & 0.164 & 0.147 & 0.982 \\ 0.013 & 0.624 & 0.362 & 0.183 & -0.951 & -0.139 \\ 0.002 & 0.793 & 0.205 & 0.079 & -0.806 & -0.04 \\ 0.001 & 0.919 & 0.079 & -0.065 & -0.54 & 0.019 \\ 0.523 & 0.01 & 0.467 & 0.143 & -0.135 & -0.989 \\ 0.018 & 0.018 & 0.039 & 0.035 & -0.052 & -0.052 \\ 0.808 & 0.015 & 0.177 & 0.221 & 0.103 & 0.756 \end{pmatrix} \quad y := \begin{pmatrix} 199.758242 \\ 0.502777787 \\ 0.509247097 \\ 0.440343952 \\ 600.116824 \\ 6.244885433 \\ 2.408743278 \\ 2.847473664 \\ 1.336532098 \\ 1.516279407 \\ 10.21461914 \\ 1.280944835 \end{pmatrix}$$

$$uols := \left(X^T \cdot X\right)^{-1} \cdot X^T \cdot y \qquad uols = \begin{pmatrix} 3.671 \times 10^2 \\ -5.535 \times 10^1 \\ -4.888 \times 10^2 \\ 1.192 \times 10^2 \\ -1.759 \times 10^2 \\ 2.061 \times 10^1 \end{pmatrix}$$

$$U := \begin{pmatrix} uols_1 & uols_4 & uols_6 \\ uols_4 & uols_2 & uols_5 \\ uols_6 & uols_5 & uols_3 \end{pmatrix} \qquad U = \begin{pmatrix} 367.126 & 119.17 & 20.611 \\ 119.17 & -55.346 & -175.932 \\ 20.611 & -175.932 & -488.816 \end{pmatrix}$$

$$SsK := U^{-1} \qquad SsK = \begin{pmatrix} -8.346 \times 10^{-4} & 0.012 & -4.245 \times 10^{-3} \\ 0.012 & -0.039 & 0.014 \\ -4.245 \times 10^{-3} & 0.014 & -7.392 \times 10^{-3} \end{pmatrix}$$

$$avgDSs := 9.6698 \cdot 10^{-12} \qquad Ss := \left[\frac{(avgDSs)}{(|SsK|)}\right]^{.5} \qquad Ss = 6.72 \times 10^{-3}$$

Figure C-1 (Continued).

$$K := SsK \cdot Ss \qquad K = \begin{pmatrix} -5.609\times 10^{-6} & 7.86\times 10^{-5} & -2.853\times 10^{-5} \\ 7.86\times 10^{-5} & -2.588\times 10^{-4} & 9.647\times 10^{-5} \\ -2.853\times 10^{-5} & 9.647\times 10^{-5} & -4.967\times 10^{-5} \end{pmatrix}$$

Figure C-1 (Continued).

Equation for the inverse diffusivity tensor:

$U = S_s K^{-1} = e_{j,1}{}^2 U_{11} + e_{j,2}{}^2 U_{22} + e_{j,3}{}^2 U_{33} + 2e_{j,1}e_{j,2} U_{12} + 2e_{j,2}e_{j,3} U_{23} + 2e_{j,1}e_{j,3} U_{13}$

$e_{j,i}$ = unit vector component pointing from injection point to monitoring point

i = component direction (1=east, 2=north, 3=vertical)

j = test number

X = jX6 matrix of coefficients identical to those in equation defining inverse diffusivity tensor

y = vector containing S_s/K_d (e_j) values obtained from testing

u = vector representing six unknown terms in U

uols = vector u solved by ordinary least squares

$$j := 1..7$$

$$e := \begin{pmatrix} 0.1021 & 0.6618 & -0.7427 \\ 0.1152 & 0.9556 & -0.2711 \\ 0.0677 & 0.7886 & 0.6112 \\ 0.2158 & 0.9576 & 0.1908 \\ 0.0704 & 0.4957 & 0.8657 \\ 0.0318 & 0.5959 & -0.8024 \\ 0.0272 & 0.9902 & -0.1372 \end{pmatrix}$$

$$X_{j,1} := \left(e_{j,1}\right)^2 \qquad X_{j,4} := 2e_{j,1} \cdot e_{j,2}$$

$$X_{j,2} := \left(e_{j,2}\right)^2 \qquad X_{j,5} := 2e_{j,2} \cdot e_{j,3}$$

$$X_{j,3} := \left(e_{j,3}\right)^2 \qquad X_{j,6} := 2e_{j,1} \cdot e_{j,3}$$

$$X = \begin{pmatrix} 0.01 & 0.438 & 0.552 & 0.135 & -0.983 & -0.152 \\ 0.013 & 0.913 & 0.073 & 0.22 & -0.518 & -0.062 \\ 0.005 & 0.622 & 0.374 & 0.107 & 0.964 & 0.083 \\ 0.047 & 0.917 & 0.036 & 0.413 & 0.365 & 0.082 \\ 0.005 & 0.246 & 0.749 & 0.07 & 0.858 & 0.122 \\ 0.001 & 0.355 & 0.644 & 0.038 & -0.956 & -0.051 \\ 0.001 & 0.98 & 0.019 & 0.054 & -0.272 & -0.007 \end{pmatrix} \qquad y := \begin{pmatrix} 99.33907697 \\ 22.96738631 \\ 32.8764955 \\ 16.75447739 \\ 7.076360917 \\ 19.92805714 \\ 41.22898679 \end{pmatrix}$$

$$uols := \left(X^T \cdot X\right)^{-1} \cdot X^T \cdot y \qquad uols = \begin{pmatrix} 5.97 \times 10^3 \\ 9.211 \times 10^1 \\ 6.378 \times 10^1 \\ -7.292 \times 10^2 \\ 8.318 \times 10^1 \\ -9.349 \times 10^2 \end{pmatrix}$$

Figure C-2 Least squares solution for directional hydraulic conductivity, wash (Site 2).

$$U := \begin{pmatrix} uols_1 & uols_4 & uols_6 \\ uols_4 & uols_2 & uols_5 \\ uols_6 & uols_5 & uols_3 \end{pmatrix} \qquad U = \begin{pmatrix} 5.97\times 10^{3} & -729.199 & -934.861 \\ -729.199 & 92.108 & 83.18 \\ -934.861 & 83.18 & 63.777 \end{pmatrix}$$

$$SsK := U^{-1} \qquad SsK = \begin{pmatrix} 1.443\times 10^{-4} & 4.317\times 10^{-3} & -3.516\times 10^{-3} \\ 4.317\times 10^{-3} & 0.068 & -0.026 \\ -3.516\times 10^{-3} & -0.026 & -2.506\times 10^{-3} \end{pmatrix}$$

$$avgDSs := 1.43205\cdot 10^{-14} \qquad Ss := \left[\frac{(avgDSs)}{|SsK|}\right]^{0.5} \qquad Ss = 3.22i\times 10^{-4}$$

$$K := SsK \cdot Ss \qquad K = \begin{pmatrix} 4.646i\times 10^{-8} & 1.39i\times 10^{-6} & -1.132i\times 10^{-6} \\ 1.39i\times 10^{-6} & 2.194i\times 10^{-5} & -8.234i\times 10^{-6} \\ -1.132i\times 10^{-6} & -8.234i\times 10^{-6} & -8.069i\times 10^{-7} \end{pmatrix}$$

Figure C-2 (Continued).

Appendix D. Theis Type Curve Matches

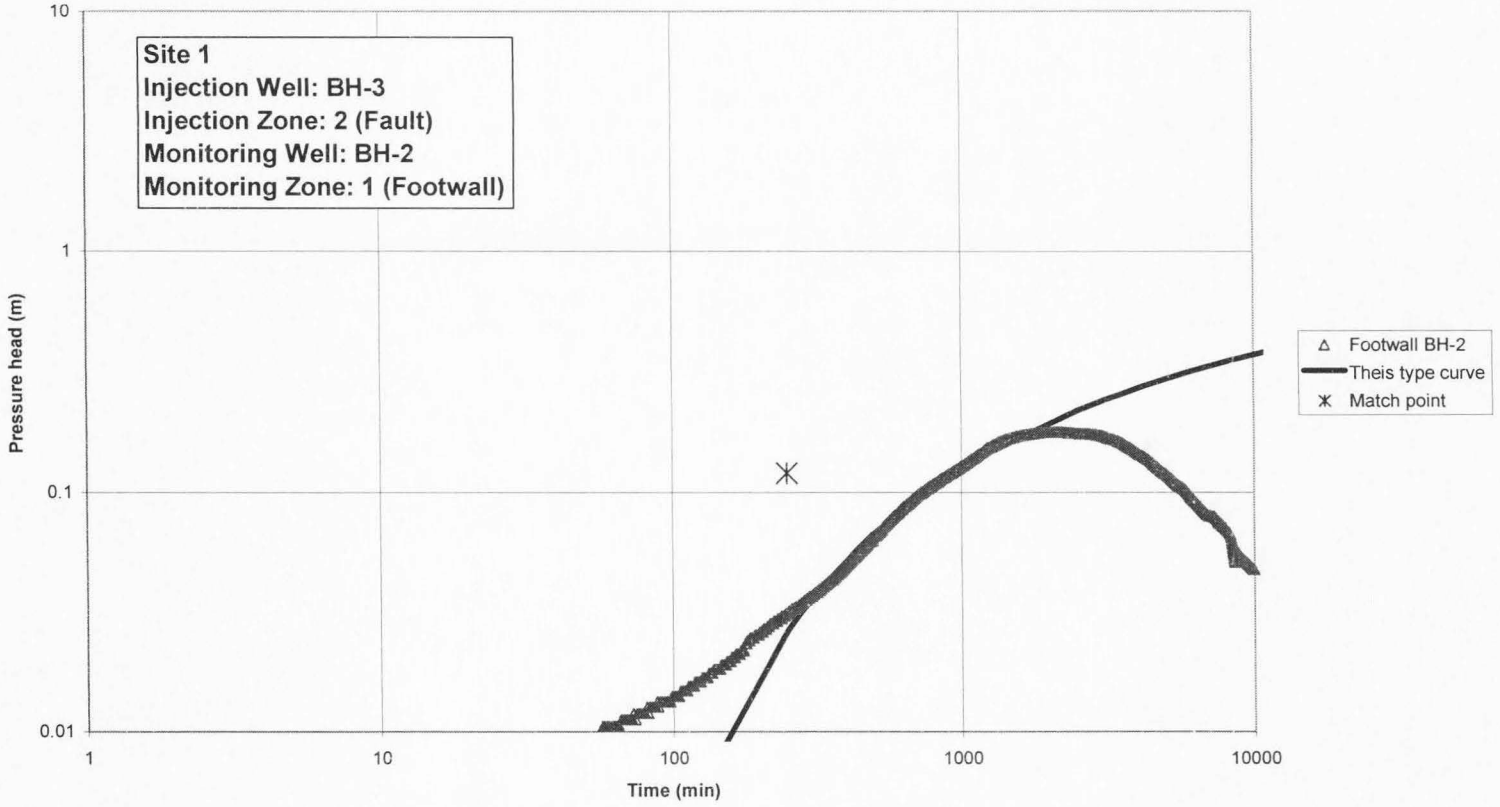

Figure D-1 Test 2 footwall pressure head response for fault injection (Zone 2) at fault tip (Site 1) monitored in BH-2 with Theis type curve.

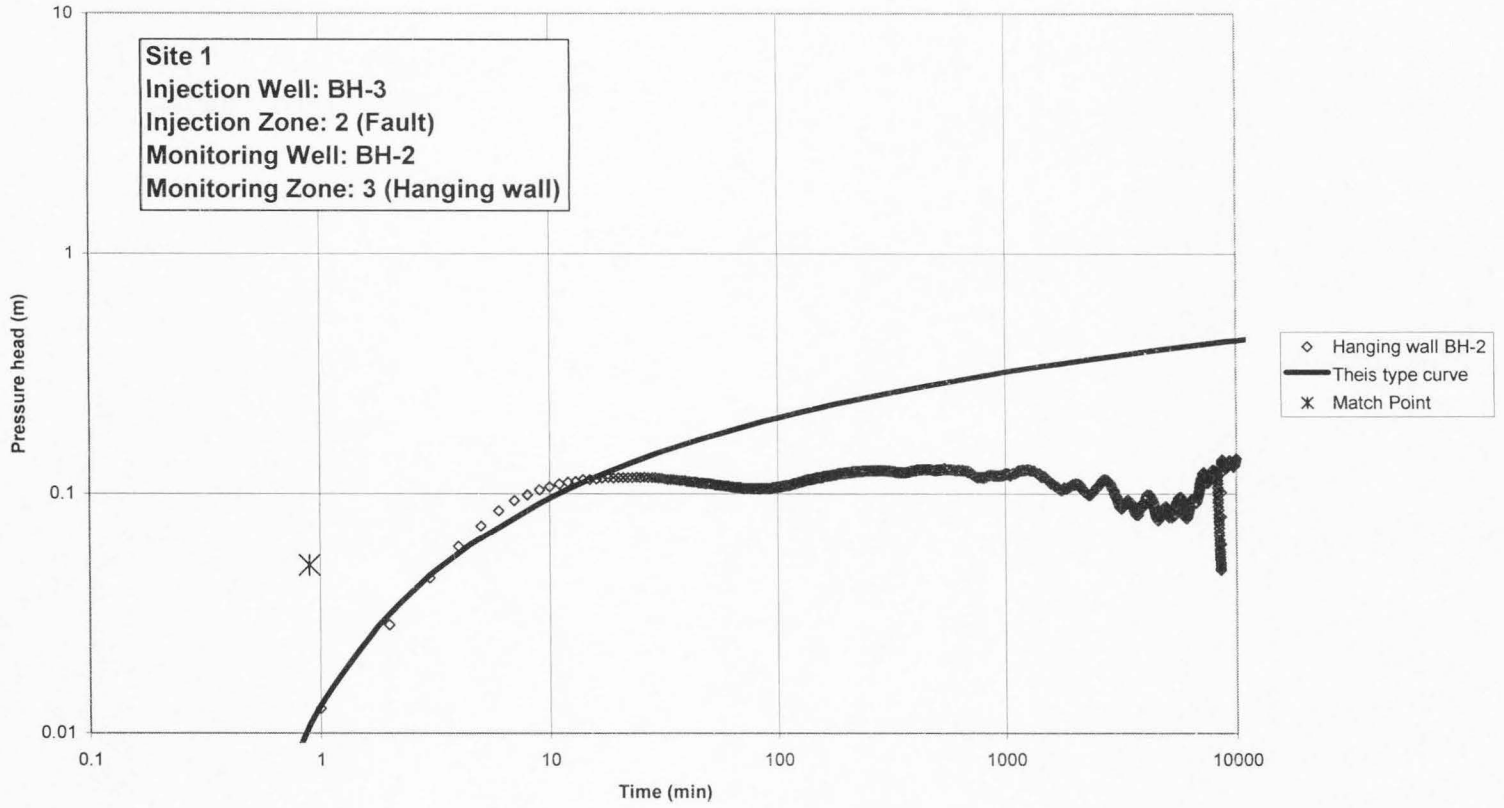

Figure D-2 Test 2 hanging wall pressure head response for fault injection (Zone 2) at fault tip (Site 1) monitored in BH-2 with Theis type curve.

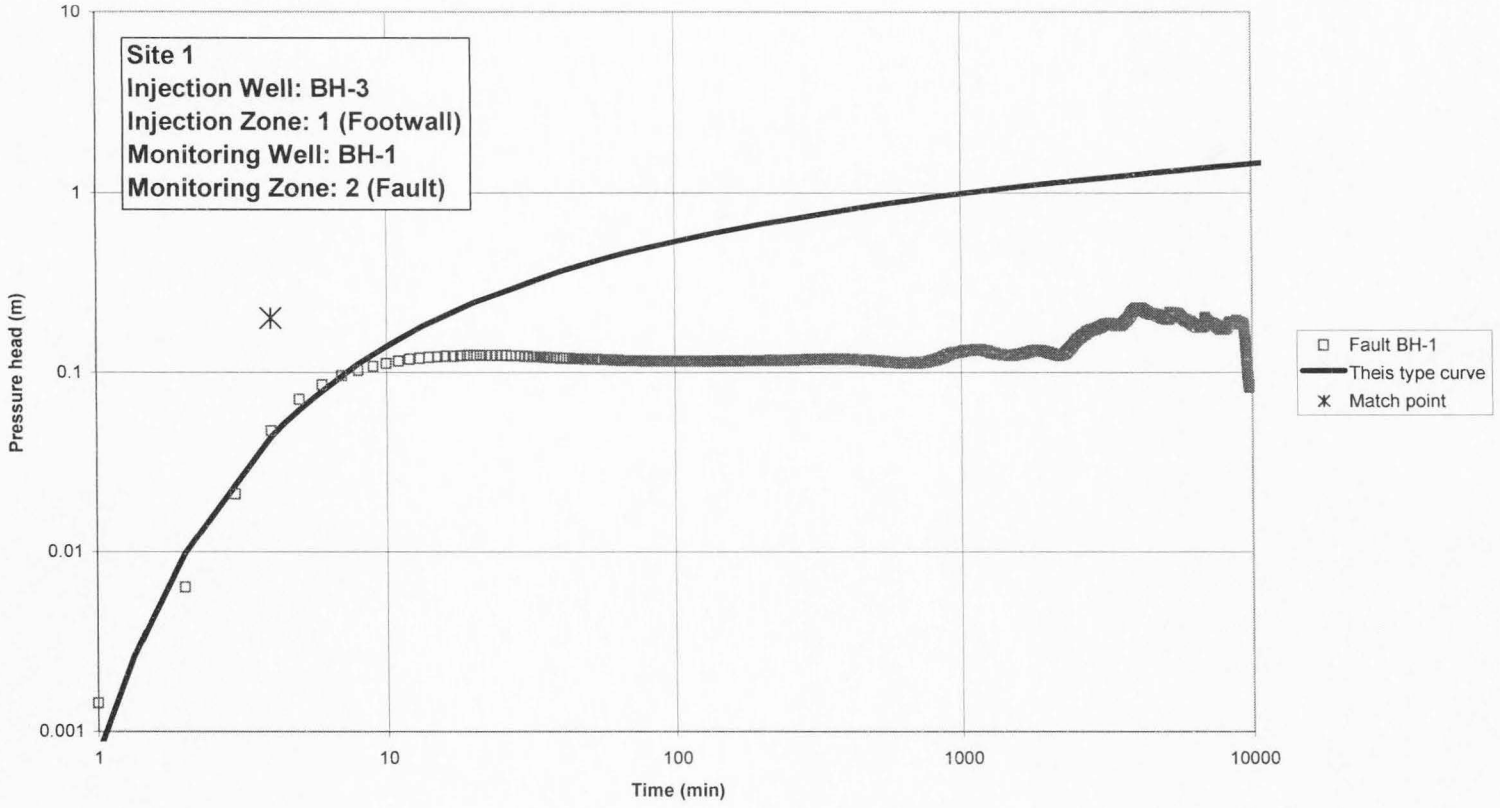

Figure D-3 Test 4 fault pressure head response for footwall injection (Zone 1) at fault tip (Site 1) monitored in BH-1 with Theis type curve.

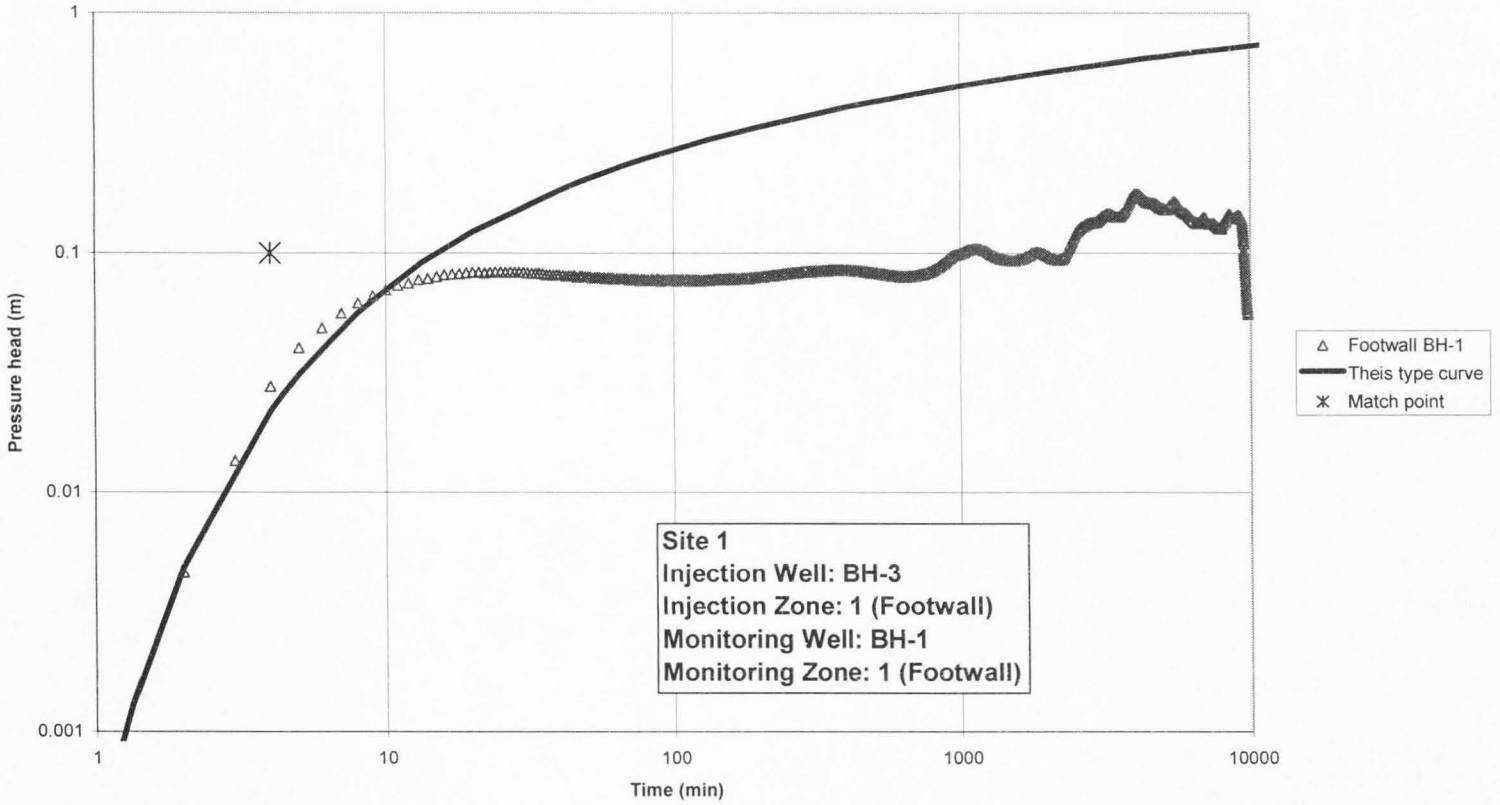

Figure D-4 Test 4 footwall pressure head response for footwall injection (Zone 1) at fault tip (Site 1) monitored in BH-1 with Theis type curve.

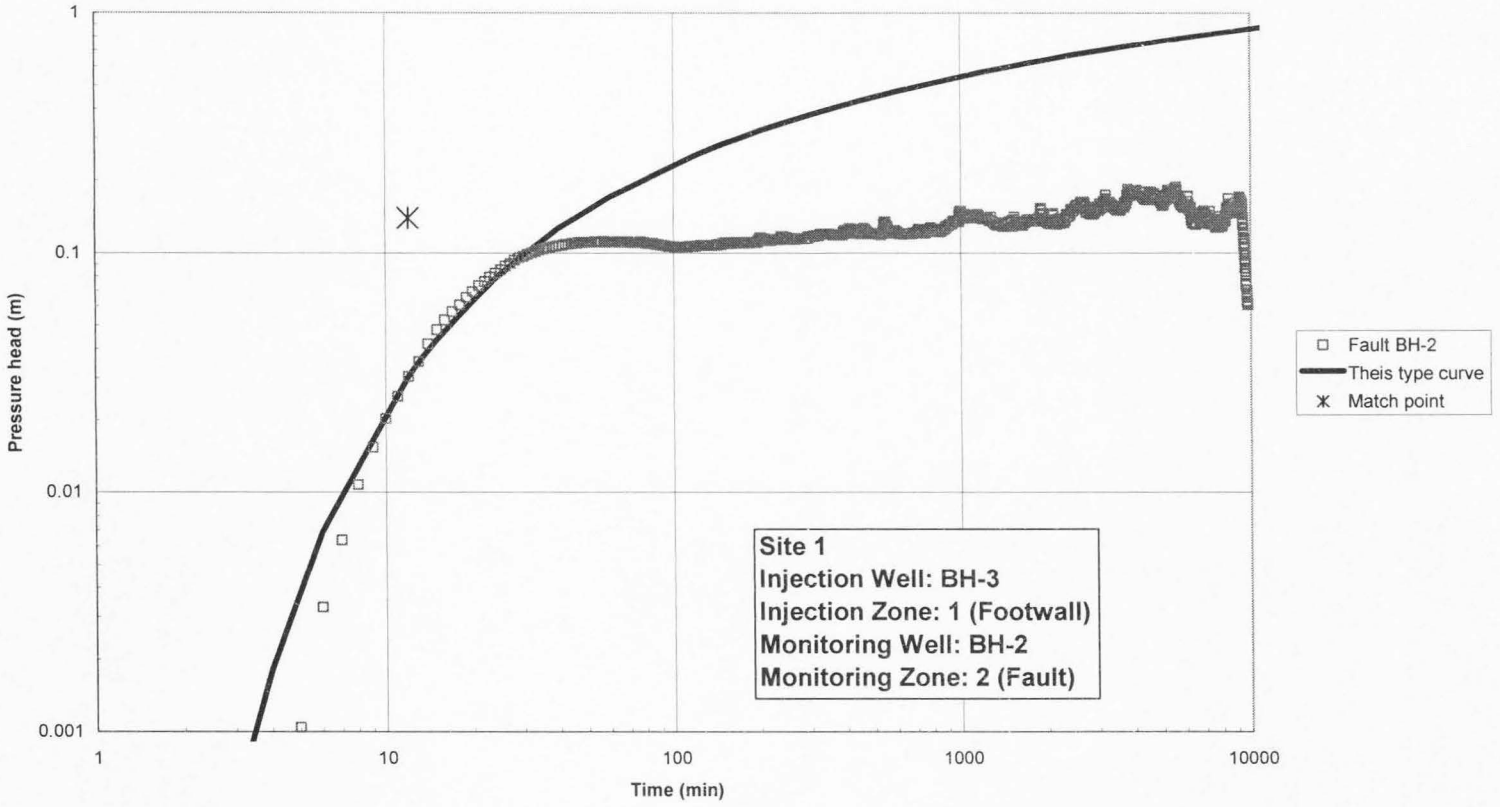

Figure D-5 Test 4 fault pressure head response for footwall injection (Zone 1) at fault tip (Site 1) monitored in BH-2 with Theis type curve.

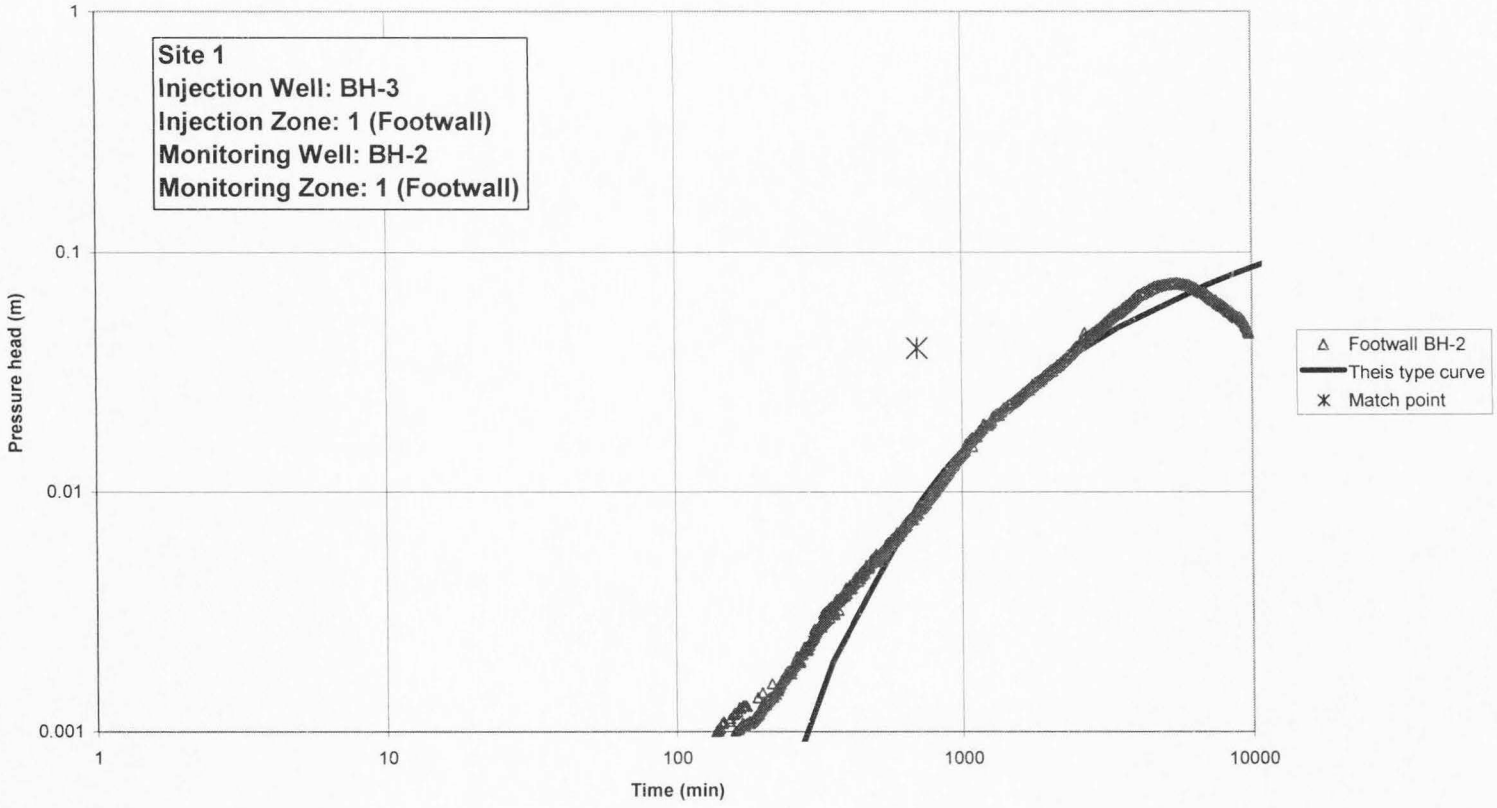

Figure D-6 Test 4 footwall pressure head response for footwall injection (BH-3, Zone 1) at fault tip (Site 1) monitored in BH-2 with Theis type curve.

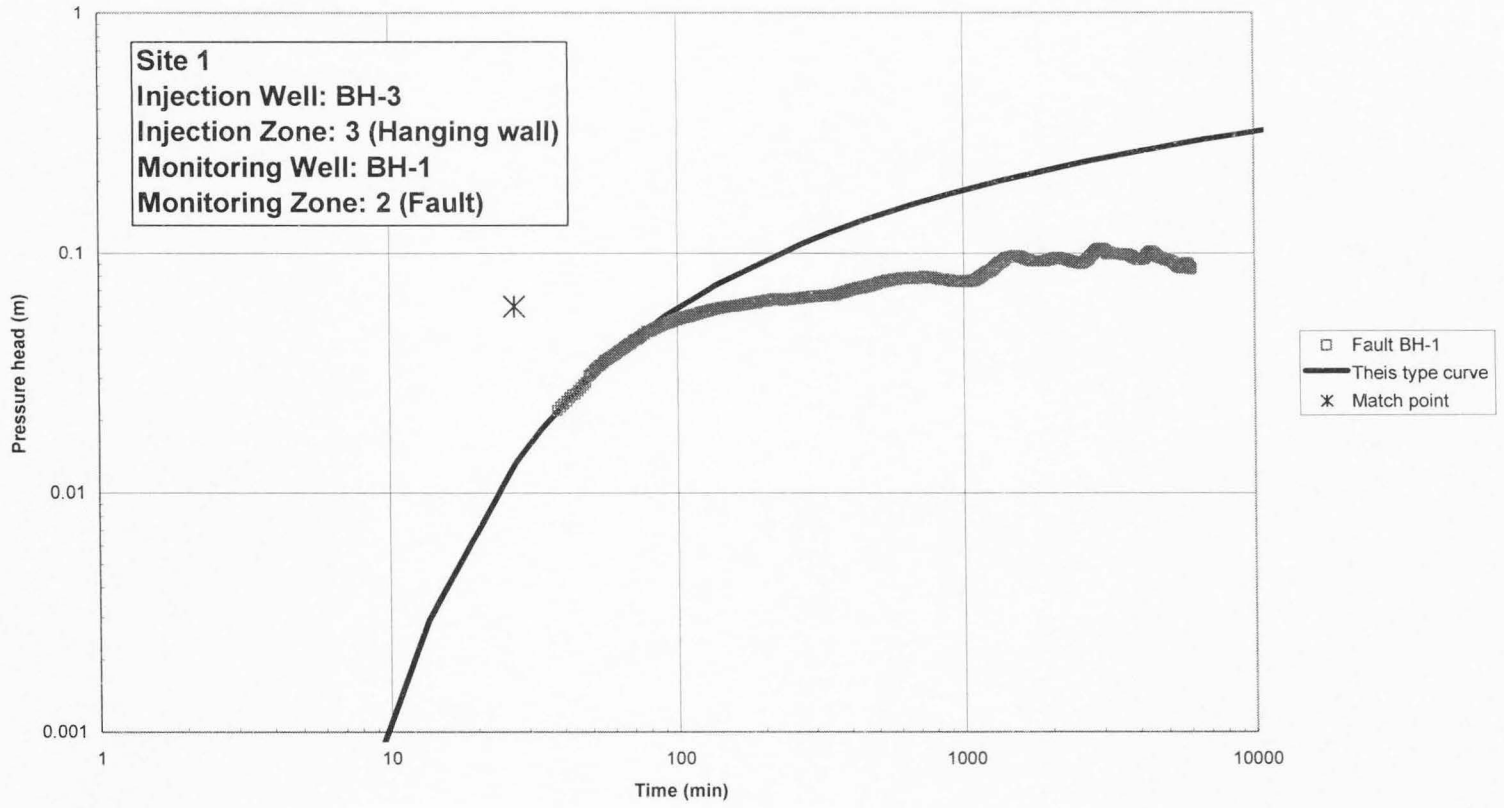

Figure D-7 Test 6 fault pressure head response for hanging wall injection (Zone 3) at fault tip (Site 1) monitored in BH-1 with Theis type curve.

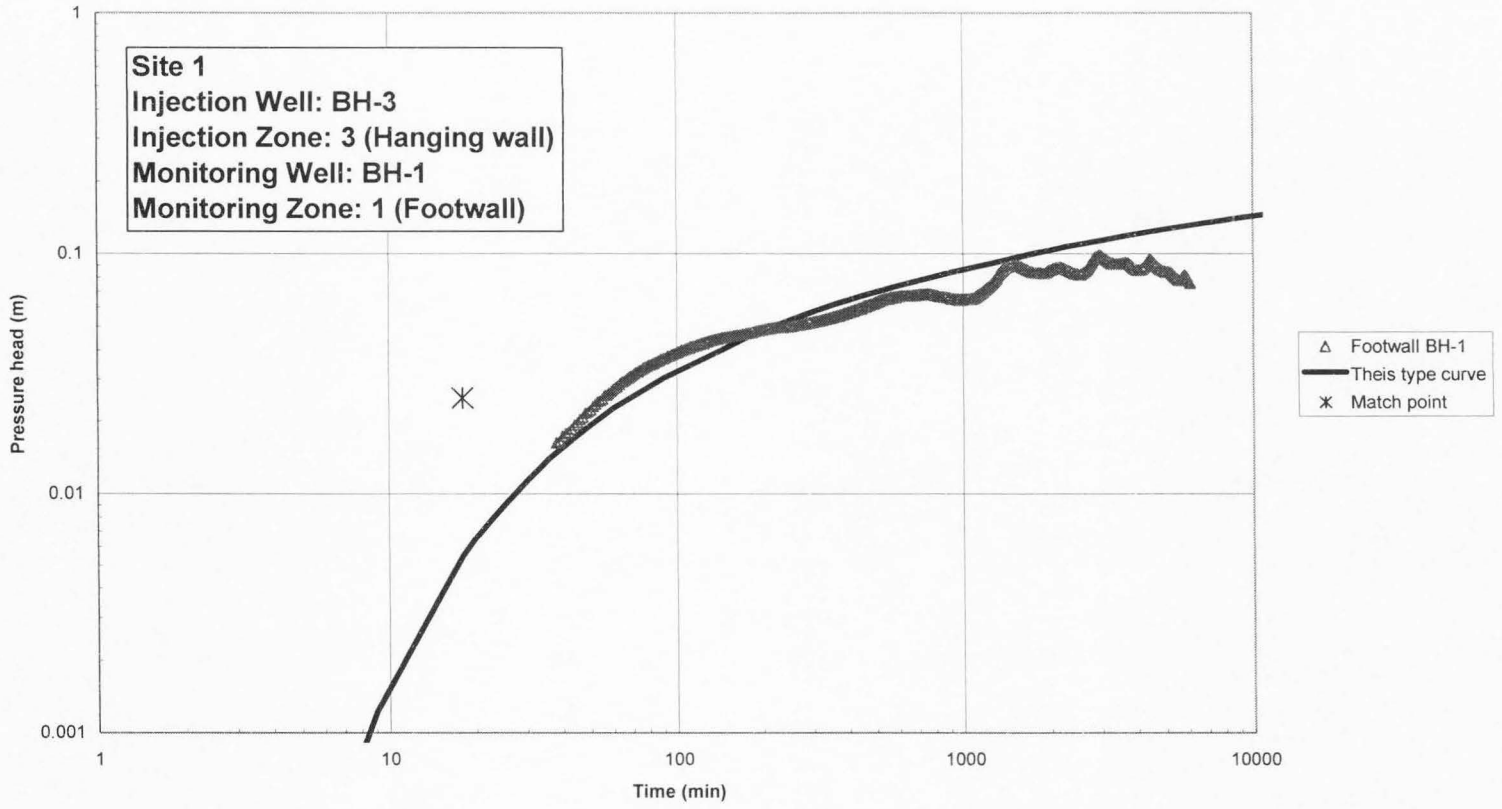

Figure D-8 Test 6 footwall pressure head response for hanging wall injection (Zone 3) at fault tip (Site 1) monitored in BH-1 with Theis type curve.

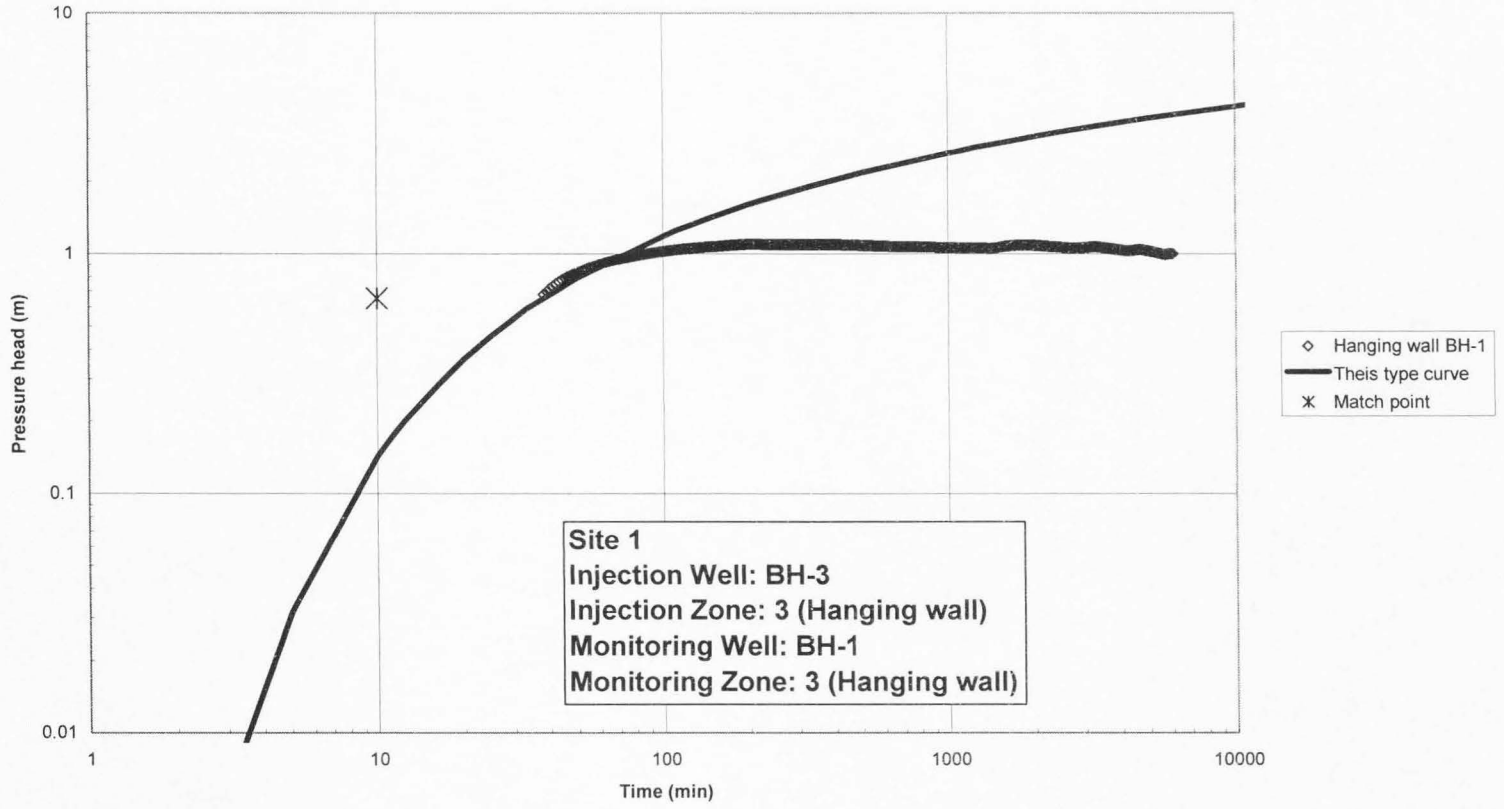

Figure D-9 Test 6 hanging wall pressure head response for hanging wall injection (Zone 3) at fault tip (Site 1) monitored in BH-1 with Theis type curve.

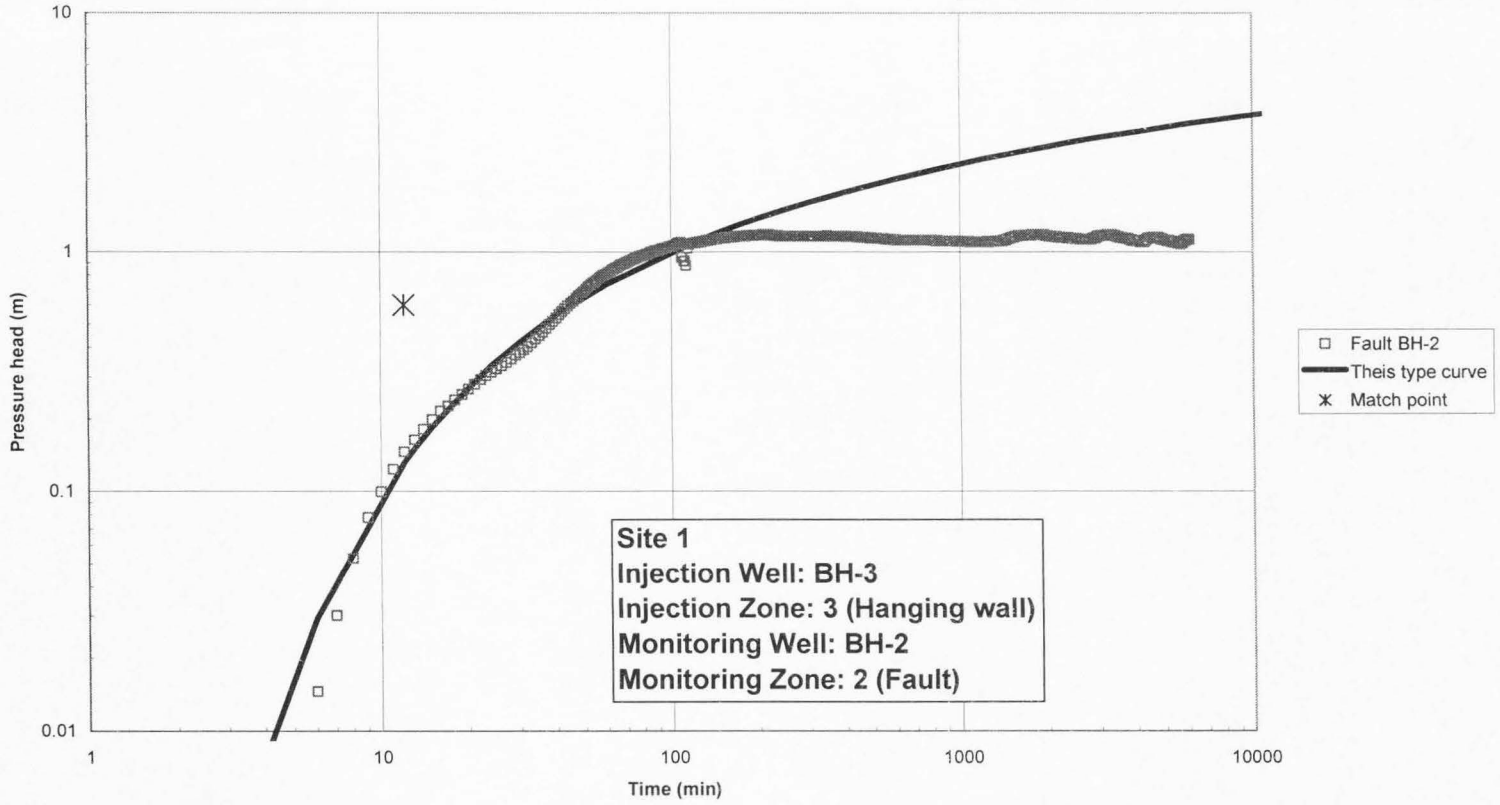

Figure D-10 Test 6 fault pressure head response for hanging wall injection (Zone 3) at fault tip (Site 1) monitored in BH-2 with Theis type curve.

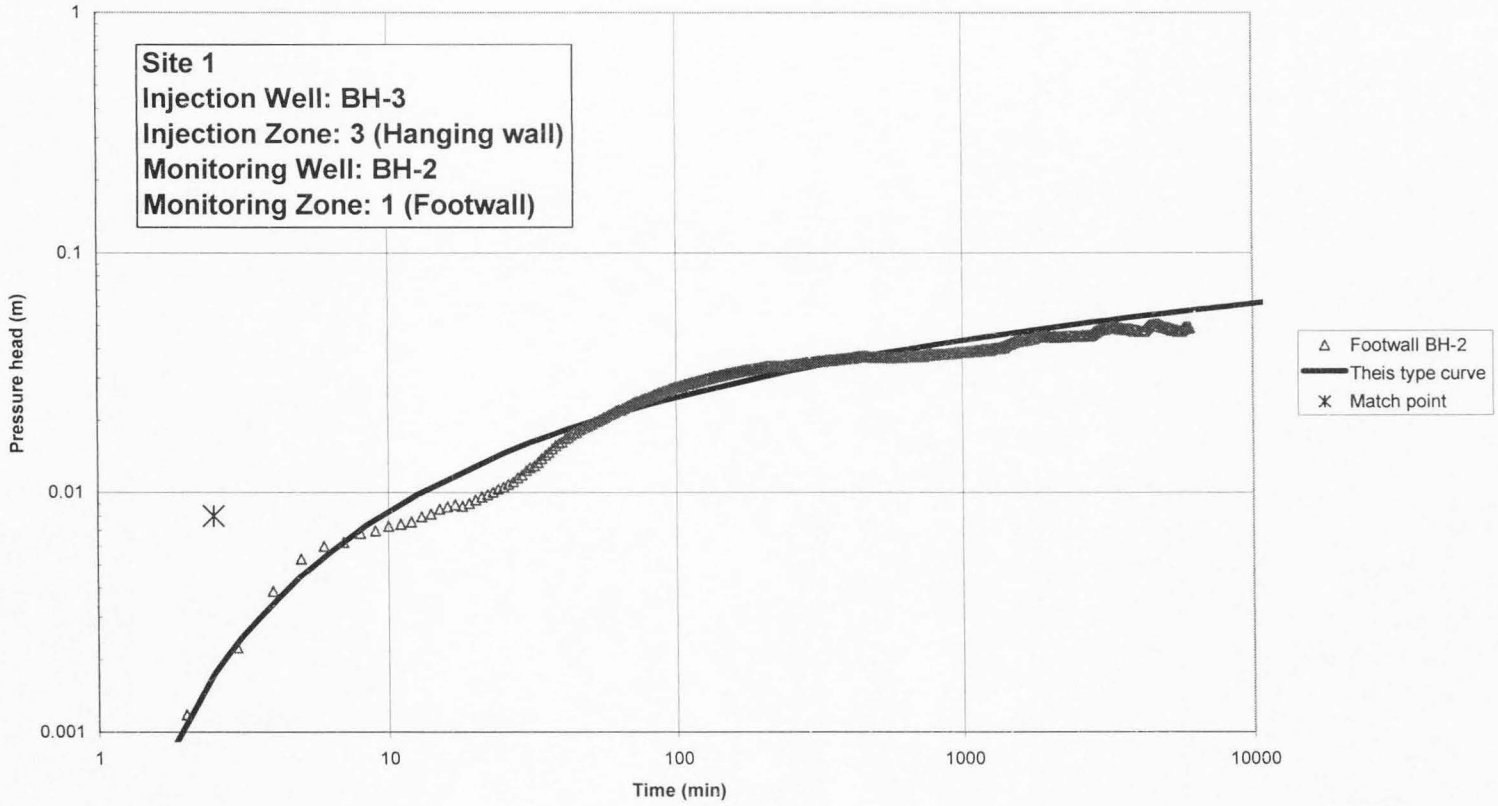

Figure D-11 Test 6 footwall pressure head response for hanging wall injection (Zone 3) at fault tip (Site 1) monitored in BH-2 with Theis type curve.

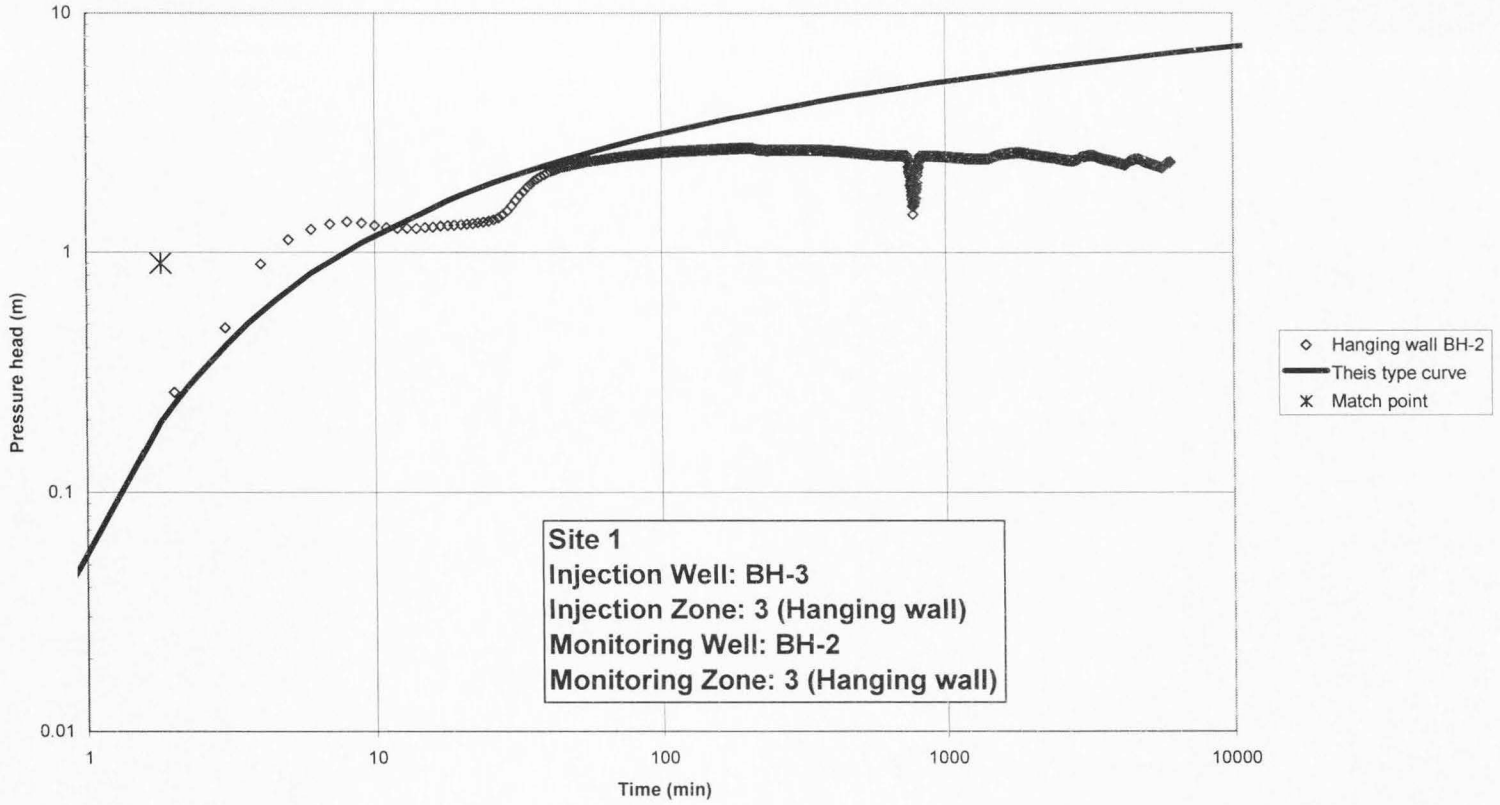

Figure D-12 Test 6 hanging wall pressure head response for hanging wall injection (Zone 3) at fault tip (Site 1) monitored in BH-2 with Theis type curve.

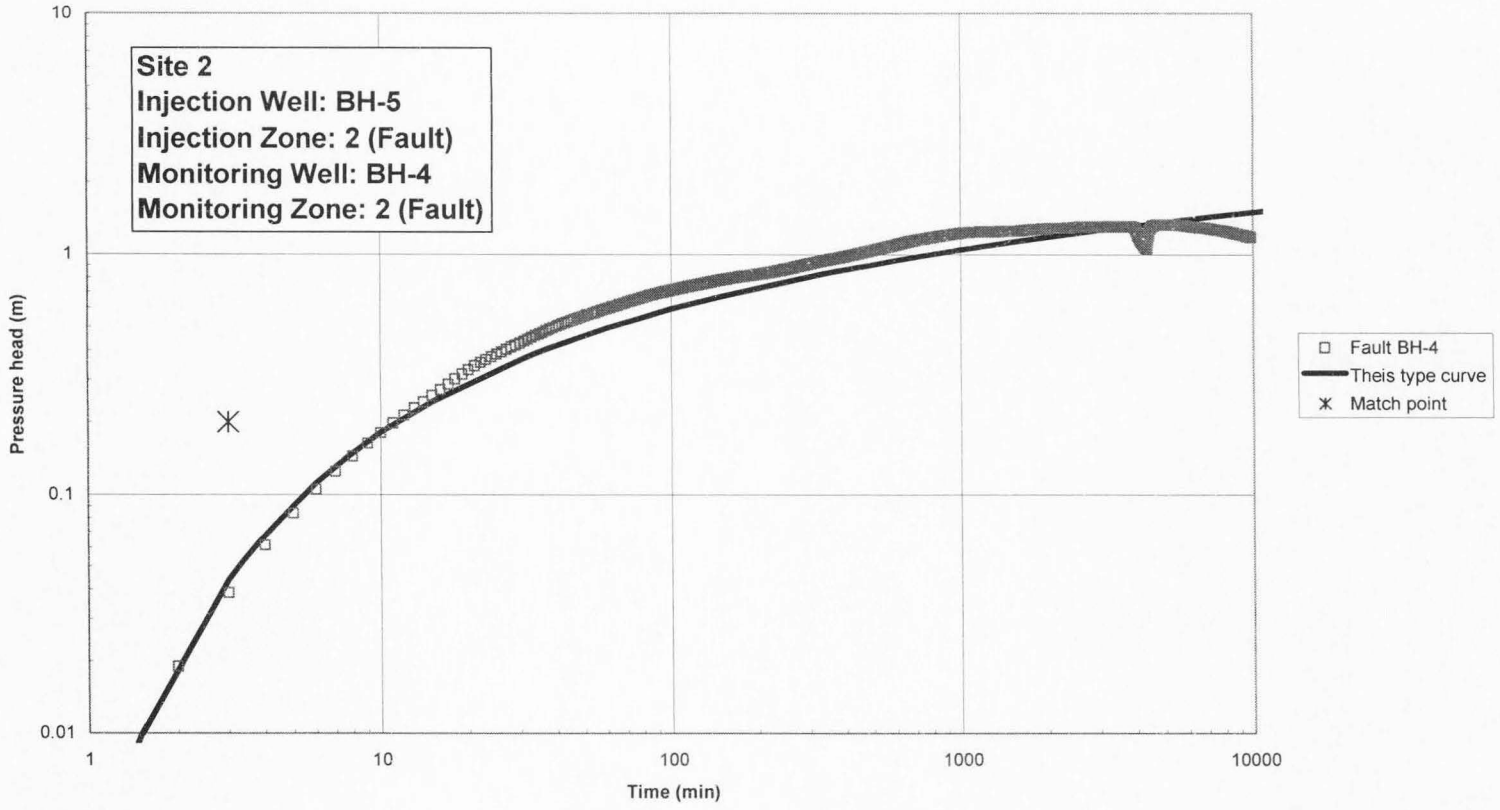

Figure D-13 Test 1 fault pressure head response for fault injection (Zone 2) at wash (Site 2) monitored in BH-4 with Theis type curve.

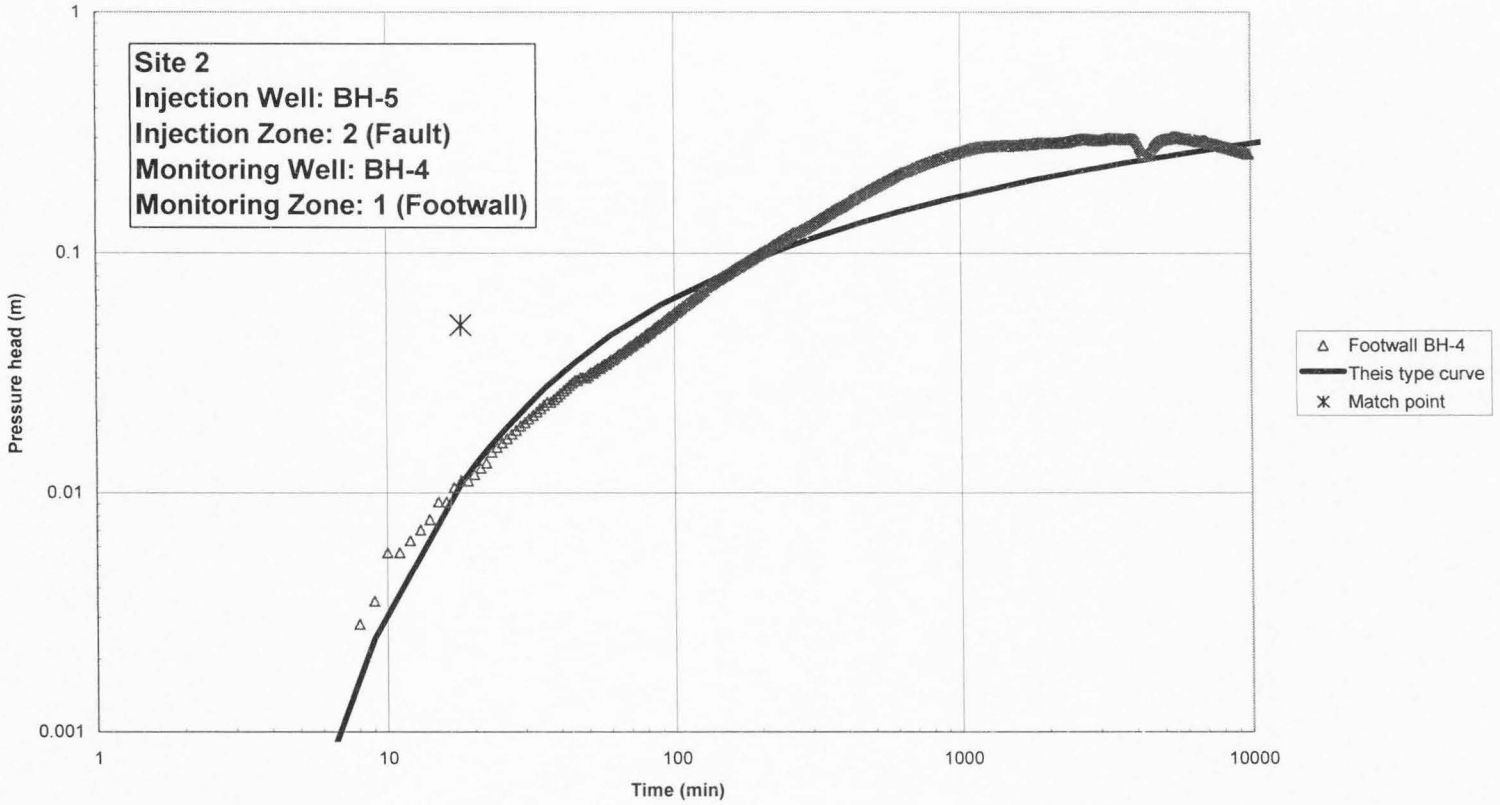

Figure D-14 Test 1 footwall pressure head response for fault injection (Zone 2) at wash (Site 2) monitored in BH-4 with Theis type curve.

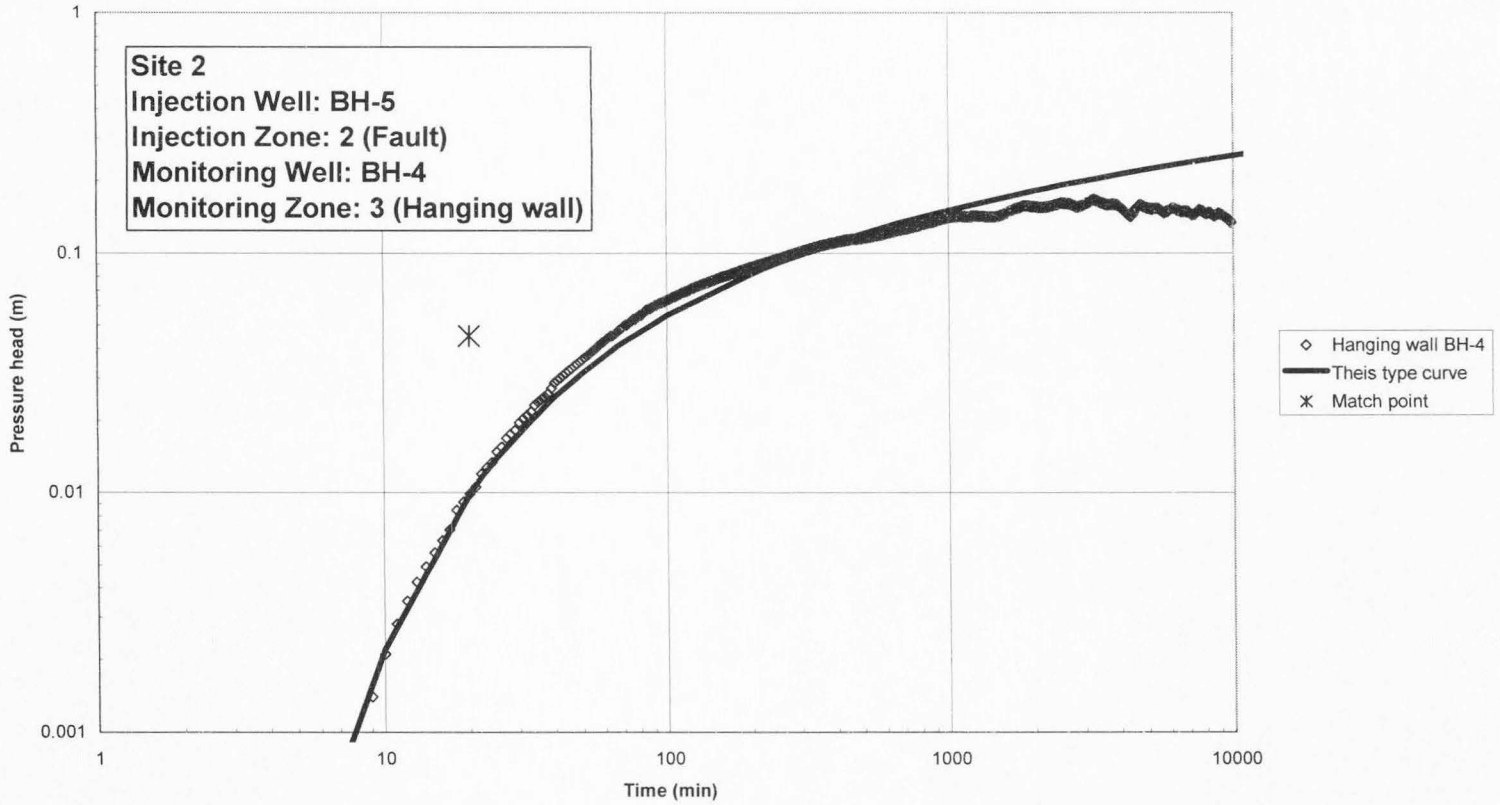

Figure D-15 Test 1 hanging wall pressure head response for fault injection (Zone 2) at wash (Site 2) monitored in BH-4 with Theis type curve.

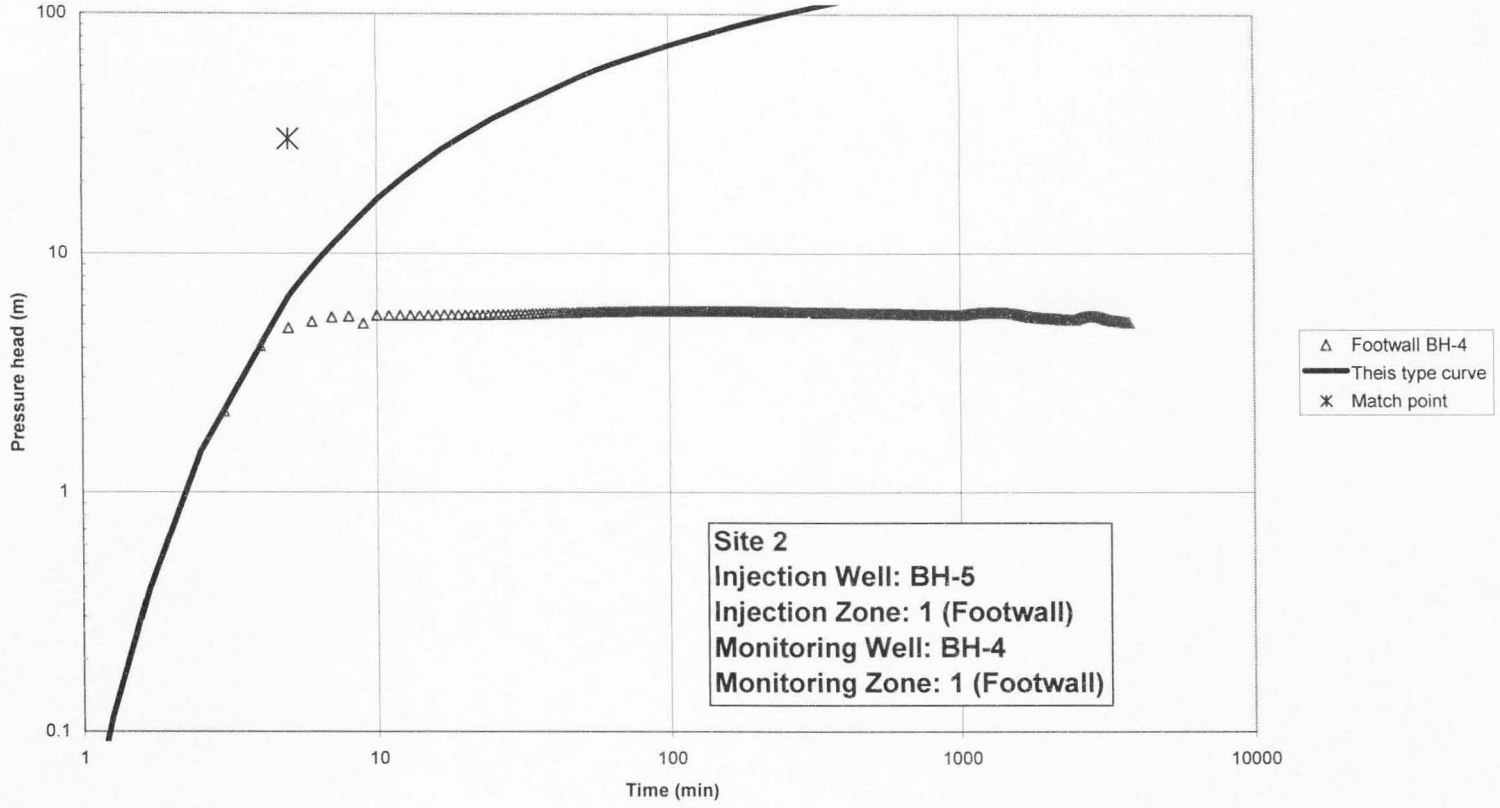

Figure D-16 Test 3 footwall pressure head response for footwall injection (Zone 1) at wash (Site 2) monitored in BH-4 with Theis type curve.

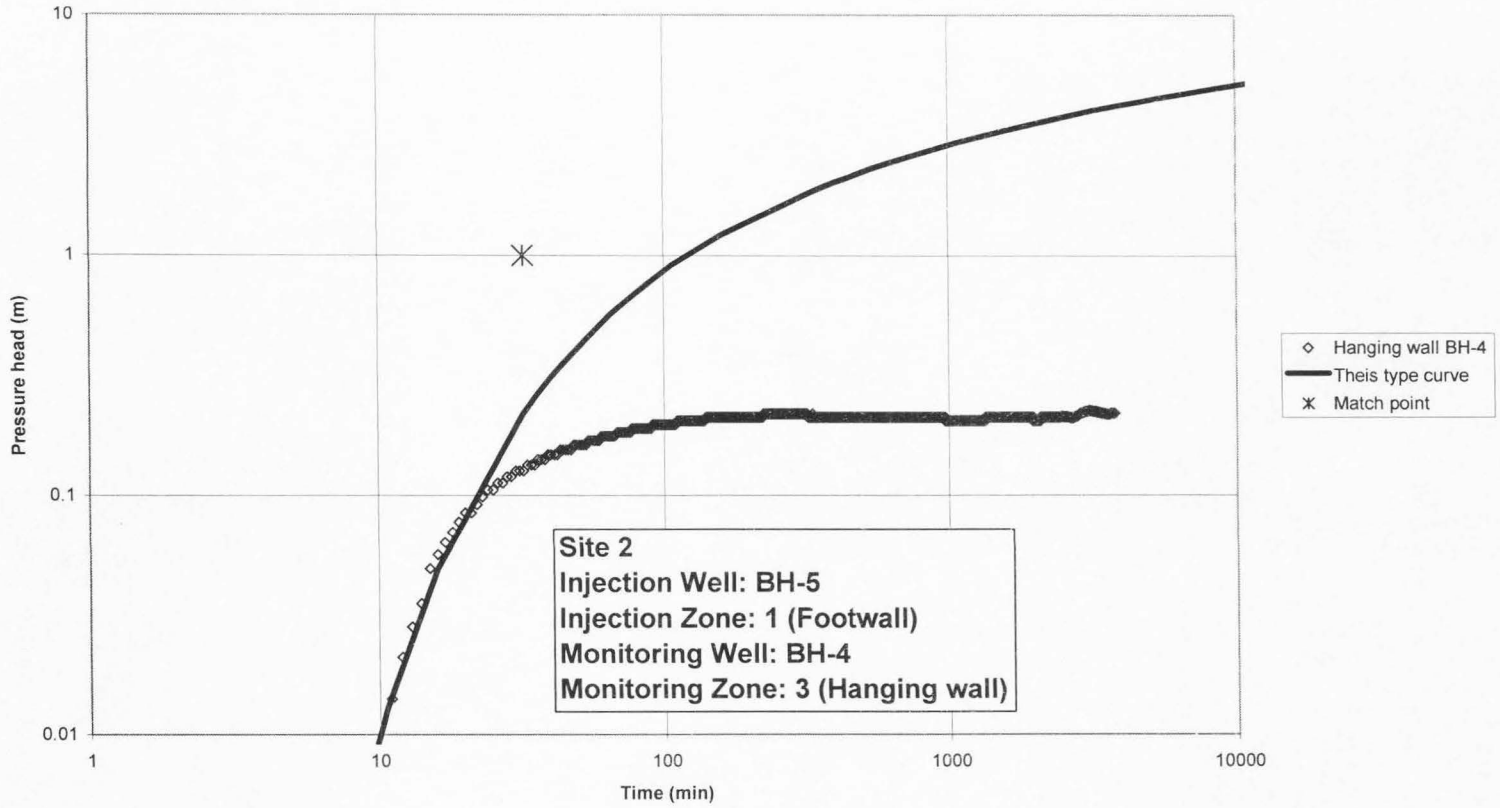

Figure D-17 Test 3 hanging wall pressure head response for footwall injection (Zone 1) at wash (Site 2) monitored in BH-4 with Theis type curve.

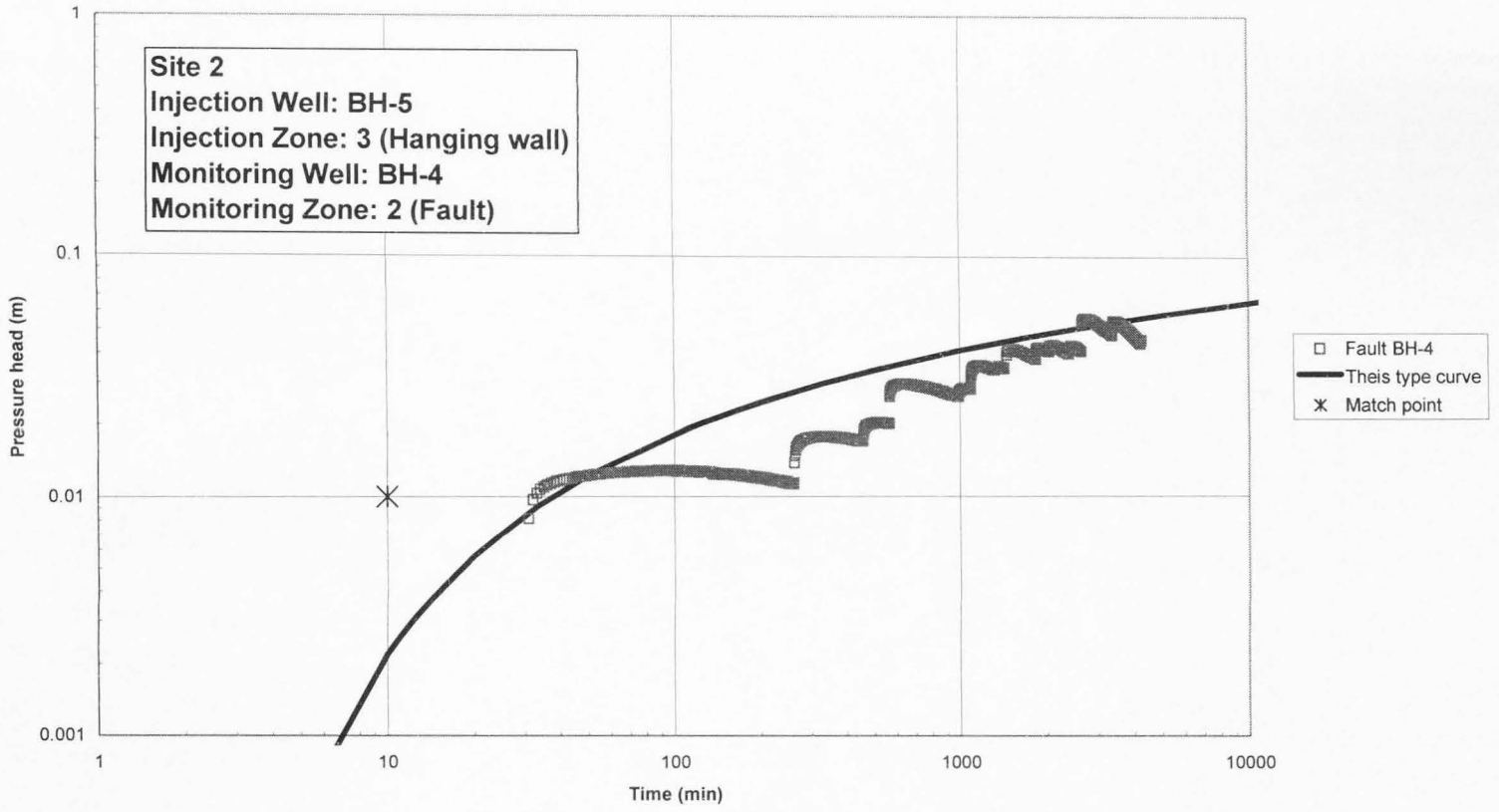

Figure D-18 Test 5 fault pressure head response for hanging wall injection (Zone 3) at wash (Site 2) monitored in BH-4 with Theis type curve.

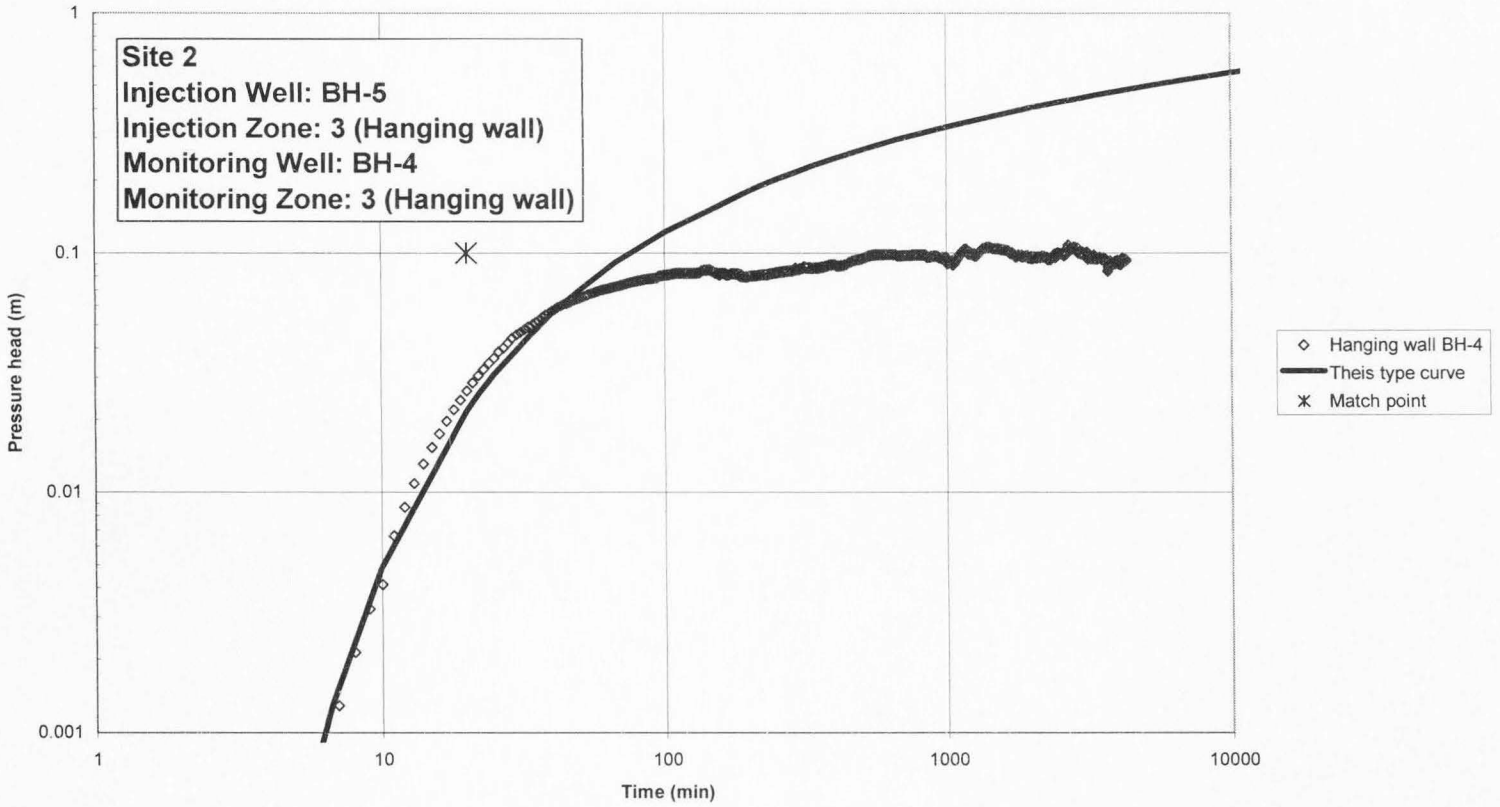

Figure D-19 Test 5 hanging wall pressure head response for hanging wall injection (Zone 3) at wash (Site 2) monitored in BH-4 with Theis type curve.